



Theses and Dissertations

2014-07-11

Refinement and Characterization of Synthetic Vocal Fold Models

Shelby Charisse Ward
Brigham Young University - Provo

Follow this and additional works at: <https://scholarsarchive.byu.edu/etd>



Part of the [Mechanical Engineering Commons](#)

BYU ScholarsArchive Citation

Ward, Shelby Charisse, "Refinement and Characterization of Synthetic Vocal Fold Models" (2014). *Theses and Dissertations*. 4225.

<https://scholarsarchive.byu.edu/etd/4225>

This Thesis is brought to you for free and open access by BYU ScholarsArchive. It has been accepted for inclusion in Theses and Dissertations by an authorized administrator of BYU ScholarsArchive. For more information, please contact scholarsarchive@byu.edu, ellen_amatangelo@byu.edu.

Refinement and Characterization of Synthetic Vocal Fold Models

Shelby C. Ward

A thesis submitted to the faculty of
Brigham Young University
in partial fulfillment of the requirements for the degree of
Master of Science

Scott L. Thomson, Chair
Tadd T. Truscott
Steven K. Charles

Department of Mechanical Engineering

Brigham Young University

July 2014

Copyright © 2014 Shelby C. Ward

All Rights Reserved

ABSTRACT

Refinement and Characterization of Synthetic Vocal Fold Models

Shelby C. Ward

Department of Mechanical Engineering, BYU

Master of Science

Understanding vocal fold mechanics is an integral part of voice research and synthetic vocal fold models are an essential tool in characterizing vocal fold mechanics. These models contain multiple layers with varying stiffness, much like human vocal folds. The purpose of this thesis is to improve the current models and modeling techniques, as well as investigate the impact of asymmetry on model vibration. A new design for an MRI-based model is detailed. This model has a more realistic geometry than the simplified models and mimics some of the vibratory characteristics observed in human vocal folds. The MRI-based model was used to investigate left-right stiffness asymmetry in multiple layers of the model. A zipper-like motion was observed during vibration of the MRI-based models. A phase shift was present in the asymmetric models, with the less stiff side leading the stiffer side. A new expendable mold fabrication process is described. This new process provides more freedom in designing vocal fold models and experiments. Additionally, the new process enables fabrication of models without the use of release agent, a factor which has, in the past, adversely impacted manufacturing yield and prohibited the incorporation of certain biological materials into the synthetic models. The new process also allows for more convenient geometry variation than what has previously been feasible. Finally, the new process was used to investigate cover layer geometry variation and asymmetry in a simplified model. Cover layer thickness was found to be a significant factor in governing the motion of the vocal fold model. Anterior-posterior asymmetry was found to induce the same zipper-like motion observed in the MRI-based models.

Keywords: vocal fold, voice, stiffness, asymmetry, geometry variation

ACKNOWLEDGEMENTS

I have very much enjoyed my time at BYU. While completing both my undergraduate and graduate degrees at BYU, I have received wonderful guidance and help from multiple sources. I could not have asked for a better advisor. Dr. Scott L. Thomson was exceptionally responsive to my ideas, and he guided my research in the right direction. He was a wonderful source of advice regarding research as well as career and life goals. Also, Dr. Thomson provided wonderful opportunities for growth. I am so grateful he chose to mentor me as a graduate student.

My graduate committee Dr. Tadd T. Truscott and Dr. Steven K. Charles provided me with support by reading and providing helpful revisions to improve the quality of my thesis work.

My fellow members of the Voice Biomechanics Lab provided me with assistance as well as suggestions to improve my research. I'd like to give special acknowledgement to Kimberly Stevens as she was an excellent source for brainstorming. Ryan Jenkins, Kevin Moore, Nelson Warner, and Nic Bons were helpful in machining and in the lab.

Funding for this research was provided by the National Institute on Deafness and Other Communication Disorders.

I'd also like to thank my family and friends who have been so supportive throughout this process, especially my parents for their endless encouragement and my wonderful fiancée Alexander Dushku II for his patience and faith in my abilities.

TABLE OF CONTENTS

LIST OF TABLES	viii
LIST OF FIGURES	x
1 Introduction	1
1.1 Chapters	3
1.1.1 Chapter 2: Left-Right Stiffness Asymmetry in an MRI-Based Geometry	3
1.1.2 Chapter 3: Expendable Mold Process	3
1.1.3 Chapter 4: Cover Layer Thickness Variation and Asymmetry	4
2 Left-Right Stiffness Asymmetry in an MRI-Based Geometry	5
2.1 Introduction	5
2.2 Methods	7
2.2.1 Model Geometry and Fabrication	7
2.2.2 Stiffness Asymmetry	12
2.2.3 Instrumentation and Measurement	13
2.3 Results and Discussion	15
2.3.1 Threshold Pressure	15
2.3.2 Flow Rate	15
2.3.3 Frequency	16
2.3.4 Model Motion	16
2.4 Conclusion	20
3 Expendable Mold Fabrication Process	23
3.1 Introduction	23

3.2	Old Process for Fabricating Vocal Fold Models	23
3.3	New Process for Fabricating Vocal Fold Models	27
3.3.1	Milling Equipment and Protocol.....	30
3.3.2	Detailed Description of New Modeling Process:.....	33
3.4	Conclusion	34
4	Cover Layer Thickness Variation and Asymmetry	36
4.1	Introduction.....	37
4.2	Methods	40
4.2.1	Model Design.....	40
4.2.2	Experimental Setup and Procedure.....	42
4.3	Results and Discussion	45
4.3.1	Threshold Pressure.....	45
4.3.2	Flow Rate	46
4.3.3	Frequency.....	46
4.3.4	Model Motion	48
4.3.5	Model Consistency.....	55
4.4	Conclusion	58
5	Conclusions and Recommendations	59
5.1	Chapter 2: Left-Right Asymmetric Stiffness in an MRI-Based Geometry	59
5.1.1	Future Work	60
5.2	Chapter 3: Expendable Mold Fabrication Process.....	61
5.2.1	Future Work	61
5.3	Chapter 4: Cover Layer Thickness Variation and Asymmetry.....	62

5.3.1 Future Work	62
REFERENCES.....	63
Appendix A. MRI-Based Model Design Details.....	65
Appendix B. MATLAB Code for Edge Tracking	68
Appendix C. Drawings and Process Sheets for the Mounting Plates.....	83
Appendix D. Vector 3D.....	89
Appendix E. Mach3 CNC set up.....	92
Appendix F. Curing Details	95

LIST OF TABLES

Table 2.1: Young's modulus values of cured silicone materials of different mixing ratios.	12
Table 2.2: Silicone mixing ratios used in different layers of different models.....	13
Table 4.1: Young's modulus values of the different silicone mixing ratios used in the models. .	41
Table 4.2: Cover layer thickness cases.	42
Table F.1: Silicone curing details.	95
Table F.2: Curing times used for Chapter 4 models.	95

LIST OF FIGURES

Figure 2.1: Different views of the MRI-derived models of Pickup and Thomson (2010) (left column) and the new, modified model (right column).	8
Figure 2.2: New MRI-based geometry with the curves that define the medial surface. Line 1 defines the medial surface on the anterior side. Line 2 is a curve from the points closest to the center sagittal plane projected onto the center sagittal plane. Line 3 defines the medial surface on the posterior side of the model.	9
Figure 2.3: Right fold of modified MRI-based vocal fold model. In the synthetic model, a thin (80-100 μm thick) epithelial layer (not shown) was applied to the cover layer surface....	10
Figure 2.4: Different views of the modified MRI-based model geometry.	10
Figure 2.5: Cross sections of the modified MRI-based model. All cross sections are to scale. a) Anterior cross section. b) 4.25 mm anterior-to-posterior cross section. c) 8.5 mm anterior-to-posterior cross section. d) 12.75 mm anterior-to-posterior cross section. e) Posterior cross section.....	11
Figure 2.6: Diagram of experimental setup, after Pickup and Thomson (2009).	14
Figure 2.7: a) Pressure, b) flow rate, and c) frequency data.	17
Figure 2.8: Sequence of high-speed images from three models. Asymmetric lateral excursions and variations in anterior-posterior zipper-like motion are evident. The arrows point out the zipper-like motion of the models.	18
Figure 2.9: Frame from high-speed image sequence, with line indicating anterior-posterior position along which left and right model edges were detected.	19
Figure 2.10: Edge positions vs. time for different stiffness configurations. a) Model 11, symmetric case, 1:1:4 Body 1:1:8 Cover. b) Model 2, Left-1:1:3 Body 1:1:8 Cover. c) Model 3, Left-1:1:5 Body 1:1:8 Cover. d) Model 6, Left-1:1:4 Body 1:1:5 Cover. e) Model 8, 1:1:4 Body 1:1:6 Cover.	20
Figure 3.1: 3D printed positive of the model made from ABS plastic.	25
Figure 3.2: Old process for synthetic model fabrication.....	26
Figure 3.3: Aluminum milling fixture and compacting piece used for building powdered sugar bricks.....	29
Figure 3.4: A picture of the CNC table top mill with the brick milling fixture attached.	29
Figure 3.5: Powdered sugar mold (left) and CAD model (right) of the mold.	31

Figure 3.6: CNC mill with 5-bit array adaptation and milling fixture.....	32
Figure 3.7: Side and main mounting plate assembly.....	33
Figure 3.8: New process for synthetic model fabrication.....	35
Figure 4.1: Cover layer thickness and geometries. Dimensions are in mm.....	43
Figure 4.2: Experimental setup.....	44
Figure 4.3: a) Average onset and offset pressure data (in kPa). b) Average onset and offset flow rate data (in L/min). c) Average frequency data (Hz).....	48
Figure 4.4: Standard (2.1 mm) cover layer at 110% onset pressure. Time between frames: 1 msec. a) Superior view high speed images. b) Side view high speed images. c) Edge position tracking. Each frame in rows a1 and a2 corresponds in time to the frame below in rows b1 and b2, respectively. Rows a2 and b2 are continuations of rows a1 and b1, respectively.....	51
Figure 4.5: Thinnest (0.5 mm) cover layer model at 110% onset pressure. Time between frames: 0.667 msec. a) Superior view high speed images. b) Side view high speed images. c) Edge position tracking. Each frame in rows a1 and a2 corresponds in time to the frame below in rows b1 and b2, respectively. Rows a2 and b2 are continuations of rows a1 and b1, respectively.....	52
Figure 4.6: 1.05 mm cover layer model at 110% onset pressure. Time between frames: 1 msec. a) Superior view high speed images. b) Side view high speed images. c) Edge position tracking. Each frame in rows a1 and a2 corresponds in time to the frame below in rows b1 and b2, respectively. Rows a2 and b2 are continuations of rows a1 and b1, respectively.....	53
Figure 4.7: 3.15 mm cover layer model at 110% onset pressure. Time between frames: 1.33 msec. a) Superior view high speed images. b) Side view high speed images. c) Edge position tracking. Each frame in rows a1 and a2 corresponds in time to the frame below in rows b1 and b2, respectively. Rows a2 and b2 are continuations of rows a1 and b1, respectively.....	54
Figure 4.8: 3.7 mm cover layer model at 110% onset pressure. Time between frames: 1.33 msec. a) Superior view high speed images. b) Side view high speed images. c) Edge position tracking. Each frame in rows a1 and a2 corresponds in time to the frame below in rows b1 and b2, respectively. Rows a2 and b2 are continuations of rows a1 and b1, respectively.....	55
Figure 4.9: Asymmetry case 1 (0.5-3.7 mm) cover layer at 110% onset pressure. Time between frames: 1.33 msec. a) Superior view high speed images. b) Side view high speed images. c) Edge position tracking. Each frame in rows a1 and a2 corresponds in time to the frame below in rows b1 and b2, respectively. Rows a2 and b2 are continuations of rows a1 and b1, respectively.....	56

Figure 4.10: Asymmetry case 2: 1.05-3.15 mm cover layer models at 110% onset pressure. Time between frames: 1.33 msec. a) Superior view high speed images. b) Side view high speed images. c) Edge position tracking. Each frame in rows a1 and a2 corresponds in time to the frame below in rows b1 and b2, respectively. Rows a2 and b2 are continuations of rows a1 and b1, respectively.	57
Figure A.1: Vocal fold surface derived from raw MRI data.....	65
Figure A.2: The highest points along the medial surface were selected and projected onto the midsagittal plane. These points formed a spline which served as the guide curve.....	65
Figure A.3: Points along the anterior surface were projected onto a coronal plane at the anterior-most surface.	66
Figure A.4: Points along the posterior surface were projected onto a coronal plane at the posterior-most surface.....	66
Figure A.5: The anterior and posterior curves were lofted along the guide curve, forming a surface.....	66
Figure A.6: This surface matches well with the raw MRI data.	67
Figure A.7: Finished MRI-based model.	67
Figure D.1: Model orientation.	89
Figure D.2: Model size.	90
Figure D.3: Rough cut settings.	90
Figure D.4: Finishing cut settings.....	91
Figure D.5: Toolpath save screen.	91
Figure E.1: Mach3 control panel.	92
Figure E.2: X, Y, and Z orientation	93
Figure E.3: Mach3 X-axis motor settings.....	93
Figure E.4: Mach3 Y-axis motor settings.....	94
Figure E.5: Mach3 Z-axis motor settings.	94

1 INTRODUCTION

Sound is produced as air from the lungs flows through the vocal folds and causes them to vibrate. This phenomenon of vocal fold flow-induced vibration is called phonation. The vocal folds are located in the larynx. They attach anteriorly to the thyroid cartilage and posteriorly to the arytenoid cartilages. Vocal fold oscillation causes pressure differences in the vocal tract, thereby producing sound. That is, whereas sound for speech is manipulated by the shape of the vocal tract, which begins at the top of the vocal folds and ends at the lips and nose, the actual source of sound in speech is the fluctuating air pressure near the vocal folds.

The current knowledge of voice production biomechanics is incomplete. Vocal fold vibration must be characterized in order to more fully understand voice disorders. A better understanding of the mechanics of vocal fold vibration and voice production could lead to better treatment and prevention of voice disorders. In particular, some voice disorders are related to vocal fold abnormalities, such as asymmetry in tissue stiffness or geometry. Changes in stiffness or geometry of the vocal fold tissue can be developmental, may emerge with age, or be caused by injury to the vocal folds. These pathological variations or inconsistencies can cause abnormal vibration which, in turn, can lead to voice problems.

Vocal fold models are an important tool in voice research. Most experiments cannot be performed *in vivo*, and excised larynges have limits. For example, excised larynges can be difficult to procure and transport. Maintaining hydration is a problem during transportation and experimentation. Geometry changes can take place before and after preservation. Longevity of

the excised larynges can be a limiting factor. There is very little control over geometry. Because of these difficulties and limitations, vocal fold models are emerging as a very important tool in voice research.

Vocal fold models can be divided into two categories: computational and synthetic. Significant work has been accomplished using computational models of the vocal folds; however, they are computationally expensive, must be verified, and do not always completely or accurately model relevant physical phenomena. Synthetic models can be further subdivided into three categories: static, driven, and self-oscillating. Static models are useful in understanding flow properties, but they can only be used to study the flow between the folds at a single instant in time in a given oscillation cycle. Driven models are mechanically driven by a motor or other mechanism. They can be useful in understanding some flow and vibratory phenomena, but since the human vocal folds are self-oscillating, driven models cannot completely model human vocal fold mechanics. Self-oscillating models are driven by air flow, as are the human vocal folds. Consequently, although they are difficult to design, much can be learned from self-oscillating models.

In order to improve voice research capabilities, self-oscillating vocal fold models need to be further developed and refined. Many of the existing models have simplified geometries and do not accurately model many important vibratory metrics. The focus of this thesis is on the continued development and study of synthetic vocal fold models. A new model based on MRI data was designed, a new model fabrication process was developed, and the influences of stiffness and geometry asymmetries were investigated.

1.1 Chapters

1.1.1 Chapter 2: Left-Right Stiffness Asymmetry in an MRI-Based Geometry

Left-right stiffness asymmetry has been studied previously using physical, self-oscillating models (Pickup and Thomson, 2009; Zhang and Luu, 2012; Zhang et al., 2013). However, it has not been studied in a model with realistic geometry. Many have been performed using two layer models, in which the muscle and ligament layers are represented by the “body” layer, and the superficial lamina propria and epithelial layers are represented by the “cover” layer. Body layer stiffness was varied by Zhang and Luu (2012) and Zhang et al. (2013), and cover layer stiffness was varied by Pickup and Thomson (2009). However, there has yet to be a study in which both cover and body layer stiffness values have been varied.

In Chapter 2, the effect of left-right stiffness asymmetry on vocal fold model vibration is examined. A three-layer, MRI-based model was designed for this experiment. Both body and cover layer stiffness were varied in order to better understand the role of each layer on vocal fold vibration.

1.1.2 Chapter 3: Expendable Mold Process

The current synthetic vocal fold model fabrication process has several weaknesses. Two primary issues include: (1) model fabrication requires release agent, which is toxic to cells and can, in some cases, prevent curing, and (2) fabricating models with geometry variation is costly and time consuming. In Chapter 3, a new “expendable mold” model fabrication process that eliminates the need for release agent, increases ease of geometry variation, and improves the fabrication process in several other ways is described.

1.1.3 Chapter 4: Cover Layer Thickness Variation and Asymmetry

Since vocal fold asymmetry can be associated with voice disorders, it has been explored in several studies. However, many of these studies have only focused on stiffness asymmetry (Alipour et al., 2000; Pickup and Thomson, 2009; Xue et al., 2010; Zhang, 2010; Zhang and Luu, 2012; Zhang et al., 2013). Geometry asymmetry or variation has also been studied, but only in computational or in static models (Scherer et al., 2001; Cook et al., 2009; Pickup and Thomson, 2011; Smith and Thomson, 2012; Xuan and Zhang, 2014). In these papers, stiffness and geometry asymmetries have only been studied in the left-right (medial-lateral) direction; anterior-posterior asymmetry has not been studied.

In Chapter 4, use of the fabrication process described in Chapter 3 is described in which the effect of anterior-posterior cover layer geometry variation on vocal fold vibratory mechanics was investigated.

2 LEFT-RIGHT STIFFNESS ASYMMETRY IN AN MRI-BASED GEOMETRY

2.1 Introduction

Understanding vocal fold stiffness asymmetry has important clinical implications. The effect of asymmetric stiffness on vocal fold vibration has been studied using synthetic and computational vocal fold models (Pickup and Thomson, 2009; Zhang and Luu, 2012; Zhang et al., 2013). Pickup and Thomson (2009) varied stiffness in the cover layer, while in Zhang and Luu (2012) and Zhang et al. (2013) the body layer stiffness was varied. These studies are briefly summarized below.

Pickup and Thomson (2009) studied a simplified two-layer self-oscillating model based on the so-called “M5” model of Scherer et al. (2001) with left-right asymmetry in the cover layer stiffness. The right vocal fold was varied, while the left vocal fold was kept constant. The body layers of all models had a Young’s modulus of about 8.9 kPa. The left cover layer had a Young’s modulus of 3.3 kPa and the modulus of the right cover layer varied from 2.9 to 8.7 kPa between models. These modulus values are comparable to those of human vocal fold tissue. A 30 cm upstream duct was used with no vocal tract. Onset pressure, high-speed imaging data, and PIV data were acquired. The PIV data were analyzed and vibration metrics were extracted from the high speed data. It was shown that an increase in asymmetry increased the phase difference between opposing vocal fold models. This phase difference influenced the shape of the orifice

area (or shape between the vocal folds), which could affect the quality of the generated sound, and also resulted in increased phonation onset pressure.

Zhang and Luu (2012) used a two-layer self-oscillating vocal fold model to investigate the influence of left-right asymmetry. The cover layer Young's modulus was 3.25 kPa while the body-layer Young's modulus varied from 3.25 kPa to 73.16 kPa. An 11 cm upstream duct was used with no simulated vocal tract. High speed image data were collected at several flow rates. The experimental results were compared with those of a numerical study. It was found that for pairs with a large variation in stiffness, the vibration was dominated by the softer fold. The stiffer fold was out of phase with and had a lower amplitude than the softer fold. The phase difference increased with greater severity of stiffness mismatch, with the stiffer fold leading the more flexible fold. However, when the stiffness mismatch was less severe, the amplitude and frequency differences were also less significant.

As in the above two studies, Zhang et al. (2013) used a simplified, two-layer, self-oscillating vocal fold model to study the influence of left-right stiffness asymmetry on vocal fold vibration. An 11 cm circular upstream duct was used with a 17 cm long duct downstream of the vocal fold model to simulate the vocal tract. Three sets of left-right asymmetry configurations were studied: left-right symmetric conditions with varying body stiffness, left-right asymmetry with the control (right) fold having a stiff body layer and varying left body stiffness, and finally, left-right asymmetry with a softer body layer in the control (right) fold. Acoustic measurements were acquired and human perceptual testing of the sound produced by the models was performed. This study found that vibrational amplitude changes and phase differences caused by asymmetry were perceptually insignificant unless those differences caused the vibratory pattern

to change regimes. This suggests that left-right asymmetry may not always affect voice quality, but may be a symptom of other problems.

Most prior synthetic vocal fold model experiments have been performed using models with simplified geometry. In particular, the studies mentioned above were all performed using simplified geometries that were generally similar to the M5 model (Scherer et al., 2001) and had cross sections that were uniform in the anterior-posterior direction; i.e., they were symmetric anterior-posteriorly. Further, in each of these studies the stiffness was only varied in one layer. Lacking in the literature are studies of left-right asymmetry using more geometrically-realistic models and stiffness asymmetry that spans across multiple layers. In this chapter the findings of research designed to study stiffness asymmetry in multiple layers of a vocal fold model with MRI-based geometry are reported.

2.2 Methods

2.2.1 Model Geometry and Fabrication

The MRI model of Pickup and Thomson (2010), derived from MRI data with slightly abducted vocal folds, was modified for this study. Because of the slight abduction of the folds in this image set, the medial surface of the model presented by Pickup and Thomson (2010) was slightly bowed; see Figure 2.1. For this study, the model was adjusted to medialize the surface in the following manner (see Appendix A for additional details). To correct for the bowing of the medial surface, the highest points (or points closest to the center sagittal plane) along the medial surface were found. The curve passing through these points was projected onto the center sagittal plane, forming Line 2 in Figure 2.2. The curves formed by two coronal planes spaced 17 mm

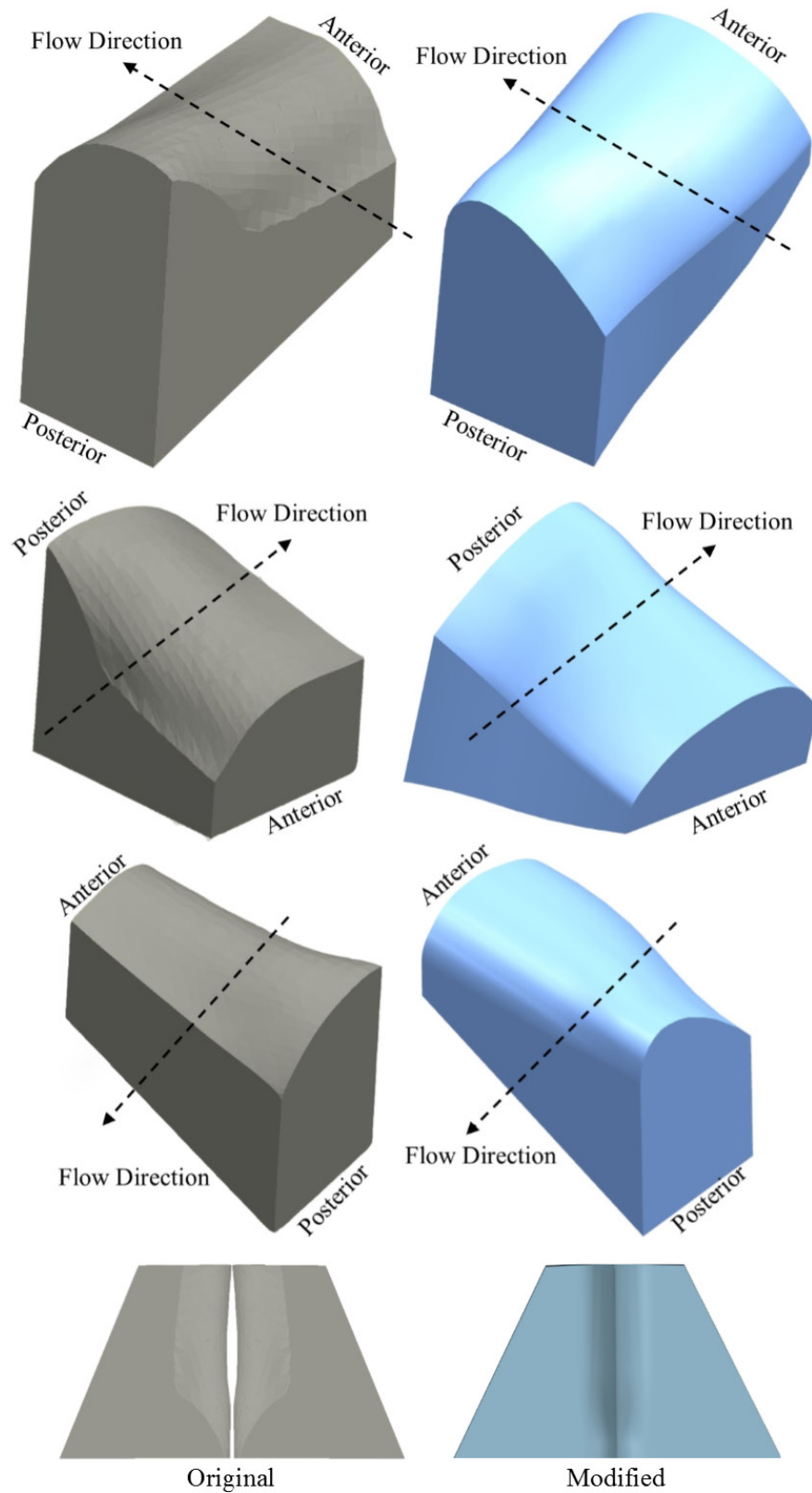


Figure 2.1: Different views of the MRI-derived models of Pickup and Thomson (2010) (left column) and the new, modified model (right column).

apart that cut through each end of the vocal folds and the MRI geometry surface (Lines 1 and 3 in Figure 2.2) were lofted along the curve projected from the highest points along the medial surface (Line 2 in Figure 2.2). The resulting surface followed the outer geometry of the scan, with the exception of the bowed medial surface, and was used to define the outside geometry of the cover layer.

The lateral surface of the model followed a 62° angle from the posterior surface (see Figure 2.3). This created a 56° angle at the thyroid notch, approximating the lateral vocal fold margin along the thyroid cartilage (Zrunek et al., 1988).

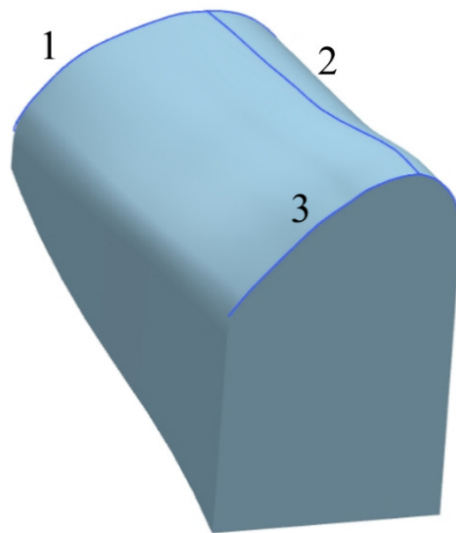


Figure 2.2: New MRI-based geometry with the curves that define the medial surface. Line 1 defines the medial surface on the anterior side. Line 2 is a curve from the points closest to the center sagittal plane projected onto the center sagittal plane. Line 3 defines the medial surface on the posterior side of the model.

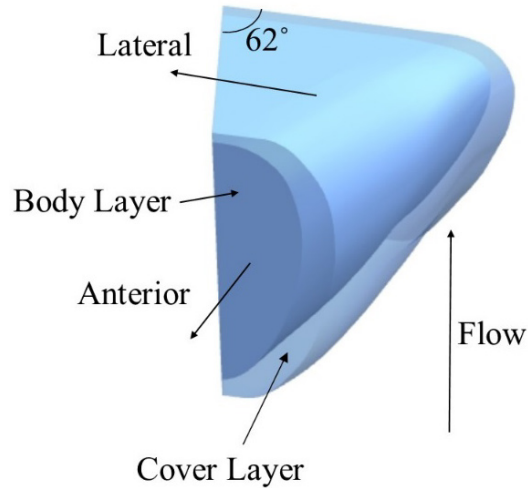


Figure 2.3: Right fold of modified MRI-based vocal fold model. In the synthetic model, a thin (80-100 μm thick) epithelial layer (not shown) was applied to the cover layer surface.

Another important geometric feature of the model is the changing inferior-superior thickness of the vocal fold along the anterior-posterior direction. These are illustrated in the cross sections of the model shown in Figure 2.5. The inferior-superior thickness at the anterior-most side was 12 mm, whereas the corresponding thickness at the posterior-most side was only 10 mm. The body layer geometry was based on the cover layer geometry; however, there were some small adjustments made in the cover layer thickness. The anterior-posterior dimension was 17 mm, corresponding to the anterior-posterior length of vocal folds for the average adult male (Baken, 1999).

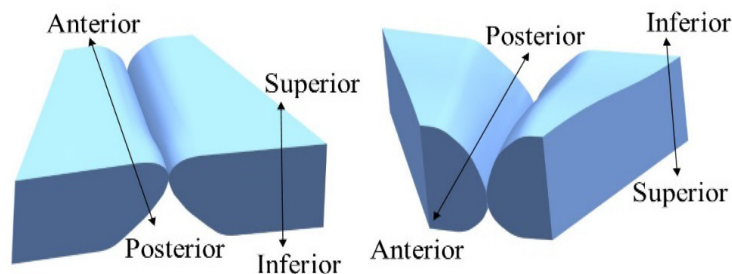


Figure 2.4: Different views of the modified MRI-based model geometry.

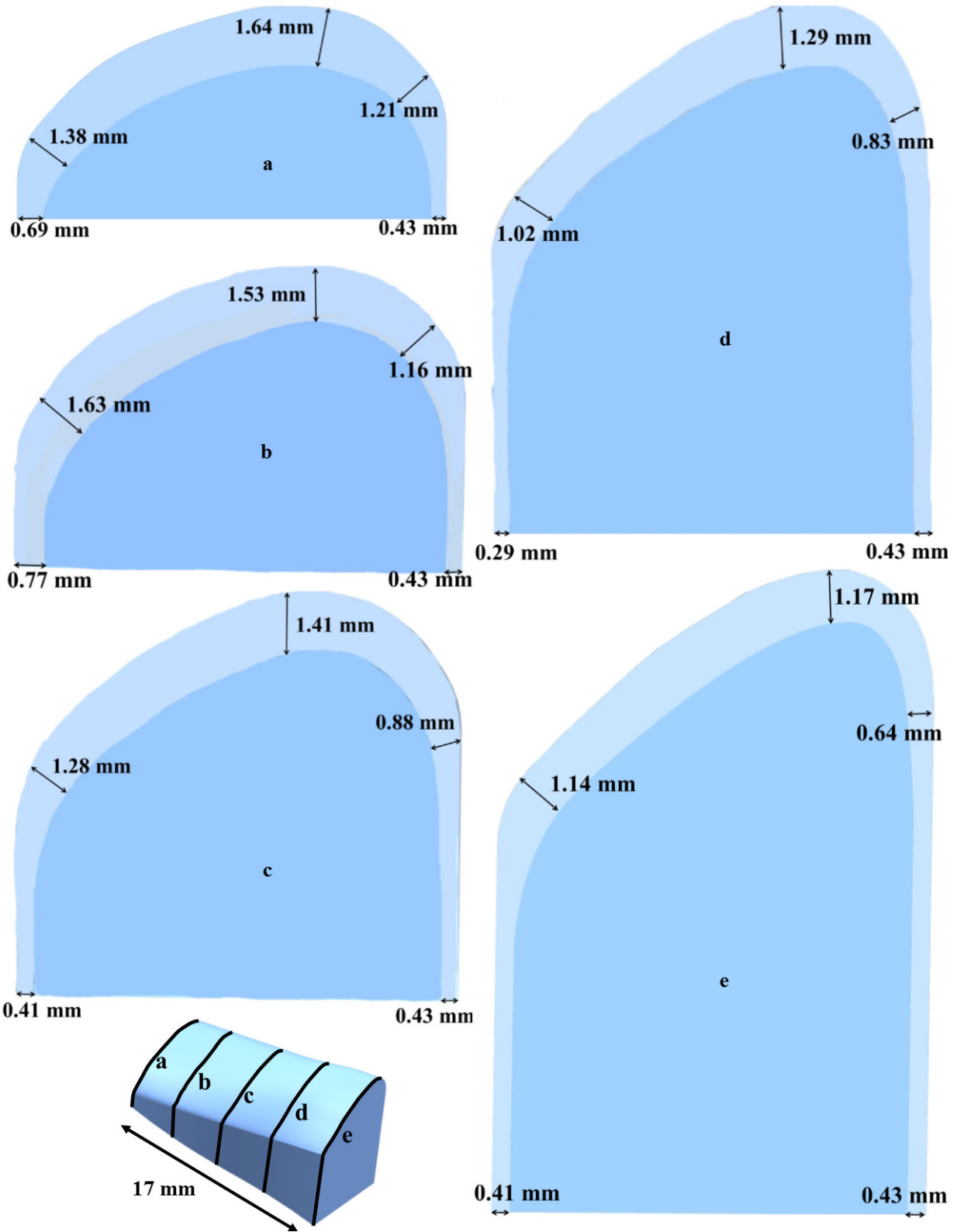


Figure 2.5: Cross sections of the modified MRI-based model. All cross sections are to scale. a) Anterior cross section. b) 4.25 mm anterior-to-posterior cross section. c) 8.5 mm anterior-to-posterior cross section. d) 12.75 mm anterior-to-posterior cross section. e) Posterior cross section.

The model was fabricated using different ratios of a two-part silicone compound (Ecoflex 0030, Smooth-On Inc., Easton, PA) mixed with silicone thinner (Silicone Thinner, also by Smooth-On, Inc.) Increasing the amount of thinner results in reduced Young's modulus of the cured material. The mixing ratio of the body layer was 1:1:4 by weight (Part A Ecoflex:Part B Ecoflex:Thinner) of Smooth-On Ecoflex® 0030. The cover layer was 1:1:8, also of Ecoflex® 0030. A thin (estimated 100 µm thick) epithelial layer was applied to the outside of the cover layer, as has been documented elsewhere (Murray and Thomson, 2011). This layer was 1:1:1 of Smooth-On Dragon Skin 10®. Young's modulus values for several mixing ratios is given in Table 2.1. The Young's modulus values were found via a tensile test using an Instron 3342 machine with an Instron 2519-102 force transducer (www.instron.us). The fabrication process used here is described in detail by Murray and Thomson (2011).

Table 2.1: Young's modulus values of cured silicone materials of different mixing ratios.

Ratio	Young's modulus (kPa)
1:1:3 Ecoflex	5.2 kPa
1:1:4 Ecoflex	3.1 kPa
1:1:5 Ecoflex	2.0 kPa
1:1:6 Ecoflex	1.7 kPa
1:1:8 Ecoflex	<1 kPa
1:1:1 Dragon Skin	33.2 kPa

2.2.2 Stiffness Asymmetry

Two left-right asymmetry conditions were explored: asymmetry in body stiffness, and asymmetry in cover stiffness. Table 2.2 lists the silicone ratios of the different models. For the models in which the body layer stiffness was varied, both a less stiff and a stiffer body layer

were paired with the normal cover. For the models in which the cover layer was varied, both of the cover layers tested were stiffer than the control model. A less stiff cover layer was not tested because the silicone would not cure with a thinner ratio higher than 1:1:8. In this study the left fold stiffness was varied and the stiffness of the right fold was constant. A separate right model was paired with each of the left models, but all of the right models were fabricated using the same mixing ratio. Three symmetric models and two models of each asymmetric ratio were fabricated and tested; the first column in Table 2.2 gives corresponding model numbers that will be referenced in sections below.

Table 2.2: Silicone mixing ratios used in different layers of different models.

Model Number	Model Description	Left		Right	
		Body	Cover	Body	Cover
1, 2	stiffer body	1:1:3	1:1:8	1:1:4	1:1:8
3, 4	less-stiff body	1:1:5	1:1:8	1:1:4	1:1:8
5, 6	stiffer cover	1:1:4	1:1:5	1:1:4	1:1:8
7, 8	stiffer cover	1:1:4	1:1:6	1:1:4	1:1:8
9, 10, 11	symmetric	1:1:4	1:1:8	1:1:4	1:1:8

2.2.3 Instrumentation and Measurement

The experimental setup is illustrated in Figure 2.6. Air flowed from the air supply through ducts and a plenum, through the vocal fold models, to open air. No vocal tract model was used in this experiment, as is common practice in many studies (Pickup and Thomson, 2009; Zhang and Luu, 2012). The duct between the plenum and the models was a flexible PVC tube, 17 cm long and 2.54 cm in diameter.

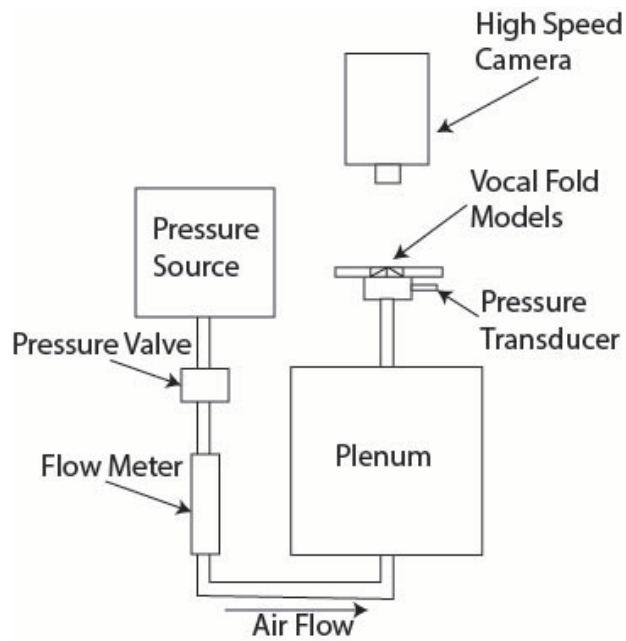


Figure 2.6: Diagram of experimental setup, after Pickup and Thomson (2009).

Each model was tested five times for onset flow rate, offset flow rate, onset pressure, offset pressure, and frequency. Onset and offset flow rate were measured using an Omega FMA-A2323 flow meter. The onset and offset pressures were measured via a pressure transducer (Omega PX138) located approximately 3 cm below the model, flush with the inside of the duct wall upstream of the vocal fold models. The pressure data were displayed by an Omega DP24-E panel meter calibrated to report the pressure in kPa from the voltage received from the pressure transducer. The pressure transducer voltage output was also sent to and processed by a LabVIEW program. Frequency was extracted from the upstream pressure data via LabVIEW. High-speed images were acquired at 110% and 150% of the onset pressure for each of the models. High-speed images were acquired at 3000 fps with a resolution of 512×512 pixels.

2.3 Results and Discussion

2.3.1 Threshold Pressure

Average onset pressure for an adult male is 0.29 to 0.49 kPa (Baken, 1999). As observed in Figure 2.7a, the measured onset pressure for the base models (models 9, 10, and 11; see Table 2.2) was between 0.69 and 0.81 kPa. These values, although higher than onset pressure, are still within the range of lung pressures during normal speech. Note in Figure 2.7a that offset pressure is always lower than onset pressure. The differences between onset and offset pressures are all between 0.22 and 0.47 kPa. It is important to recognize that the onset pressure for the base models was close to the *in vivo* onset pressure range. The pressures do not appear to have an obvious relationship with asymmetry. This can be observed below in that the variation between models of the same type is similar to the variation between models of different asymmetry.

2.3.2 Flow Rate

An estimate of mean airflow during sustained phonation is 6.1-12.8 L/min (Baken, 1999). The flow rates for the models are shown in Figure 2.7b; sustained phonation typically occurs somewhere above the onset flow rate. However, Figure 2.7b reports onset values higher than what is typical primarily because the models did not achieve full closure. However, the flow rates are within the right order of magnitude. There does not appear to be a strong correlation between the flow rate changes and changes in asymmetry. The flow rate varies similarly between identical models and model with different stiffness configurations.

2.3.3 Frequency

The average frequency of an adult male is between approximately 100 and 136 Hz (Baken, 1999). As can be seen in Figure 2.7c, all of the observed frequencies are within or close to this range. In this regard, the models produced in this study are a good representation of adult male human vocal folds. There does not appear to be a strong correlation between asymmetry and frequency.

2.3.4 Model Motion

A convergent/divergent motion was observed in the models. This motion refers to the intraglottal streamwise profile that alternates during oscillation between a convergent shape during glottal opening and divergent during glottal closing. This motion is a manifestation of the mucosal wave present in human vocal folds. The mucosal wave is a vertically-traveling surface wave on the tissue that is often used as a clinical hallmark of healthy phonation. In Figure 2.8 the inferior surface of the model can be seen while the orifice is still open. This creates a divergent orifice profile. In the vocal folds, and possibly in these models, a convergent profile exists during orifice opening as the inferior margins separate before the superior margins separate, although further investigation would be required to verify this.

Amplitude differences can be observed in Figure 2.8 in the asymmetric models: the softer the model, the larger the amplitude of the less stiff side. (These amplitude differences are more readily apparent in the edge tracking shown in Figure 2.10, discussed below.) The cover layer stiffness appears to have a larger effect on the amplitude than the body layer stiffness.

All models exhibited an anterior-posterior zipper-like wave, as seen in Figure 2.8. This type of motion is sometimes observed *in vivo*; however, its cause is unclear. The zipper-like motion was present in all of the models. Therefore, the zipper-like motion is not a product of

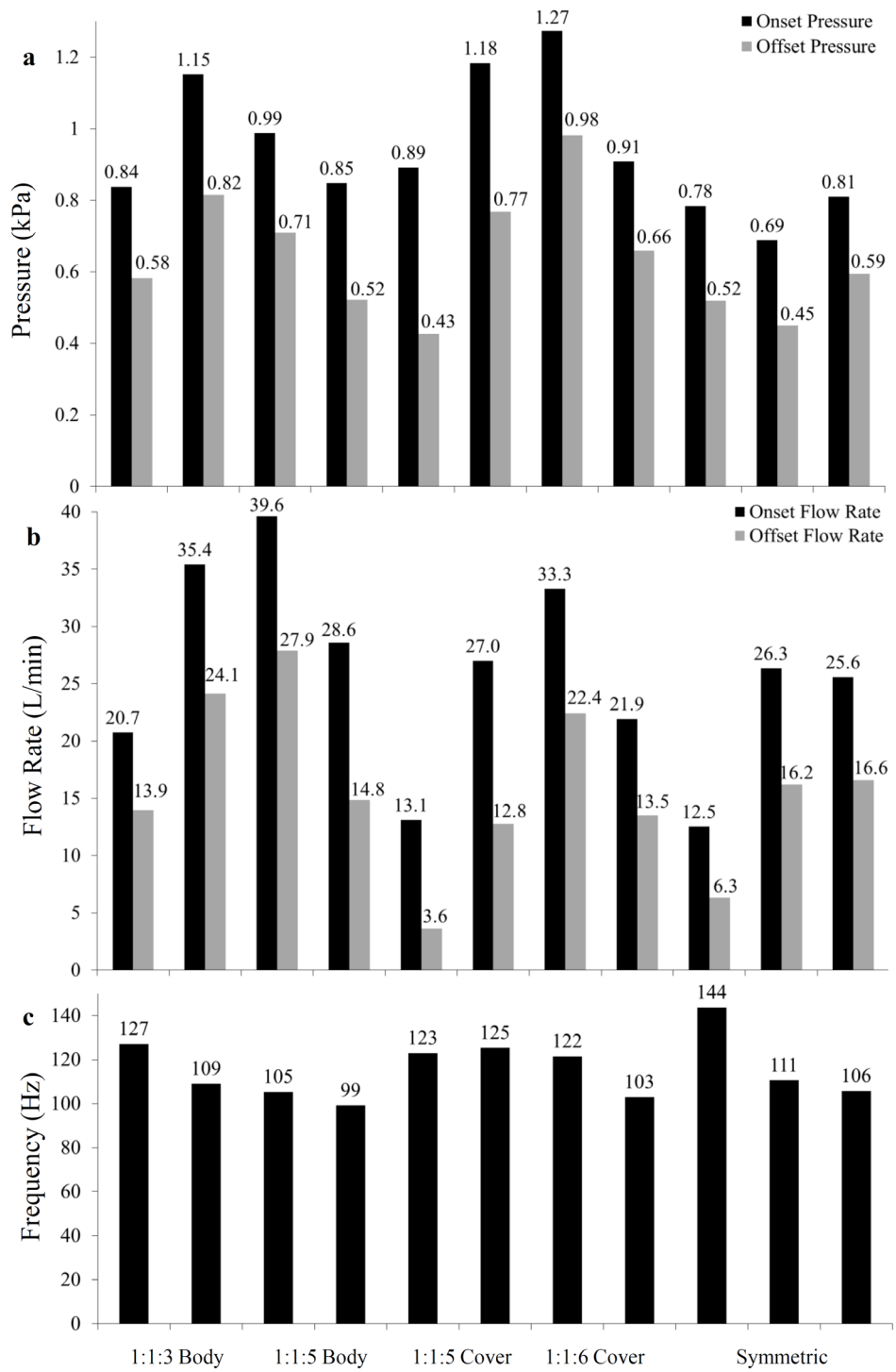


Figure 2.7: a) Pressure, b) flow rate, and c) frequency data.

left-right asymmetry. A proposed explanation of this phenomenon is provided in the discussion section of Chapter 4.

Figure 2.9 shows the edge positions of the models as they are vibrating through two cycles. The edge positions were tracked at the point 1/3 of the length of the vocal fold, measured

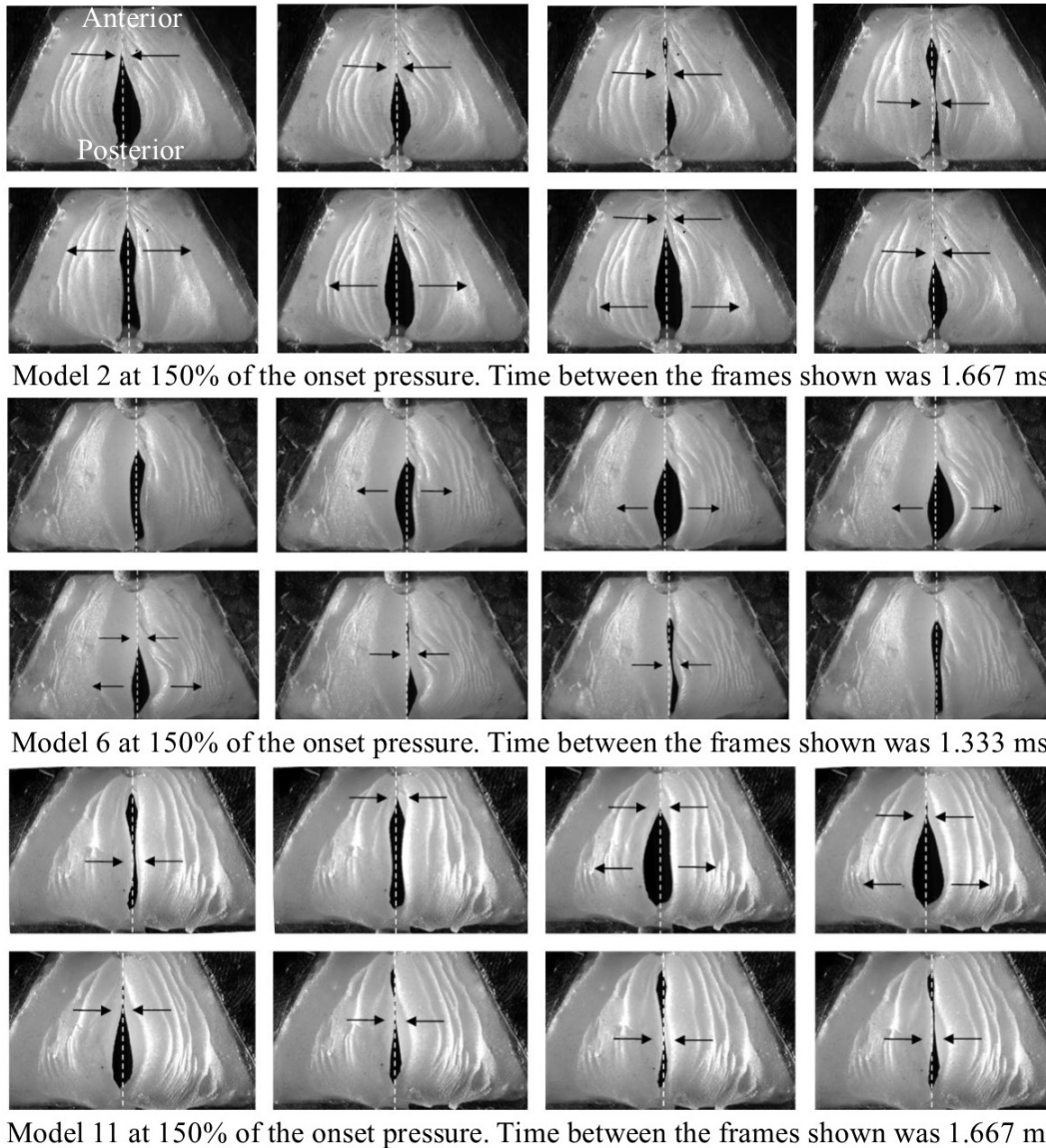


Figure 2.8: Sequence of high-speed images from three models. Asymmetric lateral excursions and variations in anterior-posterior zipper-like motion are evident. The arrows point out the zipper-like motion of the models.

from the posterior side, as shown in Figure 2.10. This is close to where the amplitude is the largest.

A phase shift between left and right edge motion was observed in all of the models. In all of the asymmetric cases, the stiffer model led the less stiff model. The softer models tends to experience a larger amplitude; however, the stiffer model will often cross the mid plane. This is consistent with some of Zhang and Luu's (2012) findings. Zhang and Luu studied left-right stiffness asymmetry in the body layer of a simplified model. Their models were much stiffer than the models used in this study, with Young's modulus values for their standard model being 73.16 kPa and 3.25 kPa for the body and cover layers, respectively. The Young's modulus for the standard model (right fold) used in this study were 3.25 kPa and <1kPa for the body and cover layers, respectively. Despite the overall stiffness differences for these models, the stiffer model led the less stiff model in both studies with comparable left-right stiffness mismatches.

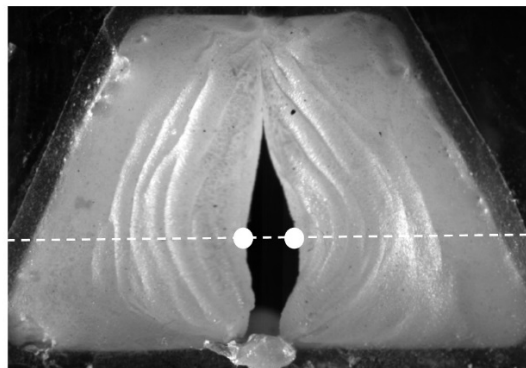


Figure 2.9: Frame from high-speed image sequence, with line indicating anterior-posterior position along which left and right model edges were detected.

2.4 Conclusion

The modified MRI-derived models oscillated at pressures, flow rates, and frequencies that are typical of human phonation. The onset pressures and onset flow rates were higher than *in*

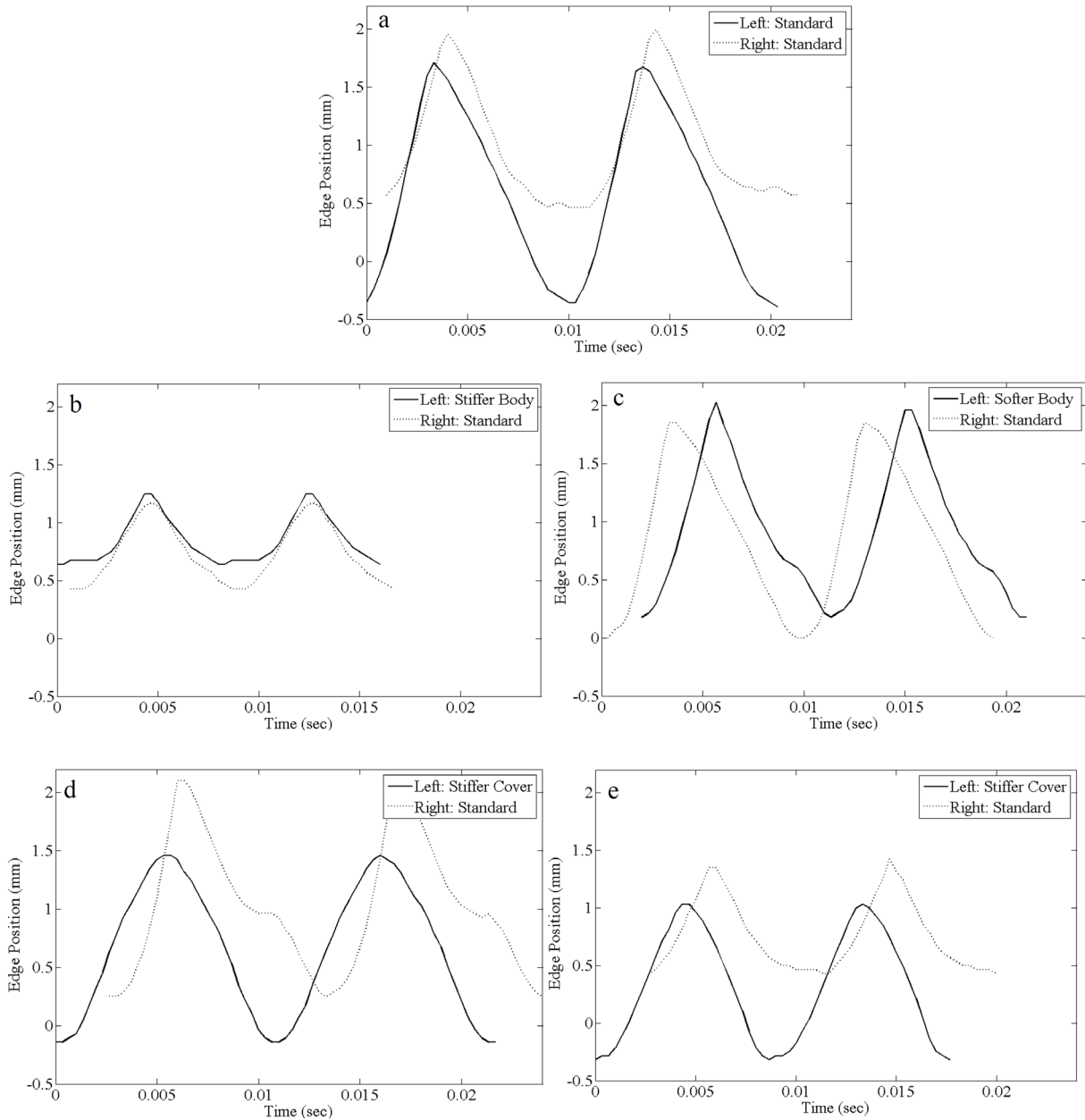


Figure 2.10: Edge positions vs. time for different stiffness configurations. a) Model 11, symmetric case, 1:1:4 Body 1:1:8 Cover. b) Model 2, Left-1:1:3 Body 1:1:8 Cover. c) Model 3, Left-1:1:5 Body 1:1:8 Cover. d) Model 6, Left-1:1:4 Body 1:1:5 Cover. e) Model 8, 1:1:4 Body 1:1:6 Cover.

vivo conditions, but are still within the range of typical human speaking voice. Although the models did not experience complete glottal closure, they did vibrate with patterns that were characteristic of some aspects of model motion, including convergent/divergent motion and an anterior-posterior zipper-like motion. Although the zipper-like motion is not a normal motion in human vocal folds, it can often be observed; the reason for this motion is not known. It is possible that the anterior-posterior geometry variations contribute to this motion in these models (further evidence of this is provided in Chapter 4).

The frequency, onset pressure and flow rate did not show a discernable pattern with asymmetric stiffness variations. There are several possible explanations for this behavior. It is possible that small inconsistencies in these models affected the vibration of the models more than the asymmetry affected motion. It is also possible that frequency, pressure, and flow rate, although common metrics in voice research, might not be telling metrics for this experiment. Glottal area, videokymography, and radiated acoustics might yield more compelling measures of the effect of asymmetry on model vibration. As for the small inconsistencies, Chapter 3 details a new fabrication process designed to improve model consistency.

Although there did not seem to be a significant difference in the frequency and onset pressure of the asymmetric pairs, the high-speed data exhibited interesting results. Differences in amplitude and lateral and anterior-posterior wave motion for the various asymmetrical conditions were observed. In all of the asymmetric cases, the less stiff model experienced larger amplitude.

The results of this study add to the research presented in the introduction of this chapter. Future research includes an investigation into the interaction between body layer and cover layer stiffness in an asymmetry study; i.e., a study in which the body and cover layer stiffness values

in one of the models are varied together. Further work and studies should be done with this modified MRI-based model due to the realistic metrics and motion that were observed.

3 EXPENDABLE MOLD FABRICATION PROCESS

3.1 Introduction

Synthetic models of human vocal folds are important tools in the study of voice production and are used to understand the effects of geometry, stiffness, and other parameters on vocal fold vibration. Although stiffness can be easily varied with the current model fabrication process, geometry variations are more complex, thus limiting the turnaround time in generating models with different geometries. Many geometric iterations will be required in order to eventually find an ideal geometry and material property combination that most closely mimics the structure and response of the vocal folds. Further, to better understand the effect of vibration on vocal fold cells, hybrid models that are part synthetic and part biological are desired. The current modeling process has limitations that prevent inclusion of viable, biological materials. In this chapter a redesign of the current modeling process that solves the problems mentioned above, as well as several other weaknesses of the current process, is described.

3.2 Old Process for Fabricating Vocal Fold Models

The process for fabricating vocal fold models that was used prior to this thesis research is listed below. The strengths and weaknesses are then discussed. A more detailed description of this process is contained in Murray and Thomson (2011).

1. Three-dimensional geometry (e.g., CAD-generated or MRI-derived) of the model was created.
2. Three-dimensional geometry was exported as a stereolithography (.stl) file to a 3D printer for printing of a model positive in acrylonitrile butadiene styrene (ABS) plastic (see Figure 3.1).
3. The ABS positive was used to create a mold out of Smooth-Sil 950 platinum silicone rubber, a silicone rubber material with an approximate Shore A hardness of 50 (Smooth-On, Inc.; Easton, PA).
4. Pol-Ease 2300 Release Agent was sprayed into the molds (Polytek Development Corp.; Easton, PA).
5. Ecoflex 00-30 Supersoft Platinum Silicone, a two part silicone (also by Smooth-On) was mixed with Smooth-On Silicone Thinner. The thinner changes the material properties of the silicone. The more thinner that is used, the lower the Young's modulus of the resultant material.
6. Before curing, the Ecoflex and thinner mixture was degassed.
7. The mixture was poured into the mold.
8. Molds containing the mixture were placed in an oven to heat cure.
9. Once the silicone was cured, the body layer was peeled out of the mold.
10. Steps 4-6 were repeated for the next layer.
11. Once the silicone for the next layer was poured, the body layer was placed into the next mold, making sure the alignment wings were properly place in the mold. (The alignment wings are shown in Figure 3.1.)
12. Steps 8 and 9 were repeated.

13. If additional layers were desired, steps 10-12 were repeated until the desired number of layers was achieved.
14. The alignment wings on either side of the model were removed from the models using a scalpel.
15. 1:1:1 Dragon Skin (Smooth-On, Inc.; Easton, PA) was mixed and degassed.
16. The Dragon Skin was poured over the top of the models and allowed to run down over the edges to form a very thin layer. This layer represents the epithelium.
17. This layer was cured for 2 hours at room temperature.
18. Steps 15 through 17 were repeated once. The resultant epithelium was approximately 80-120 μm thick.
19. The model was glued to a cavity in the mounting plates such that there were anterior, posterior and lateral fixed boundaries.
20. The models were coated with baby powder to reduce surface tackiness.

The old fabrication process is also shown in Figure 3.2. Often flaws would result from this process, including bubbles, separation between the layers, gaps, or other geometric flaws. In this event, the flawed models were discarded and the process was restarted.

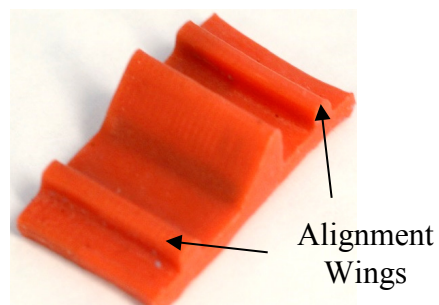


Figure 3.1: 3D printed positive of the model made from ABS plastic.

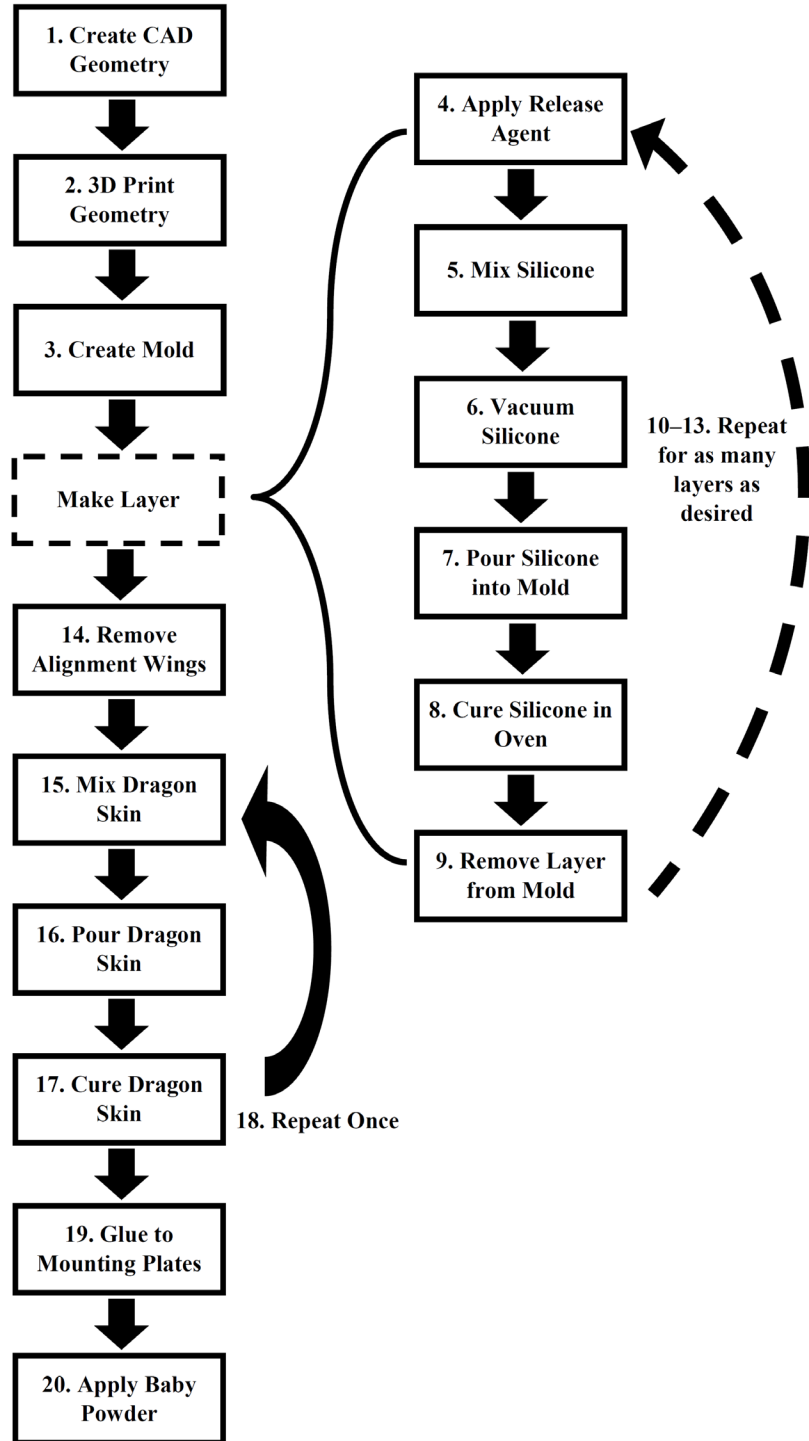


Figure 3.2: Old process for synthetic model fabrication.

Experience has shown that there is significant opportunity for human error in the process described above. Skill and precision are required to successfully create synthetic vocal fold models. Poor repeatability translates to wasted time and to difficulty in improving and testing the models, ultimately limiting the utility of vocal fold models in voice research.

Some of the most significant obstacles in this process are caused by the release agent that is applied to each mold before pouring the silicone mixture. Release agent is applied to enable removing the model from the mold without damaging the model. However, release agent causes two problems. First, too much release agent can prevent the silicone from curing, especially in the mixtures with higher thinner ratios. Second, a hybrid vocal fold model consisting of synthetic and biological materials is desired to enable the study of cell response to vibration. However, release agent is toxic to the cells that will be used in the models. Thus it is desirable for models to be made without the use of release agent.

3.3 New Process for Fabricating Vocal Fold Models

A significant portion of this thesis was to develop a new fabrication process that minimized some of the limitations of the old process. The following design goals were set: eliminate the need for release agent, improve alignment of the models, enable more convenient varying of geometry, and decrease fabrication time.

Eliminating release agent and varying the geometry led to two obvious options for the model building process: an additive process, such as 3D printing, or a lost mold process. The author was an assistant coach of a capstone team that pursued development of a 3D printer for vocal fold model fabrication. The team fabricated a prototype 3D printer. However, technical difficulties associated with printing uncured silicone prevented the printer from printing models with the required precision. The uncured silicone was not sufficiently viscous and the silicone

could not be cured quickly enough for 3D printing to be a viable option. Therefore, a process with a dispensable mold was pursued.

The mold material that was selected was a powdered sugar and water mixture. This was suitable for a mold material because it is water soluble, does not react with the silicone, and is not toxic to cells. In order to separate cured silicone from the mold, the mold needed to be dissolved in a substance that would not also dissolve the model material and that would not be toxic to cells. Water was the simplest choice that met these requirements.

The powdered sugar-to-water ratio was experimented with until a material was found that was hard enough to machine well and dense enough to hold the silicone. The powdered sugar molds were made from an unpacked powdered sugar-to-water ratio of 24:1 by weight (approximately 48:1 by volume). This is equivalent to 1 cup of unpacked powdered sugar to 1 tsp of water. Since there was such a small amount of water, a drop of food coloring was added to the water to visually confirm that the powdered sugar and water were adequately mixed. The mixture was poured into the milling fixture, which also served as the mold to create the powdered sugar bricks (see Figure 3.3). Approximately $\frac{2}{5}$ cup (48 g) of the mixture was required to make one brick. The mixture was packed using the compacting piece shown in Figure 3.3 until the mixture was solid. The volume of the packed mixture was about half of what it was before packing. The mixture was dried in an oven for 10 minutes at 175°F before being removed from the milling fixture. The brick was then left to dry overnight.

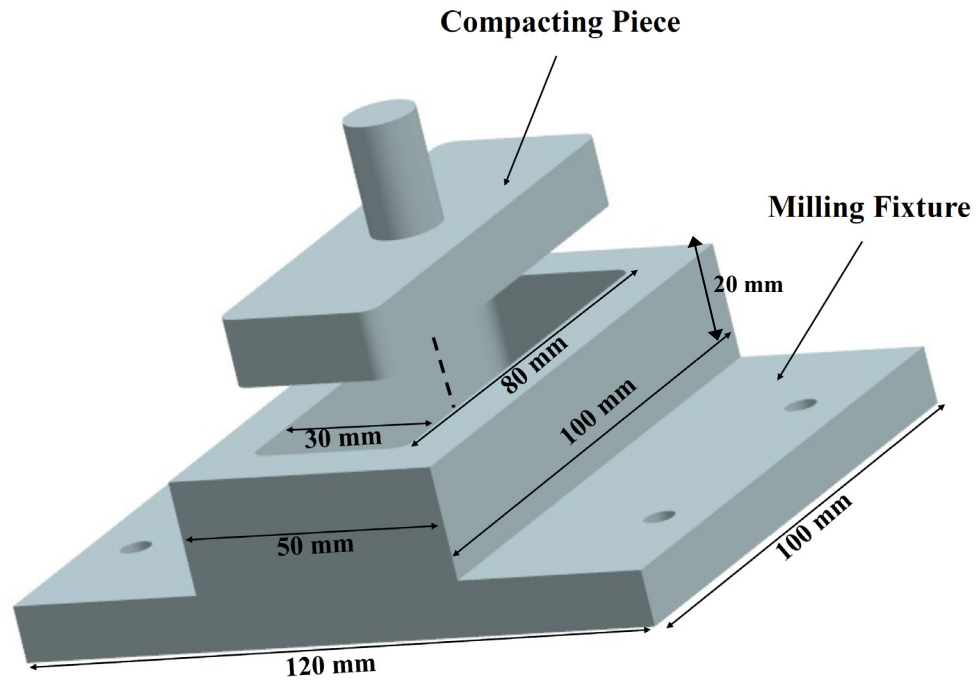


Figure 3.3: Aluminum milling fixture and compacting piece used for building powdered sugar bricks.

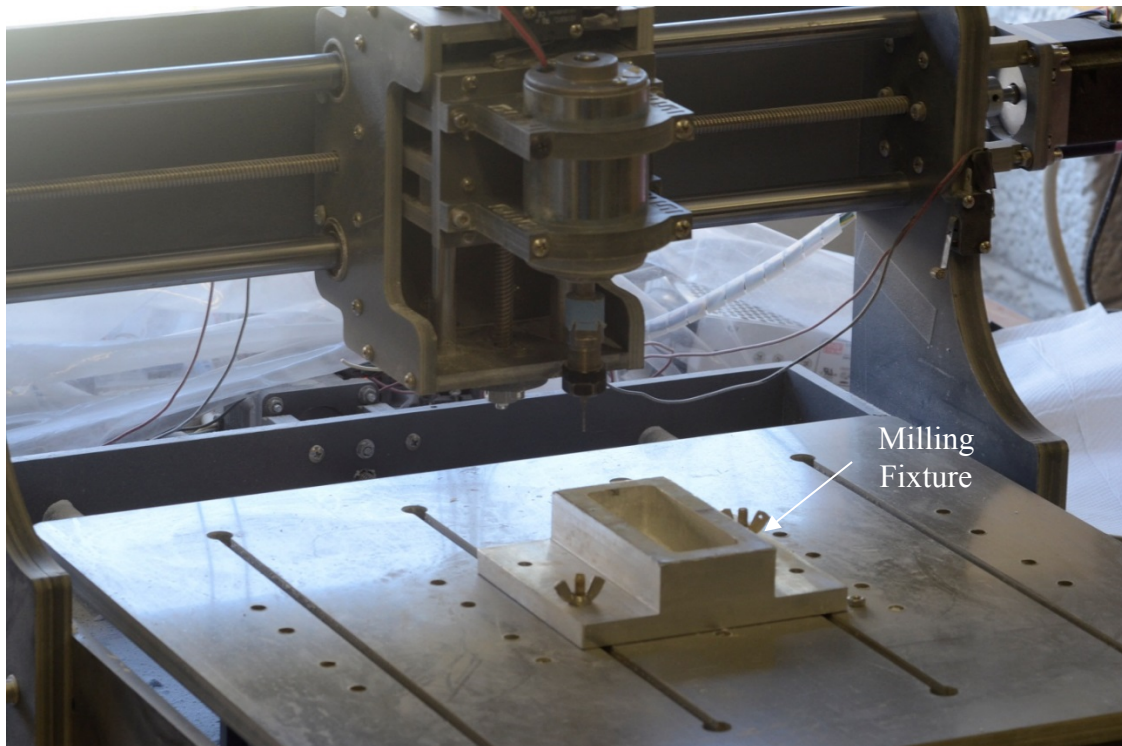


Figure 3.4: A picture of the CNC table top mill with the brick milling fixture attached.

3.3.1 Milling Equipment and Protocol

A three-axis CNC mill (Zen Toolworks 12 X 12 F8, <http://www.zentoolworks.com>) was assembled. The mill was controlled by Mach3 CNC Control Software (<http://www.machsupport.com>). Specifications for the mill and computer setup can be found in Appendices D and E. The geometry of the models was first created in the CAD system Siemens NX 8.0 and exported as a stereolithography (.stl) file. The exported geometry was a model of the brick with the shape of the vocal fold as negative space (see Figure 3.5). Notice in Figure 3.5 that not only did the negative include the model geometry, but also that of the top plate (described below). The interaction between the plate and the mold was a sliding fit of 0.2 mm. The .stl file was converted to G-code by Vectric Cut3D (<http://www.vectric.com>).

Two different cuts were performed by the mill, a rough cut and a finishing cut. The rough cut was performed using a 1.5 mm tungsten steel carbide PCB CNC end mill (<http://www.amazon.com>) with a step size of 0.5 mm in the Z direction (see coordinate system in Figure 3.5). This cut was performed in the X direction. The spindle speed for the rough cut was 8600 rpm and the feed rate was 600 mm/min. The more precise finishing cut was performed in the Y-direction with a 1 mm diameter tungsten carbide drill with a 10.5 mm cut length (<http://www.kentsupplies.com>). The overlap between passes was 40%, with a spindle speed of 8600 rpm and feed rate of 40 mm/min.

Milling a cavity or negative of the model allows for models with different geometries to be fabricated more easily and inexpensively. Rather than requiring a 3D-printed positive of the model (as in the old process), this new process calls for the negative of the model to be milled in the powdered sugar brick. This process is cheaper and has a faster turnaround time than 3D printing, since with the old process, creating models with a different geometry required the 3D

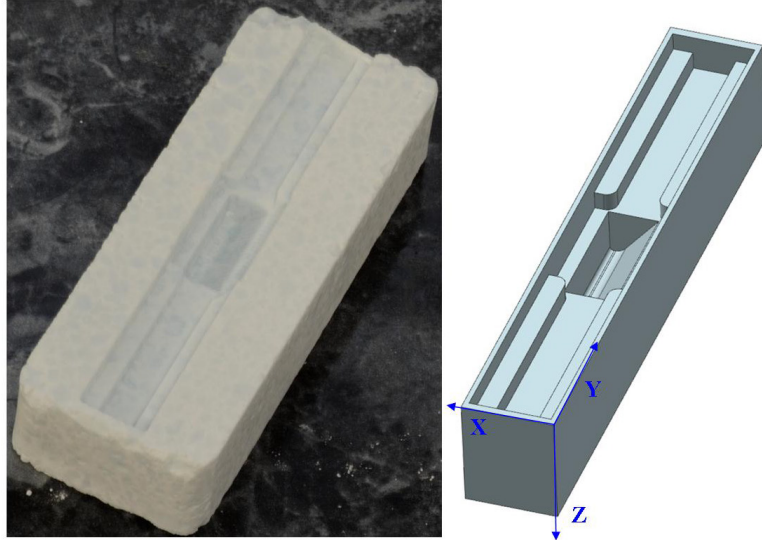


Figure 3.5: Powdered sugar mold (left) and CAD model (right) of the mold.

printed positives of the shape to be ordered and created (which can take days and is very expensive) and create a Smooth-Sil mold using those positives (which takes about one day and is also more costly than sugar). The only time added to create a new geometry for the new process was the time to create G-Code from the CAD geometry, which was typically less than 10 minutes. Milling the cavity shown in Figure 3.5 could be accomplished in approximately 30 minutes. However, a 5-bit array has recently been constructed and incorporated into the mill so that five molds can be milled simultaneously (see Figure 3.6).

Consistent alignment was insured and the need to glue the model to the mounting plates was eliminated by inserting the mounting plates directly into the molds to allow the silicone to cure directly to the plates. In the old process, alignment between the layers of the models was dependent on the alignment wings interfacing properly with the Smooth-Sil mold. Since both models and molds were made of a soft silicone, there was room for misalignment between the

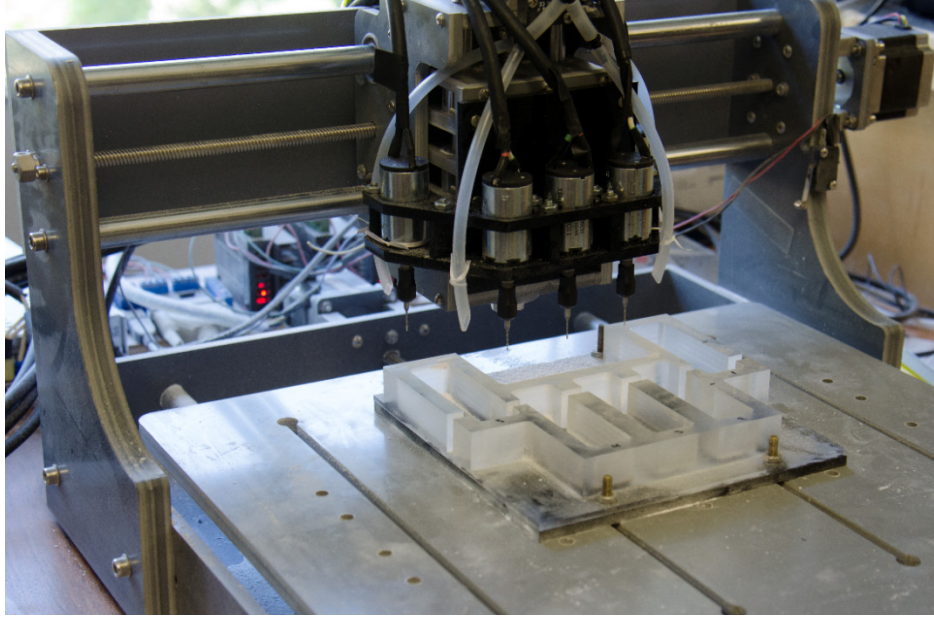


Figure 3.6: CNC mill with 5-bit array adaptation and milling fixture.

layers. Also, gluing the models into the mounting plates was imprecise. In the new process, the silicone is cured directly to the mounting plate. The powdered sugar molds interface with the mounting plates to ensure alignment consistency through the fabrication steps of each of the layers of the models. The side plates were glued onto the sides of the completed vocal fold models. Thus alignment is not only more consistent through the layers of the models, but the model position relative to the mounting plates is the same throughout all of the models.

In the old fabrication process, the models had three rigid attachments on the anterior, posterior, and lateral sides. These boundary conditions were maintained in the process redesign. However, since the plate and mold needed to directly interface, the sides of the plate that provide anterior and posterior boundary conditions were designed to be added after the vocal fold model had been cast (see Figure 3.7). The area on the main mounting plate to which the silicone was cured had a pattern etched by a laser cutter, increasing the area to which the silicone could cure and adhere (see drawings in Appendix C). Once the model was cured, the sides of the plates

were glued to the sides of the model, providing the anterior-posterior rigid attachments. The glue used to attach the model to rigid surfaces was Sil-Poxy (Smooth-on, Inc.; Easton, PA). There were grooves on the main plate that matched those on the sides, such that the sides could slide onto the main plate.

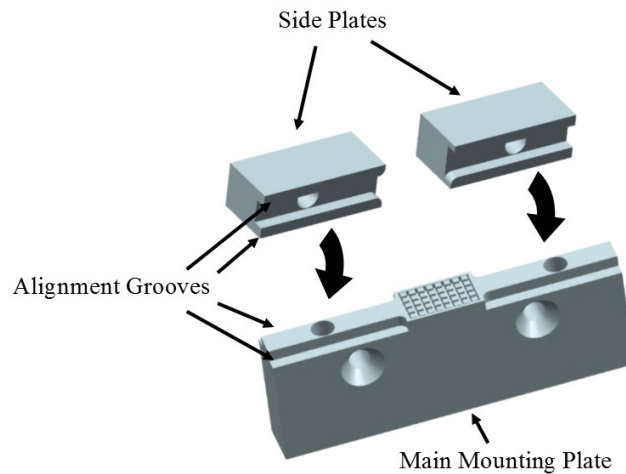


Figure 3.7: Side and main mounting plate assembly.

3.3.2 Detailed Description of New Modeling Process:

1. CAD geometry was exported as an .stl file.
2. The .stl file was imported into Vector Cut3D to convert the .stl file to a G-code.
3. 1 tsp of water and one drop of food coloring was thoroughly mixed with 1 cup of unpacked powdered sugar.
4. The powdered sugar and water mixture was packed into the milling fixture.
5. The brick was dried in the oven for 10 min and then overnight at room temperature.
6. The brick was milled into the desired geometry and cleaned with pressurized air so that no loose powdered sugar remained.

7. Ecoflex 0030 two-part silicone was mixed with thinner.
8. The mixture of Ecoflex and thinner was degassed.
9. The mixture was poured into the body layer mold.
10. The main mounting plate was placed in the mold with the alignment grooves in the milled brick aligned with the plate grooves.
11. Block and silicone were placed in the oven for appropriate amount of time for the mixture ratios of the silicone (30-90 min). Details for curing time for different ratios can be found in Appendix C.
12. Once the silicone was cured, the powdered sugar mold was dissolved in warm water.
13. Steps 7-12 were repeated until the desired number of layers was reached.
14. The side plates were glued onto the sides of the model and the main plate, causing there to be anterior, posterior and lateral rigid boundaries.
15. 1:1:1 Dragon Skin® 10 Fast was mixed and degassed.
16. The Dragon Skin® 10 Fast was poured over the top of the models and allowed to run down over the edges to form a very thin layer modeling the epithelium.
17. This layer was cured for 2 hours at room temperature.
18. Steps 15 through 17 were repeated once. The resultant epithelium was approximately 80-120 μm thick.
19. The models were coated with baby powder to reduce surface tackiness.

3.4 Conclusion

The new model fabrication process solved many of the problems of the old process, including eliminating release agent, enabling convenient variation of geometry, improving model alignment, decreasing fabrication time and cost, and avoiding some of the material deformation

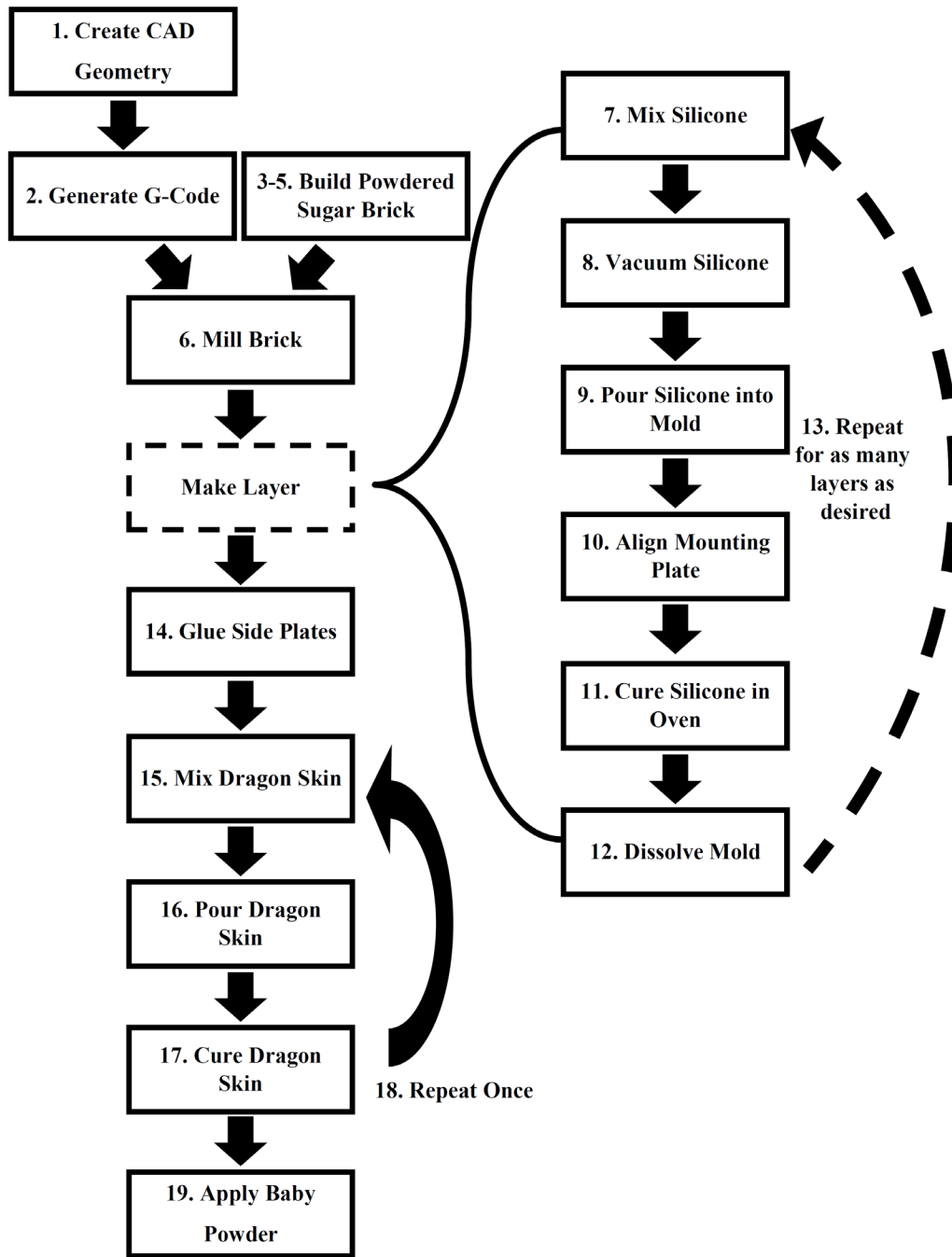


Figure 3.8: New process for synthetic model fabrication.

that resulted from removal from the mold. The new process will enable geometry variation studies by decreasing cost and turnaround time, which in turn will enable further research in geometric improvements to the synthetic vocal fold models. It is anticipated that this new process will enable researchers to build hybrid biological and synthetic models that can be used to study the effects of vibration on live cell response.

4 COVER LAYER THICKNESS VARIATION AND ASYMMETRY

4.1 Introduction

This chapter focuses on cover layer geometry variation and asymmetry in a simplified, synthetic self-oscillating vocal fold model.

Proper geometry definition is an essential component of synthetic vocal fold modeling. However, defining geometry for vocal fold models is a difficult task, as shown by Bhattacharya and Siegmund (2012), who attempted to define a simplified synthetic model geometry based on medical image data. In voice research, simplified models are often used. The responses of self-oscillating models with different geometries have been compared experimentally (Murray and Thomson, 2012), but geometry asymmetry has only been studied using either computational models (Scherer et al., 2001; Cook et al., 2009; Pickup and Thomson, 2011; Smith and Thomson, 2012) or experimental, non-self-oscillating models (Chan et al., 1997; Scherer et al., 2001; Shaw et al., 2010; Murray and Thomson, 2012; Xuan and Zhang, 2014).

Cook et al. (2009) used a computational model based on the so-called “M5” simplified vocal fold model (Scherer et al., 2001) to investigate the effect that geometry changes, layer stiffness, and other parameters have on vibration. Using three different methods, five parameters were consistently found to be the most important: longitudinal shear modulus, transverse Young’s modulus, cover stiffness, degree of transition function, and length. Also, Pickup and Thomson (2011) computationally varied geometric parameters to better understand the effect of

model geometry on motion. The geometric parameters that affected vibration the most were related to the outer, cover layer geometry; specifically, these included the intraglottal cover layer angle and the inferior glottal angle. In addition, Smith and Thomson (2012) performed a computational study determining the effect that changing the inferior glottal angle had on model vibration and, contrary to Pickup and Thomson (2011), found that the inferior glottal angle itself did not significantly influence the vibratory characteristics. Changing inferior glottal angle causes changes in vocal fold mass and stiffness. The Smith and Thomson (2012) simulations included those changes, while the Pickup and Thomson (2011) simulations did not, which accounts for the discrepancy between the two study results.

Fewer experimental studies have included variations in geometry as extensively as the previously mentioned computational studies. Varying geometry in a physical experiment can be more difficult and time consuming than in computational experiments. Scherer et al. (2001) investigated the effect of glottis shape on intraglottal pressure profiles in a rigid model with either a divergent-symmetric or oblique glottis. Chan et al. (1997) varied thickness of the epithelium in a rigid body, fluid cover layer setup, but only two epithelium thicknesses were tested. It was found that epithelium thickness directly affected onset pressure. Murray et al. (2014) investigated the effect of vocal bowing (a geometric variation) on vibratory mechanics using a simplified self-oscillating model. Bowing appeared to affect onset pressure, flow rate, and frequency (Murray et al., 2014). Murray and Thomson (2012) studied vibratory differences in four different established model geometries, including an MRI-based model, a normal “M5” model (designed in Scherer et al., 2001), a modified (convergent) “M5” model, and a multi-layer (EPI) model. The so-called “EPI” model showed convergent-divergent vibratory motion

reminiscent of a mucosal wave, along with onset pressure and frequency within the range of normal human phonation (Murray and Thomson, 2012).

In addition to geometry variation, experiments to replicate anisotropy, anterior-posterior tension, and other material properties, such as non-linear stress-strain relationships, have been performed. Anisotropy and tension can be introduced by including fibers in the models and adjusting the model mounting apparatus. Shaw et al. (2012) changed tension in a set of models with and without fibers. The changing tension had a larger effect on frequency in the models containing fibers. Xuan and Zhang (2014) experimented with short (4 mm) fiber bundles to introduce anisotropy into the models. They found that adding fibers facilitated complete glottal closure during vibration.

Although stiffness asymmetry has been previously studied (Alipour et al., 2000; Pickup and Thomson, 2009; Xue et al., 2010; Zhang, 2010; Zhang and Luu, 2012; Zhang et al., 2013), to our knowledge, anterior-posterior geometry asymmetry (i.e., a varying geometry in the anterior-posterior direction), does not appear to have been previously studied. This is, in part, due to the complexity of fabricating and developing models with anterior-posterior asymmetry. However, left-right asymmetry has been studied using both computational (Alipour et al., 2000; Xue et al., 2010) and experimental (Pickup and Thomson, 2009; Zhang, 2010; Zhang and Luu, 2012; Zhang et al., 2013) models. Xue et al. (2010) computationally studied tension asymmetry, finding that asymmetric tension increases onset pressure. Alipour et al. (2000) studied left-right asymmetry and anisotropy in a finite element model.

Pickup and Thomson (2009) varied cover layer stiffness asymmetry in a simplified, physical, self-oscillating model. Increased asymmetry was found to increase the phase difference between opposing vocal folds. Left-right asymmetry in the body layer has also been examined

(Zhang, 2010; Zhang and Luu, 2012; Zhang et al., 2013). Zhang and Luu (2012) also used a simplified, physical, self-oscillating model to investigate body layer stiffness asymmetry, finding that increased left-right asymmetry in the body layer also led to increased phase difference. Zhang et al. (2013) used a similar asymmetric model to perform human perceptual testing on the different models. They concluded that in most cases, phase shifts and amplitude differences did not affect human perception of the sound. Zhang (2010) studied the effect of a rigid vs. soft body layer. The asymmetry caused a phase shift between models where the dominant (leading) fold changed based on the subglottal pressure.

Anterior-posterior geometric asymmetry cannot be modeled efficiently using existing fabrication processes because they are not conducive to varying geometry in the required manner. As described in Chapter 3, synthetic vocal fold model geometry changes are time-consuming and costly. The new fabrication process described in Chapter 3 enables geometry to be varied from model to model without significant additions in time or cost. Utilizing the modeling techniques described in Chapter 3, an experiment investigating the effect of cover layer thickness and cover layer thickness anterior-posterior asymmetry on vocal fold motion and other vibratory metrics was conducted. In this chapter the experimental methods and results are presented and discussed.

4.2 Methods

4.2.1 Model Design

The models used for this study were designed to facilitate an understanding of the effect of varying geometry, specifically cover layer thickness, on vocal fold motion. Three-layer models were used. The body layer represented the muscle and ligament layers of the vocal fold,

the cover layer represented the superficial lamina propria, and the epithelial layer represented the epithelium. The outer geometry of the model was kept constant. The outer geometry was based on the so-called “EPI” model (Murray and Thomson, 2012); see Figure 4.1. In order to study the effect of cover layer thickness while maintaining constant outside geometry, the body layer geometry was adjusted. The body layer in the model used for this study combined the geometry of the body and ligament layers of the EPI model.

The Young’s modulus value of each of the layers is given in Table 4.1. These values were obtained using the same method described in Chapter 2. The body layer was 1:1:1 (Part A:Part B:Thinner) of Smooth-On Ecoflex® 0030. The cover layer was 1:1:8 of Ecoflex® 0030. A thin (estimated 100 µm thick) epithelial layer, 1:1:1 of Smooth-On Dragon Skin® 10, was applied to the outside of the cover layer as described in Chapter 2. The models were fabricated using the process described in Chapter 3.

Seven different cover layer thickness configurations were studied: five symmetric and two anteriorly-posteriorly asymmetric (see Table 4.2 and Figure 4.1). The thickness in both asymmetric cases varied linearly along the anterior-posterior direction. The anterior-most and posterior-most dimensions in these two cases corresponded to the thickness dimensions in four of the symmetric cases. The additional symmetric case was the “standard” thickness (2.1 mm) of the EPI model. Three replications of each model configuration were fabricated and tested.

Table 4.1: Young’s modulus values of the different silicone mixing ratios used in the models.

Layer	Ratio	Young’s modulus (kPa)
Body	1:1:1 Ecoflex	6.6 kPa
Cover	1:1:8 Ecoflex	<1 kPa
Epithelium	1:1:1 Dragon Skin	33.2 kPa

Table 4.2: Cover layer thickness cases.

Cases	Cover Layer Thickness
Uniform Thickness	0.5 mm
	1.05 mm
	2.1 mm
	3.15 mm
	3.7 mm
Asymmetric Thickness	Anterior = 0.5 mm, Posterior = 3.7 mm
	Anterior = 1.05 mm, Posterior = 3.15 mm

4.2.2 Experimental Setup and Procedure

The experimental setup is illustrated in Figure 4.2. Air flowed from the air supply, to the plenum through the duct, and through the vocal folds to open air. No vocal tract model was used. The circular duct between the plenum and the models was clear, flexible PVC tubing, 17 cm long with a 2.54 cm diameter.

An Omega PX138 pressure transducer was located subglottally, 3 cm upstream of the models. The pressure data from this transducer were sent to a LabVIEW program and displayed by a calibrated Omega DP24-E panel meter. Onset and offset flow rate were measured at the air source using an Omega FMA-A2323 flow meter and collected in LabVIEW. A microphone, Larson Davis PRM910B 0179, located approximately 12 cm downstream of the models, was used to verify the frequency measured by the pressure transducer.

The air flow was gradually increased until vibration commenced and then decreased until vibration stopped. In this manner each model was tested three times for onset pressure, offset pressure, onset flow rate, offset flow rate, and frequency. The LabVIEW program analyzed the data from the flow meter, pressure transducer, and microphone. The flow meter and pressure

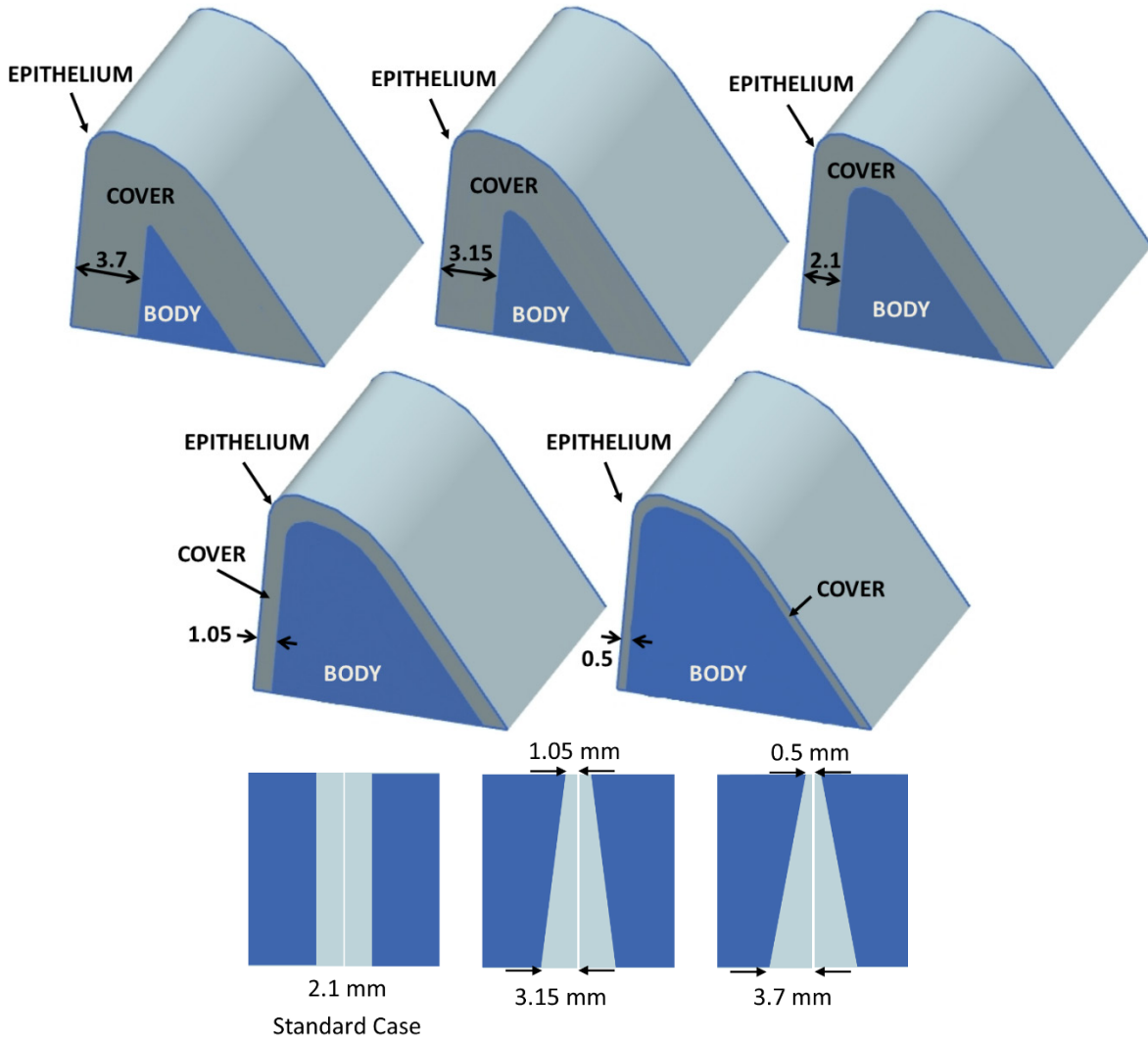


Figure 4.1: Cover layer thickness and geometries. Dimensions are in mm.

transducer data were sampled at 100 kHz. Frequency was extracted from the acquired pressure waveforms. The time, raw flow meter and pressure transducer data, frequency from pressure, frequency from microphone, pressure, and flow rate data were sent every 1/10 sec to an Excel spreadsheet.

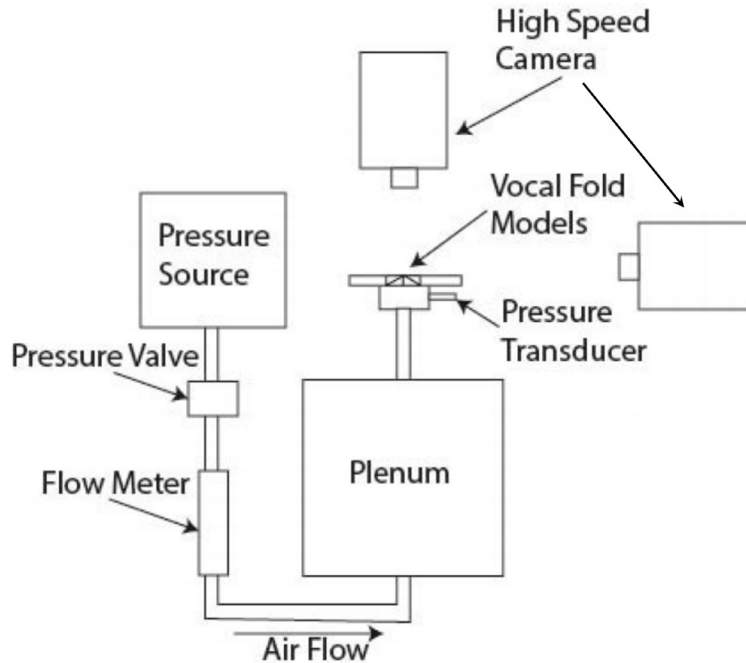


Figure 4.2: Experimental setup.

High speed image data were collected at 110% of the onset pressure. As shown in Figure 4.2, one camera was located above the vocal fold models to record a superior view of the models. The second camera was located to the side of the models to observe the vertical displacement of the models.

The high speed data from the superior view were analyzed using a MATLAB program found in Appendix B. This program found the glottal area and tracked the position of the edge of the glottal area relative to the medial plane at a given (typically the center) point on the vocal folds.

4.3 Results and Discussion

4.3.1 Threshold Pressure

In Figure 4.3a, the average onset and offset pressures for each set of cover layer thicknesses are shown. As stated in Chapter 2, the average onset pressure for an adult male is between 0.29 to 0.49 kPa (Baken, 1999). All of the collected onset pressures are above this range, but the pressures are still within the range of human voicing (e.g., loud speech or singing).

The cover layer geometry had a large effect on the model's vibratory parameters. For the thinner cover layer models, the onset pressure range was much higher than for the standard thickness model. The thicker cover layer models experienced lower subglottal onset pressures than the thinner cases, but higher than the standard. This is related to the role that each layer must play in model vibration. With the thinner cases, the body layer vibrates more than it would in the standard case. Since the cover layer is thin and the stiffer body layer is larger, more air pressure is required to vibrate the model than in the standard model. The opposite is true with the thicker cover layers. The models separate more easily, but this did not translate into lower onset pressure, presumably due to significant alterations in intraglottal geometry caused by extreme cover layer deformation. It is known that intraglottal geometry plays a significant role in governing onset pressure. The standard thickness models had the smallest onset pressures. This suggests that the cover layer thickness is close to ideal for mimicking onset pressures for this outer geometry and stiffness configuration. The asymmetric cases required a large subglottal pressure for phonation. In fact, only the 0.5 mm symmetric case required a larger pressure than the asymmetric cases.

4.3.2 Flow Rate

The estimated mean airflow during sustained phonation for an adult male is 6.1-12.8 L/min (Baken 1999). The onset and offset flow rates shown below (Figure 4.3b) were outside of this range, attributed to the models not achieving full glottal closure. The standard 2.1 mm cover layer thickness model yielded the lowest required flow rate. In all of the cases of the thickest (3.7 mm) cover layer and one of the asymmetric case 2 models, the models' onset pressures were actually higher than the air supply's upper limits. However, these models started vibrating when manually perturbed. Thus the flow rates recorded below reflect only a part of the entire onset flow rate range for the 3.7 mm case. Again the asymmetric cases have a large flow rate. Note that with asymmetry case 2 (1.05-3.15 mm), this value is higher than either of its corresponding symmetric cases (1.05 and 3.15 mm), indicating that the increased flow rate is related to asymmetry.

Both phonation flow rate and pressure are higher in the asymmetric cases. If this were to occur *in vivo*, asymmetry would likely cause labored (high onset lung pressure), breathy (high flow rate without glottal closure) speech.

4.3.3 Frequency

As stated in Chapter 2, the average frequency of an adult male voice during speech is approximately 100-136.2 Hz (Baken, 1999). The standard cover layer thickness model (2.1 mm) vibrated at 117 Hz, which is within this range. In contrast, the thinner cover layer models vibrated at a much higher frequency. Interestingly, the asymmetric cases vibrated within the normal frequency range.

Based on changes in stiffness and vibrating mass, the models with the uniform cover layer were expected to behave as the data show. The standard case has an almost optimum

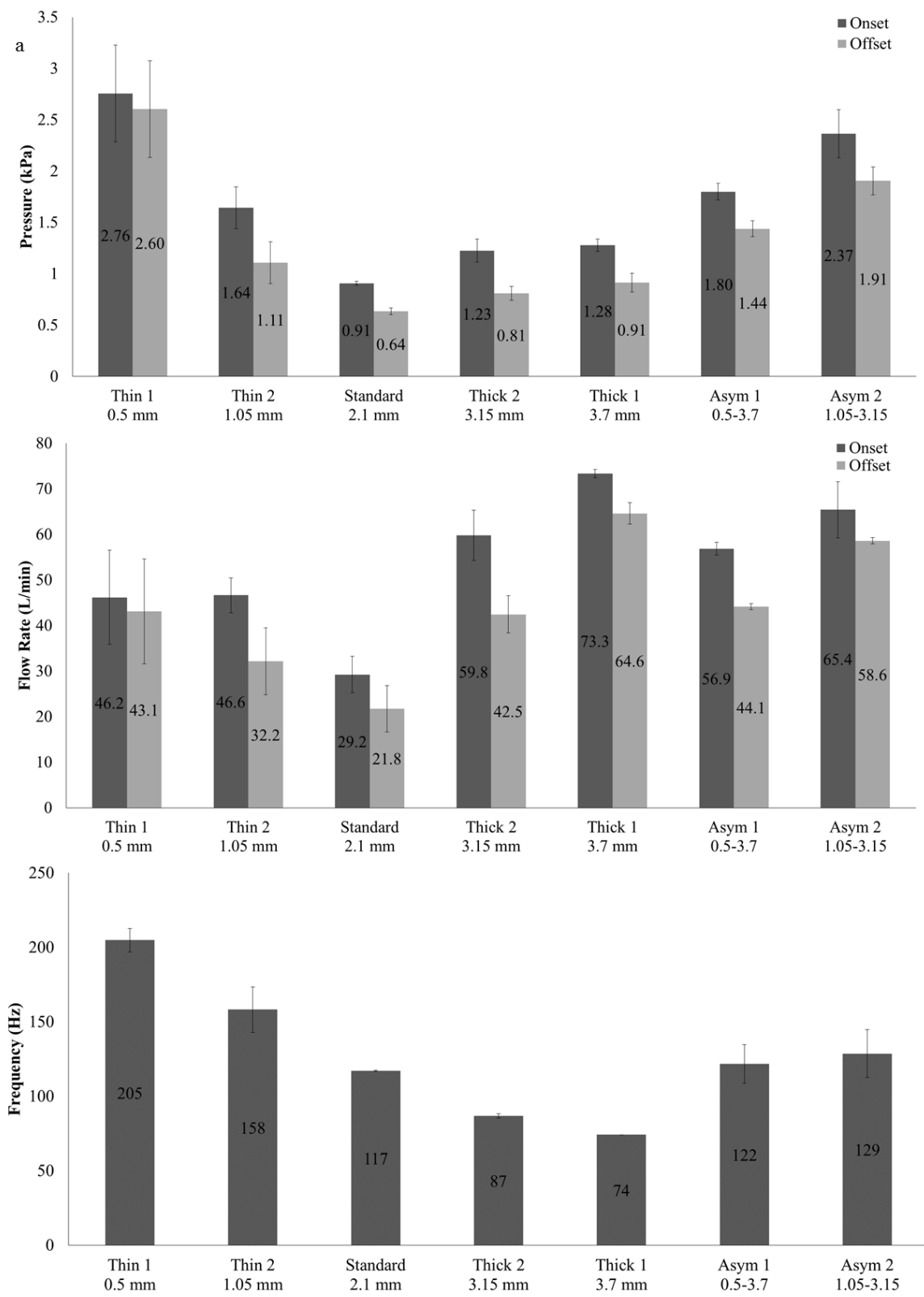


Figure 4.3: a) Average onset and offset pressure data (in kPa). b) Average onset and offset flow rate data (in L/min). c) Average frequency data (Hz).

trade-off between stiffness and vibrating mass for this configuration, which is why the vibration of the standard cover layer thickness model is more realistic than the other models.

4.3.4 Model Motion

Figures 4.4 through 4.10 contain a series of high speed images of the superior and side views, and of edge tracking data for the different cases. First, Figure 4.4 shows the standard cover layer. Notice in Figure 4.4a that the model did not experience full glottal closure and vibrated symmetrically in the anterior-posterior direction. There is a small amount of convergent/divergent motion present in this model. As can be observed in Figure 4.4b, there was some vertical displacement as the model opened. Figure 4.4c shows the distance of the edges of vocal folds from the medial center line between the two folds (solid red line shown in Figure 4.4a); the data are measured along the anterior-posterior midplane of the vocal folds (dotted red line in Figure 4.4a). Figure 4.4 shows that the model vibrated nearly symmetrically in the left-right direction.

The thinnest cover layer models (0.5 mm) did not experience full glottal closure, vibrated symmetrically anteriorly-posteriorly (Figure 4.5), but yielded non-life-like vibratory motion. Since the cover layer was so thin, the body layer vibrated more than it would otherwise. This model did not demonstrate visible convergent-divergent motion and did not have a typical wave-like motion. Some vertical displacement is observed in Figure 4.5b. The left fold has a larger amplitude than the right (Figure 4.5c), but this is attributed to inconsistencies between models.

The 1.05 mm models vibrated symmetrically anterior-posteriorly and medially-laterally (Figure 4.6c). The gaps in the curves in Figure 4.6c were caused by the MATLAB program

“losing” the edges when the glottal gap becomes too small or during brief glottal closure (although it is important to note that the closure was not necessarily complete). This is seen in several of the subsequent edge position vs. time graphs. Evidence of a small amount of convergent-divergent-like motion can be seen in Figure 4.6b along with more vertical displacement than what was seen in Figure 4.5b.

The cover layer played a more significant role in governing the vibratory characteristics of the thicker cover layer models than the body layer. The 3.15 mm cover layer models vibrated symmetrically, as can be seen in Figure 4.7c. The amplitude was much larger than any of the previous models. The amplitude was largest in the center of the folds (along the dotted line, Figure 4.7a). Since the MATLAB program tracked the edges of the fold from the glottal area, the wave forms in Figure 4.7c only corresponded to the points on the fold that were closest to the midsagittal plane, or in other words, the points on the vocal folds that were closest to the solid red line shown in Figure 4.7a. With the large convergent-divergent amplitude, this point was not necessarily on the top (superior) margin of the vocal fold. This applies to Figure 4.8c as well. A large amount of vertical displacement can be observed in Figure 4.7c.

As with the 3.15 mm model, the 3.7 mm cover layer model vibrated nearly symmetrically in both the anterior-posterior and left-right directions. The left fold does appear to have had a somewhat larger amplitude than the right fold (Figure 4.8c). Although the model did not reach full glottal closure, it did exhibit a degree of glottal closure (see Figure 4.8a). The 3.7 mm model had the largest vertical displacement of all of the models in this study. Figure 4.8b shows the large amount of convergent-divergent motion, but also the unrealistic oscillating motion caused by such a thick cover layer. This unrealistic oscillation is made evident by a large glottal area,

and large vertical displacement. *In vivo*, there is no vertical displacement and a much smaller glottal area.

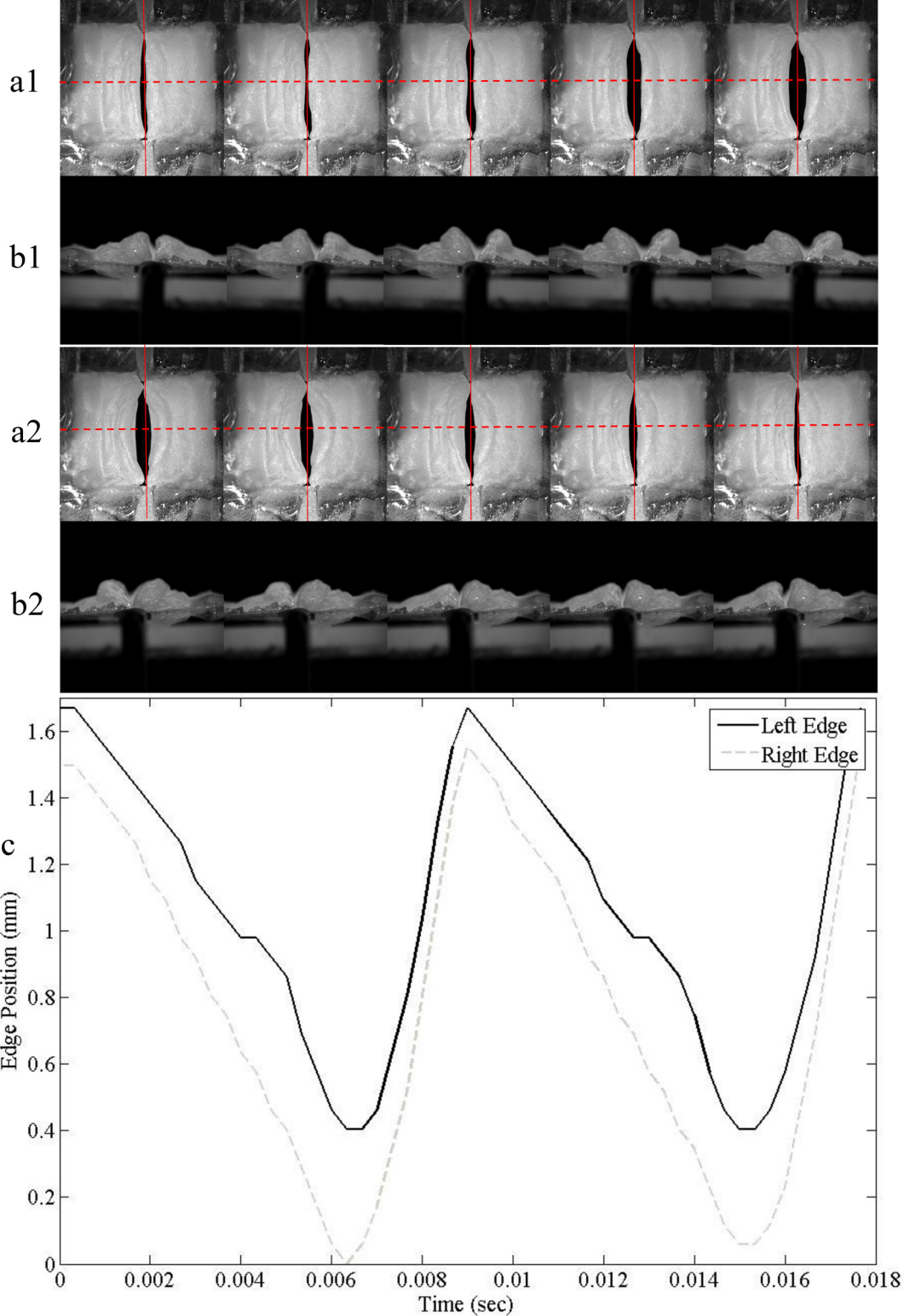


Figure 4.4: Standard (2.1 mm) cover layer at 110% onset pressure. Time between frames: 1 msec. a) Superior view high speed images. b) Side view high speed images. c) Edge position tracking. Each frame in rows a1 and a2 corresponds in time to the frame below in rows b1 and b2, respectively. Rows a2 and b2 are continuations of rows a1 and b1, respectively.

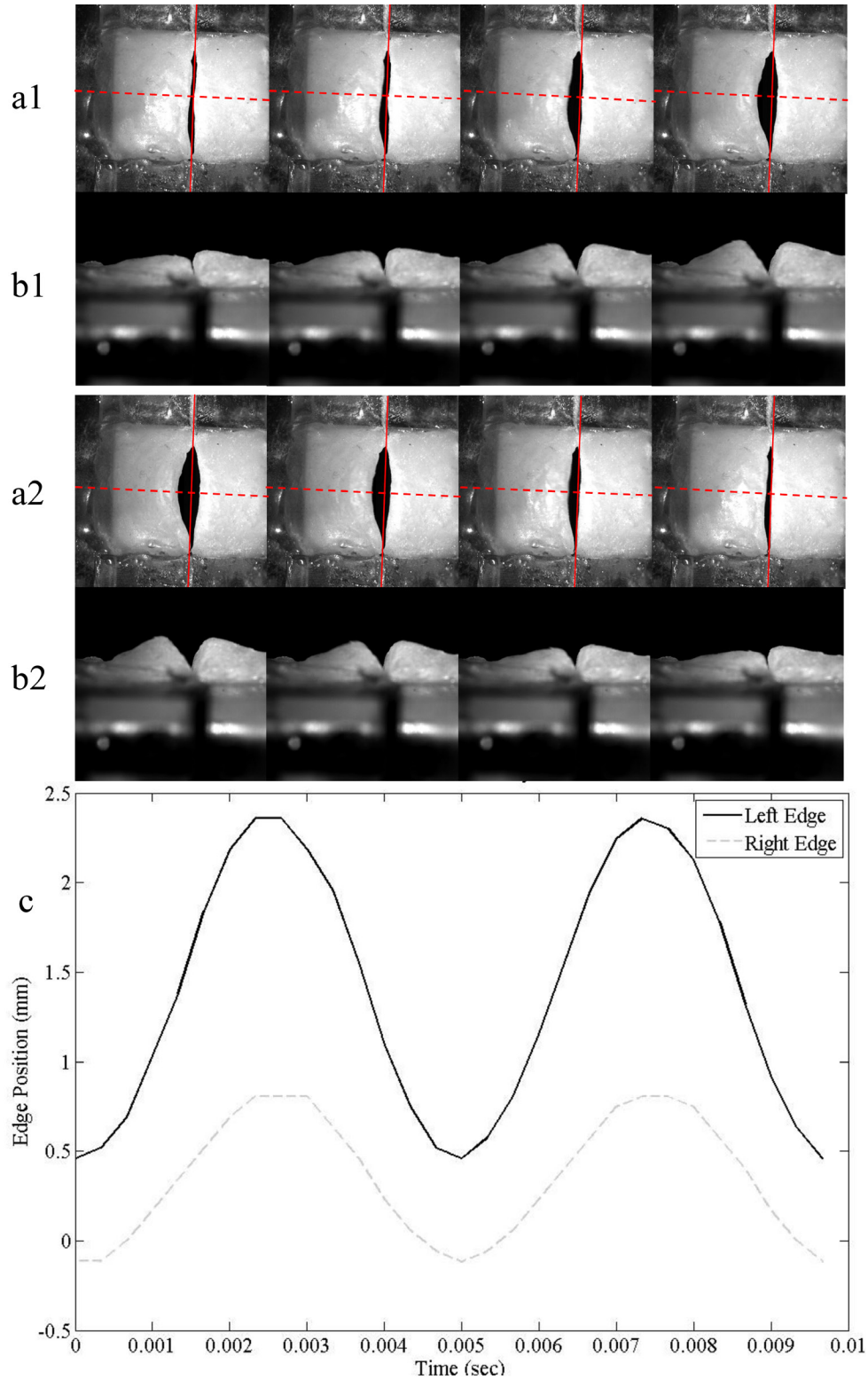


Figure 4.5: Thinnest (0.5 mm) cover layer model at 110% onset pressure. Time between frames: 0.667 msec. a) Superior view high speed images. b) Side view high speed images. c) Edge position tracking. Each frame in rows a1 and a2 corresponds in time to the frame below in rows b1 and b2, respectively. Rows a2 and b2 are continuations of rows a1 and b1, respectively.

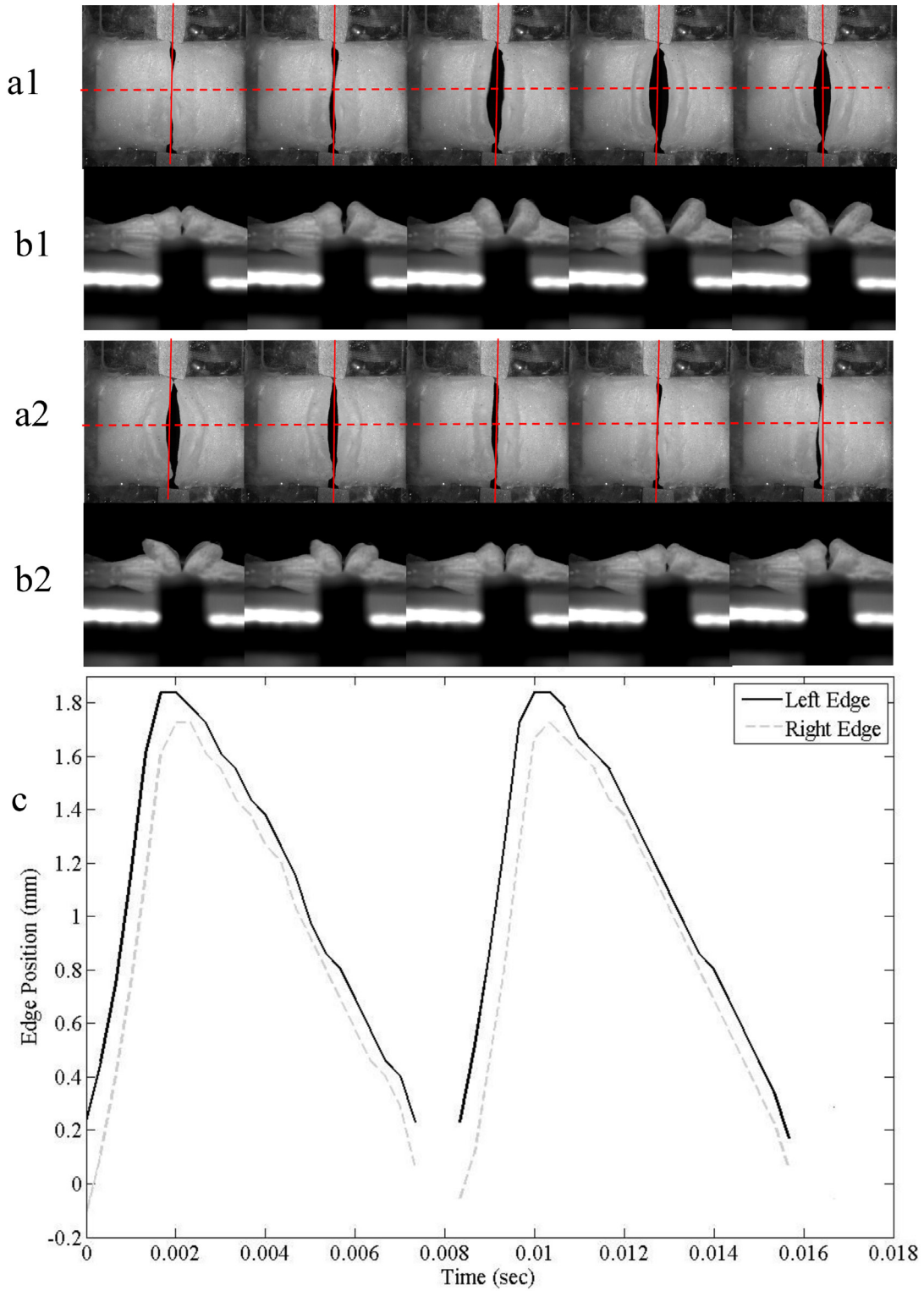


Figure 4.6: 1.05 mm cover layer model at 110% onset pressure. Time between frames: 1 msec. a) Superior view high speed images. b) Side view high speed images. c) Edge position tracking. Each frame in rows a1 and a2 corresponds in time to the frame below in rows b1 and b2, respectively. Rows a2 and b2 are continuations of rows a1 and b1, respectively.

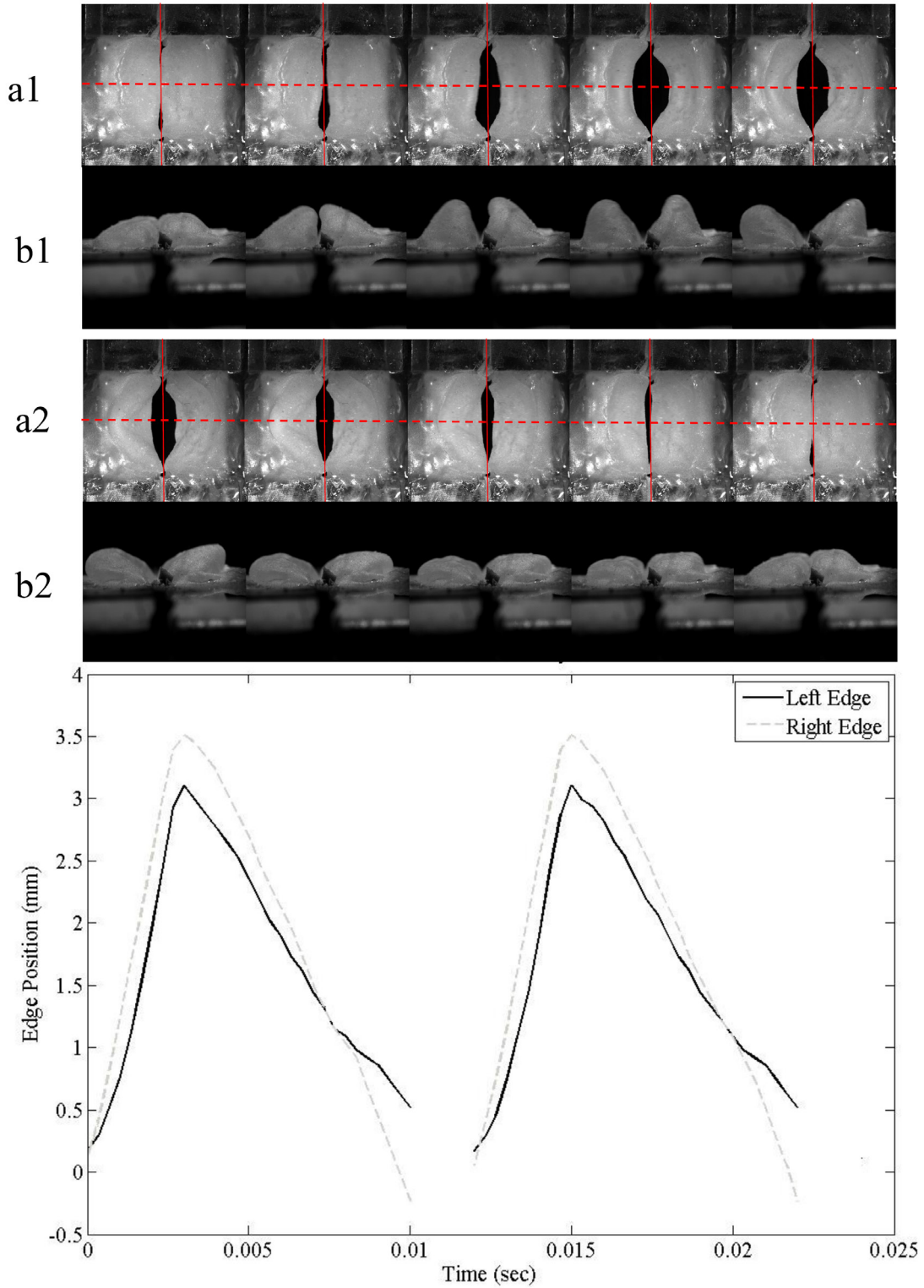


Figure 4.7: 3.15 mm cover layer model at 110% onset pressure. Time between frames: 1.33 msec. a) Superior view high speed images. b) Side view high speed images. c) Edge position tracking. Each frame in rows a1 and a2 corresponds in time to the frame below in rows b1 and b2, respectively. Rows a2 and b2 are continuations of rows a1 and b1, respectively.

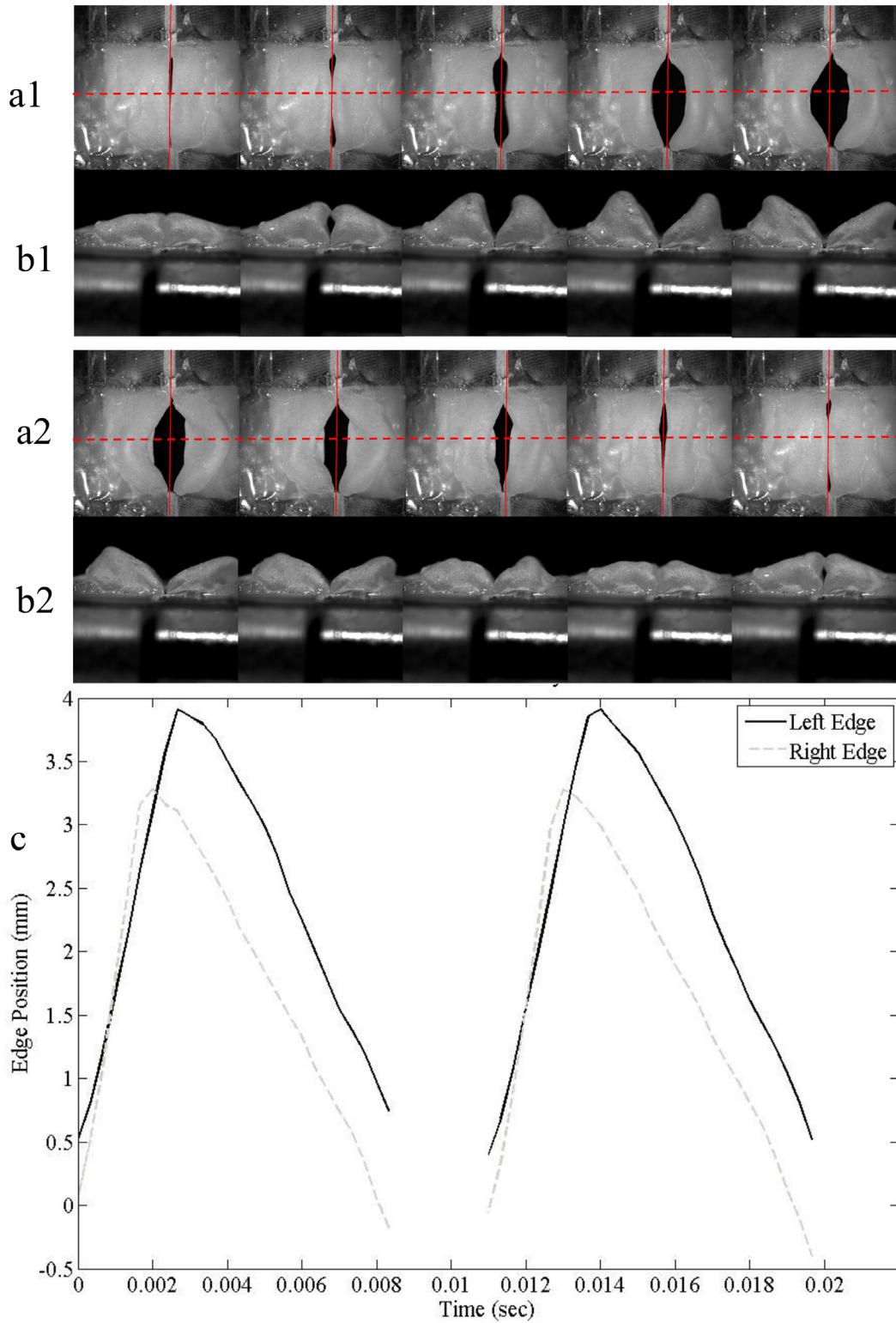


Figure 4.8: 3.7 mm cover layer model at 110% onset pressure. Time between frames: 1.33 msec. a) Superior view high speed images. b) Side view high speed images. c) Edge position tracking. Each frame in rows a1 and a2 corresponds in time to the frame below in rows b1 and b2, respectively. Rows a2 and b2 are continuations of rows a1 and b1, respectively.

For the asymmetric cases, the edge tracking was performed along 3 lines, shown in red in Figures 4.9a and 4.10a. These planes were 1/3, 1/2, and 2/3 of the distance in the anterior-posterior direction. The anterior region (which had the smallest cover layer) experienced the smallest amplitude. The amplitude increased towards the posterior region (except in the immediate vicinity of the posterior boundary). An anterior-posterior zipper-like motion can be observed in Figure 4.9a and in the phases of the displacement vs. time curves in Figure 4.9c.

The same anterior-posterior zipper-like motion can be seen in the 1.05-3.15 mm asymmetric models. Amplitude and phase differences between the left and right folds can be seen (Figure 4.10c).

4.3.5 Model Consistency

With the exception of some outliers, the variations between models of the same type (assumed to be identical models) were small. For example, the average onset pressure for the 1.05 mm symmetric cover layer model was 1.64 kPa with a standard deviation of 0.35 kPa. As can be observed with the error bars in Figure 4.3, the error found between identical models was typically less than the difference observed between different types of models. The model with the largest variation in vibration metrics between identical models was the 0.5 mm cover layer models. Since the cover layer was so thin, it was difficult to fabricate consistent models, even with the new fabrication process. In four of the cases (2.1 mm, 3.7 mm, both asymmetric cases), one of the models behaved much different than the other two identical models. In that circumstance, the model was treated as an outlier and not analyzed in the presented data.

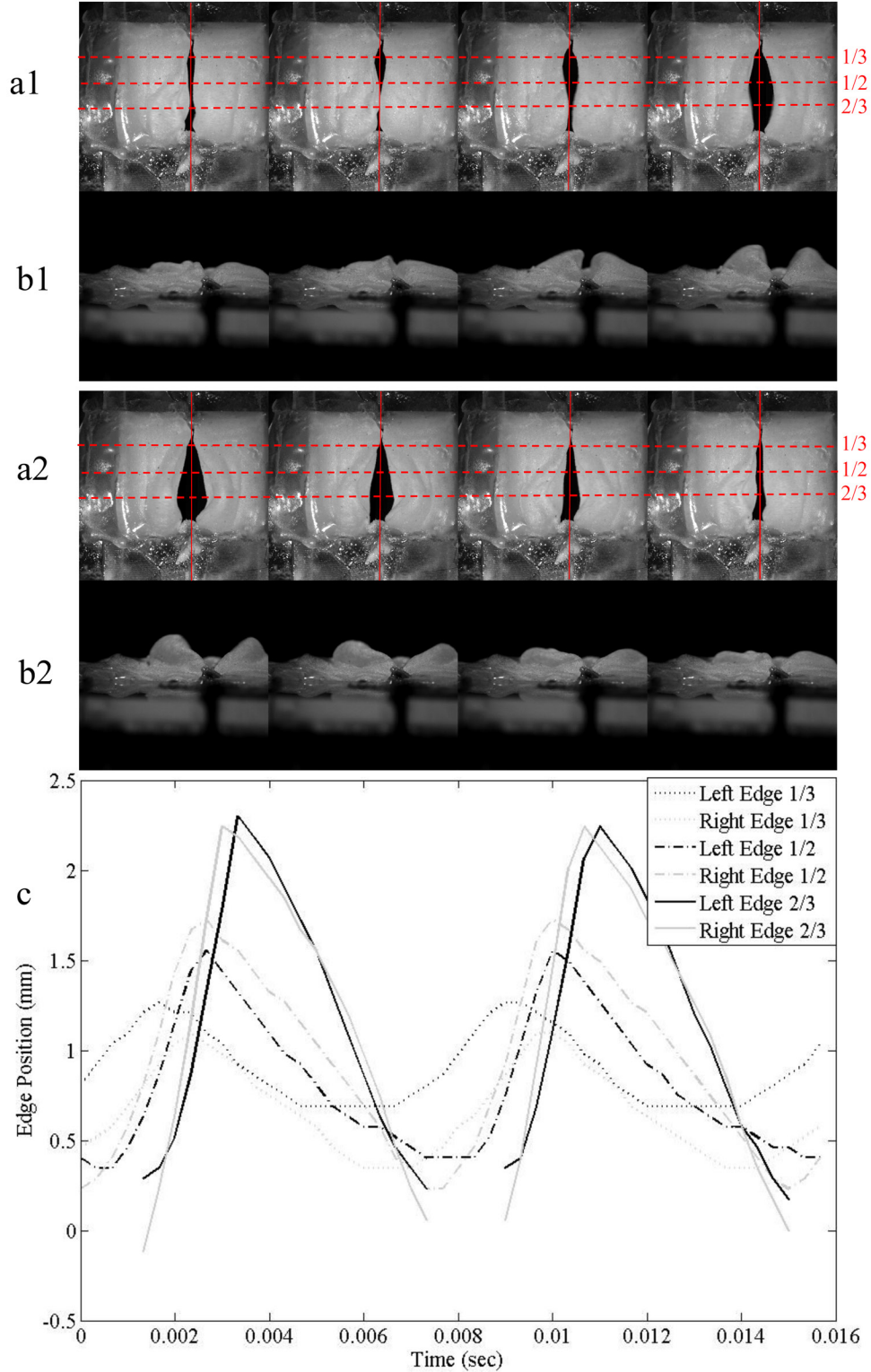


Figure 4.9: Asymmetry case 1 (0.5-3.7 mm) cover layer at 110% onset pressure. Time between frames: 1.33 msec. a) Superior view high speed images. b) Side view high speed images. c) Edge position tracking. Each frame in rows a1 and a2 corresponds in time to the frame below in rows b1 and b2, respectively. Rows a2 and b2 are continuations of rows a1 and b1, respectively.

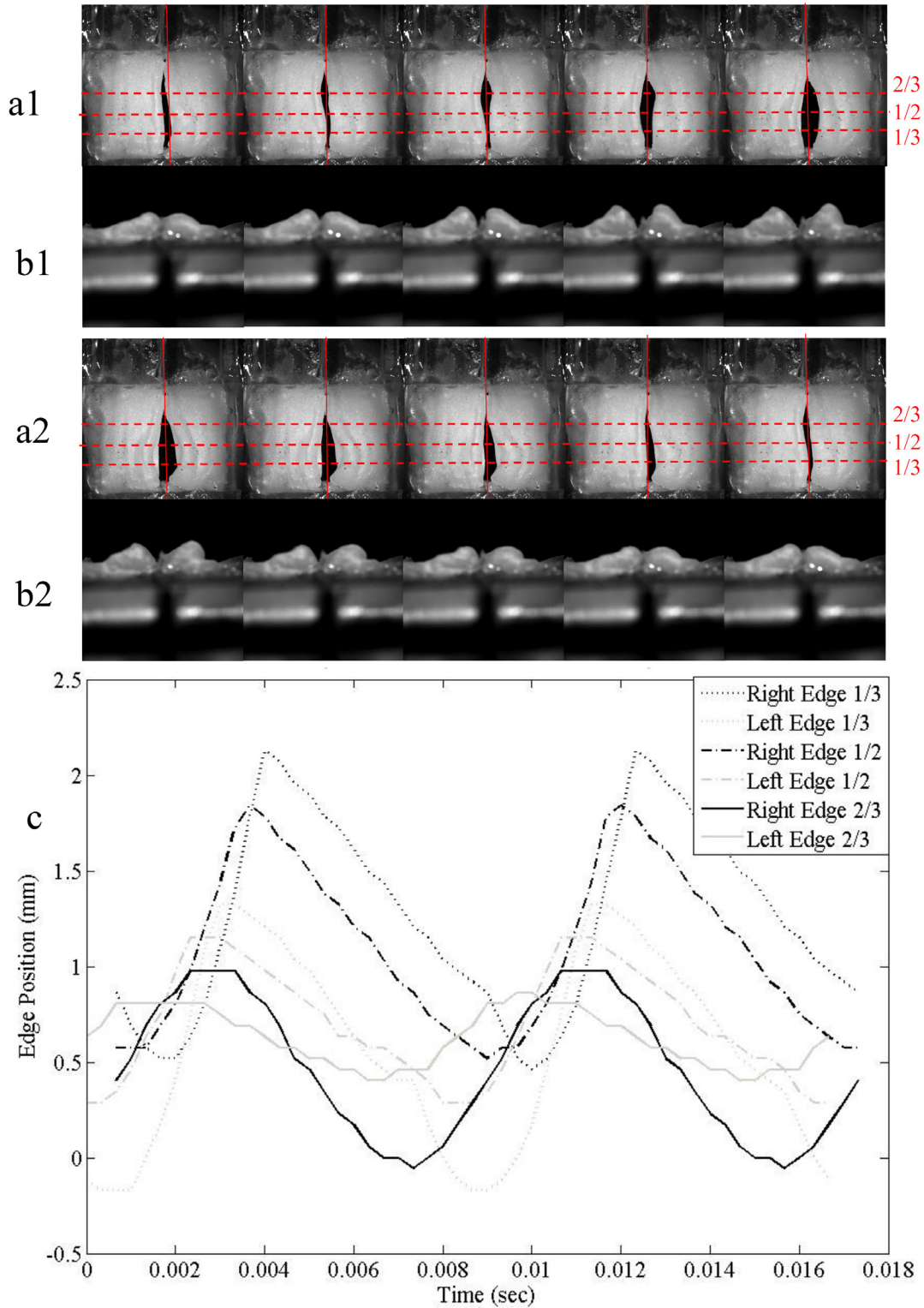


Figure 4.10: Asymmetry case 2: 1.05-3.15 mm cover layer models at 110% onset pressure. Time between frames: 1.33 msec. a) Superior view high speed images. b) Side view high speed images. c) Edge position tracking. Each frame in rows a1 and a2 corresponds in time to the frame below in rows b1 and b2, respectively. Rows a2 and b2 are continuations of rows a1 and b1, respectively.

4.4 Conclusion

Cover layer geometry was varied to explore the effect of cover layer thickness and anterior-posterior geometry asymmetry on vocal fold motion. Cover layer differences had a large effect on model motion and vibration measures. The current standard cover layer thickness (2.1 mm) appears to be close to ideal for the given geometry and layer stiffness distribution. It was seen that inconsistencies between sides of the models can cause left-right amplitude differences. Layer geometry clearly plays a significant role in governing model vibration. The modeling process described in Chapter 3 and used here could be used to study further geometric variations that have not been previously widely investigated.

Asymmetry in this study caused increased pressure and flow rates required for vibration to commence. If human vocal folds were to behave in the same way, it could lead to labored speech, requiring greater lung pressure and air flow, and the voice may have a breathy quality.

5 CONCLUSIONS AND RECOMMENDATIONS

Voice production is a complex phenomenon that is difficult to replicate outside of the body. Vocal fold vibration is essential to characterize in order to understand and treat voice disorders. In order to improve the quality of life of those suffering from voice disorders, more research and better treatments are required. Synthetic vocal fold modeling is an essential part of this research.

This thesis is focused on synthetic vocal fold model fabrication and vibratory response. Left-right and anterior-posterior asymmetries were investigated using two different models. A new MRI-base model was developed and used to investigate left-right asymmetry (Chapter 2). A new fabrication process was developed that opens many doors in vocal fold synthetic modeling research (Chapter 3). This new process was used to study anterior-posterior geometry variation, an area previously under-explored (Chapter 4). As a whole, this thesis contributes to the overall knowledge about and development of synthetic vocal fold models.

5.1 Chapter 2: Left-Right Asymmetric Stiffness in an MRI-Based Geometry

A modified MRI-based model was developed that features realistic geometry that is fully adducted (i.e., there was no bowing, as had been seen in a prior MRI-based model). Left-right body and cover layer stiffness asymmetries were prescribed to investigate the effect of asymmetry in each layer on model motion.

This new model was effective in displaying some vibration characteristics observed in human vocal folds. These include anterior-posterior zipper-like motion, and phonation pressures, flow rates, and frequencies within physiological ranges for an adult male. Anterior-posterior zipper-like motion was exhibited by all of the models, leading to the conclusion that the zipper-like motion was a product of geometry rather than asymmetry. Frequency, flow rate, and pressure did not appear to be significantly influenced by the degree of left-right asymmetry. In the asymmetric cases, a phase shift was present in which the softer side led the stiffer side. The amplitude of the more flexible side was greater than that of the stiffer side.

5.1.1 Future Work

Recommended future work includes flow visualization using the new model, tracking the medial surface vibratory characteristics, and further investigation of the zipper-like motion. It would be beneficial to compare flow characteristics (e.g., using flow visualization and/or particle image velocimetry, PIV) of the new MRI model to those of a simplified model. This would lead to better understanding of the relationship between geometry and air flow. Also, PIV would be useful in understanding the effect that left-right asymmetry has on the flow. Since the model produced such a pronounced convergent-divergent and superior motion, further investigation into the medial surface characteristics with these more realistic model geometries would be useful. Although an anterior-posterior wave or zipper-like motion can be observed *in vivo*, it is rarely seen in models. As stated in Chapter 4, the author theorizes that the zipper-like motion is due to geometry variation in the anterior-posterior direction. Further investigation would be needed to verify this hypothesis. Modeling anisotropy via anterior-posterior fibers could lead to more realistic vibratory characteristics and full glottal closure.

5.2 Chapter 3: Expendable Mold Fabrication Process

The new model fabrication process described in Chapter 3 allows for more flexibility in model development than the old fabrication process. Developing models with geometric variations is quicker and more inexpensive using the new process, allowing researchers to vary geometry to better understand the effects that certain geometric characteristics have on vibration. Alignment problems are nearly eliminated from the process. Since release agent is no longer needed, hybrid models of biological and synthetic materials are possible. It is anticipated that this will allow researchers to investigate the effect of vibration on vocal fold cells. The effect of external factors, such as improper cell nutrition or mechanical loading, could be investigated using these hybrid models.

5.2.1 Future Work

An optimized model geometry that more closely mimics vocal fold vibration might be developed with an iterative investigation into geometry via this new fabrication process. Before this new process was developed, a 3D printer prototype was designed and built as a potentially easier way to fabricate models. Due to design complications, this idea was abandoned and the milling process described in Chapter 3 was pursued. One of the largest difficulties in developing the 3D printer was related to the materials. The pre-cured silicone was not adequately viscous for printing. Also, the printer was unable to reach the required resolution. A 3D printer that could print the soft materials for these models would provide researchers with even more freedom in geometry variation than the current process. Release agent would not be required in a 3D printing process and alignment could be even more precise than in the milled models. A 3D printing process for making synthetic vocal fold models therefore warrants further investigation.

5.3 Chapter 4: Cover Layer Thickness Variation and Asymmetry

The process described in Chapter 3 was used to develop models in which the cover layer thickness in simplified vocal fold models was varied. The role that the cover layer and body layer each play in model vibration was studied. Anterior-posterior cover layer geometry was also varied. There were distinct difference in vibration metrics due to the anterior-posterior asymmetry. Increased flow rate and pressure were required for vibration in the asymmetric cases. Larger cover layer thickness was directly correlated to amplitude and inversely related to frequency.

5.3.1 Future Work

Further investigations in geometry variation is warranted. PIV or another type of flow visualization could be used to understand the effects that cover layer thickness and asymmetry have on air flow characteristics. With the new fabrication process, geometry abnormalities, such as polyps or nodules, could be investigated. Fibers have been introduced in other models (Murray et al., 2014; Xuan and Zhang, 2014), and further investigation into this (e.g., fiber placement and number of fibers) would be a good next step in improving synthetic models. Ultimately further work in this area is hoped to lead to an optimal model geometry that more accurately models the motion and vibration metrics of human vocal folds. An iterative process utilizing the methods in Chapter 3 could lead to the development of such a model.

REFERENCES

Alipour, F., Berry, D. A., and Titze, I. R. (2000). "A finite-element model of vocal-fold vibration." *Journal of the Acoustical Society of America* **108**:3003-3012.

Baken, R. J. (1999). *Clinical measurement of speech and voice*. San Diego, Singular Pub. Group.

Bhattacharya, P. and Siegmund, T. (2012). "A canonical biomechanical vocal fold model." *Journal of Voice* **26**(5):535-547.

Chan, R. W., Titze, I. R., and Titze, M. R. (1997). "Further studies of phonation threshold pressure in a physical model of the vocal fold mucosa." *Journal of the Acoustical Society of America* **101**(6):3722-3727.

Cook, D. D., Nauman, E., and Mongeau, L. (2009). "Ranking vocal fold model parameters by their influence of model frequencies." *Journal of the Acoustical Society of America* **126**(4):2002-2010.

Murray, P. R. and Thomson, S. L. (2011). "Synthetic, multi-layer, self-oscillating vocal fold model fabrication." *Journal of Visualized Experiments* **58**:e3498.

Murray, P. R. and Thomson, S. L. (2012). "Vibratory responses of synthetic, self-oscillating vocal fold models." *Journal of the Acoustical Society of America* **132**(5):3428-3438.

Murray, P. R., Thomson, S. L., and Smith, M. E. (2014). "A synthetic, self-oscillating vocal fold model platform for studying augmentation injection." *Journal of Voice* **28**(2):133-143.

Pickup, B. A. and Thomson, S. L. (2009). "Influence of asymmetric stiffness on the structural and aerodynamic response of synthetic vocal fold models." *Journal of Biomechanics* **42**(14):2219-2225.

Pickup, B. A. and Thomson, S. L. (2010). "Flow-induced vibratory response of idealized versus magnetic resonance imaging based synthetic vocal fold models." *Journal of the Acoustical Society of America* **128**(3):EL124-EL129.

Pickup, B. A. and Thomson, S. L. (2011). "Identification of geometric parameters influencing the flow-induced vibration of a two-layer self-oscillating computational vocal fold model." *Journal of the Acoustical Society of America* **129**(4):2121-2132.

Scherer, R. C., Shinwari, D., De Witt, K. J., Zhang, C., Kucinski, B. R., and Afjeh, A. (2001). "Intraglottal pressure profiles for a symmetric and oblique glottis with a divergence angle of 10 degrees." *Journal of the Acoustical Society of America* **109**(4):1616-1630.

Shaw, S. M., Thomson, S. L., Dromey, C., and Smith, S. (2012). Frequency response of synthetic vocal fold models with linear and nonlinear material properties. *Journal of Speech, Language, and Hearing Research*. **55**:1395-1406.

Smith, S. and Thomson, S. (2012). "Effect of inferior surface angle on the self-oscillation of a computational vocal fold model." *Journal of the Acoustical Society of America* **131**(5):4062-4075.

Xuan, Y. and Zhang, Z. (2014). "Influence of embedded fibers and an epithelium layer on glottal closure pattern in a physical vocal fold model." *Journal of Speech, Language and Hearing Research* **57**(2):416-425.

Xue, Q., Mittal, R., Zheng, X., and Bielamowicz, S. (2010). "A computational study of the effect of vocal-fold asymmetry on phonation." *Journal of the Acoustical Society of America* **128**(2):818-827.

Zhang, Z. (2010). "Vibration in a self-oscillating vocal fold model with left-right asymmetry in body-layer stiffness." *Journal of the Acoustical Society of America* **128**:EL279-EL285.

Zhang, Z., Kreiman, J., Gerratt, B. R., and Garellek, M. (2013). "Acoustic and perceptual effects of changes in body layer stiffness in symmetric and asymmetric vocal fold models." *Journal of the Acoustical Society of America* **133**(1):453-462.

Zhang, Z. Y. and Luu, T. H. (2012). "Asymmetric vibration in a two-layer vocal fold model with left-right stiffness asymmetry: Experiment and simulation." *Journal of the Acoustical Society of America* **132**(3):1626-1635.

Zrunek, M., Happak, W., Hermann, M., and Streinzer, W. (1988). "Comparative anatomy of human and sheep laryngeal skeleton." *Acta Oto-laryngologica* **105**: 155-162.

APPENDIX A. MRI-BASED MODEL DESIGN DETAILS

The following is an overview of how the MRI-based model geometry was defined. The purple geometry is the raw MRI data and the gray geometry is the modified geometry.

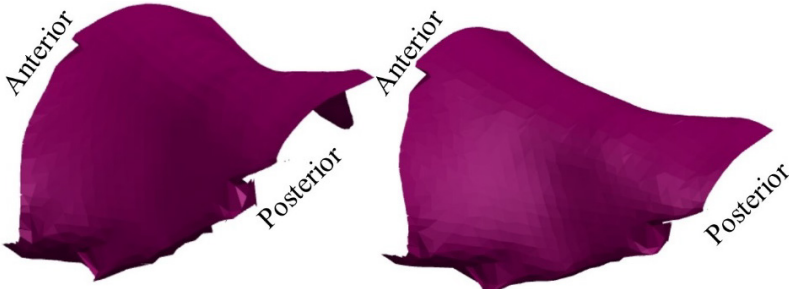


Figure A.1: Vocal fold surface derived from raw MRI data.

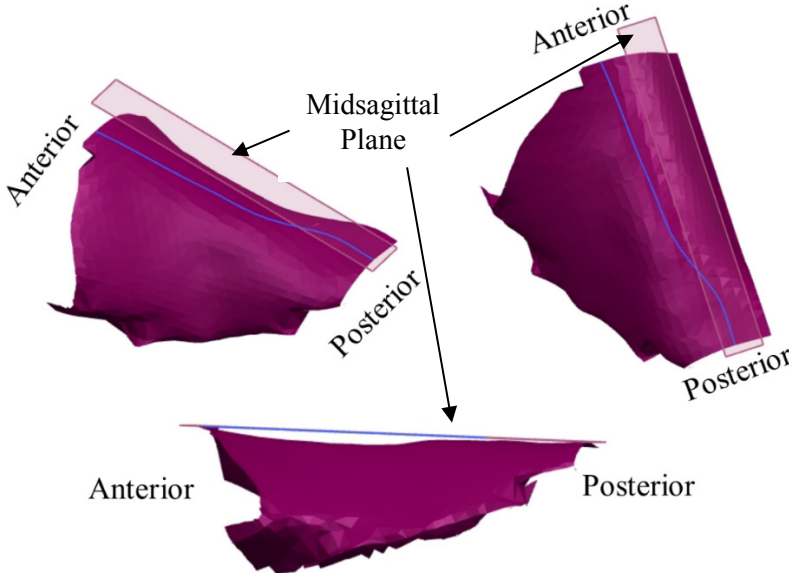


Figure A.2: The highest points along the medial surface were selected and projected onto the midsagittal plane. These points formed a spline which served as the guide curve.

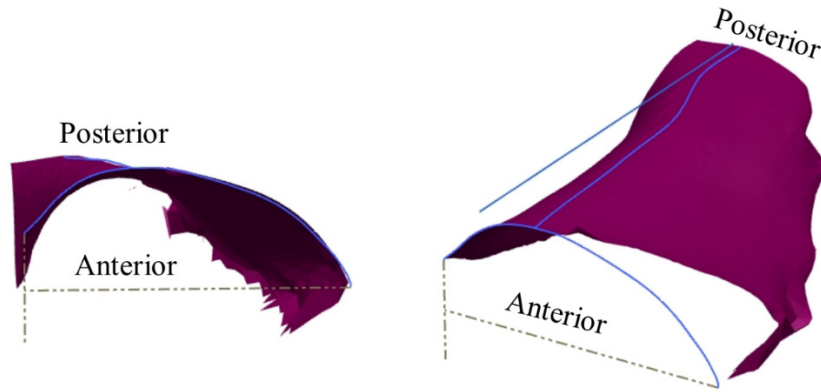


Figure A.3: Points along the anterior surface were projected onto a coronal plane at the anterior-most surface.

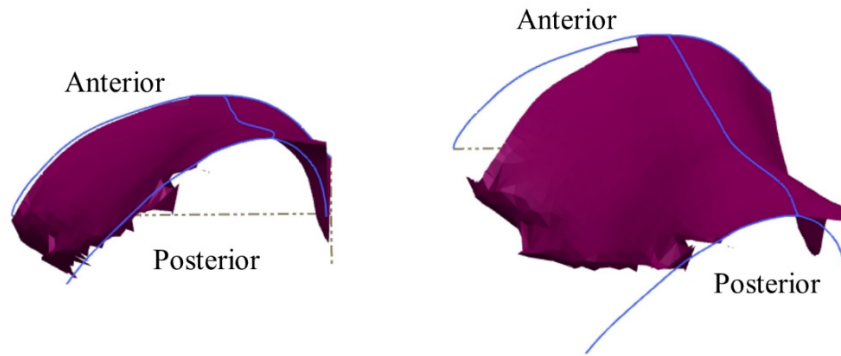


Figure A.4: Points along the posterior surface were projected onto a coronal plane at the posterior-most surface.

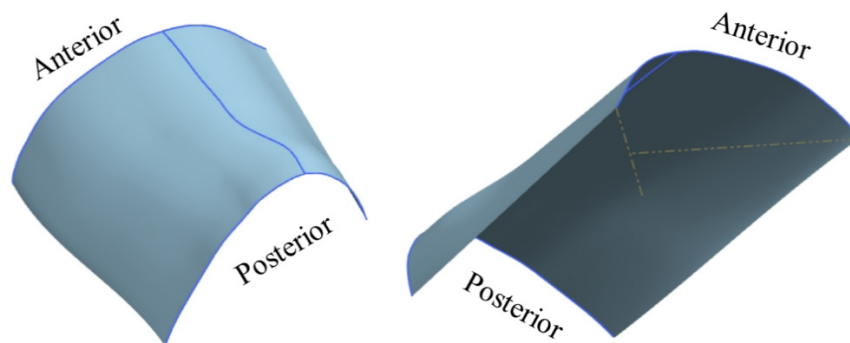


Figure A.5: The anterior and posterior curves were lofted along the guide curve, forming a surface.

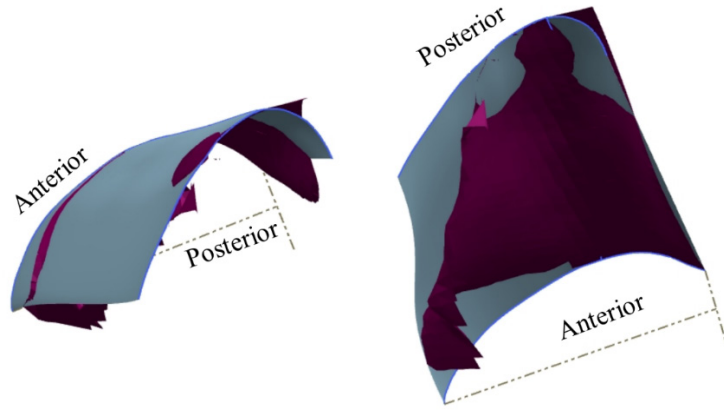


Figure A.6: This surface matches well with the raw MRI data.

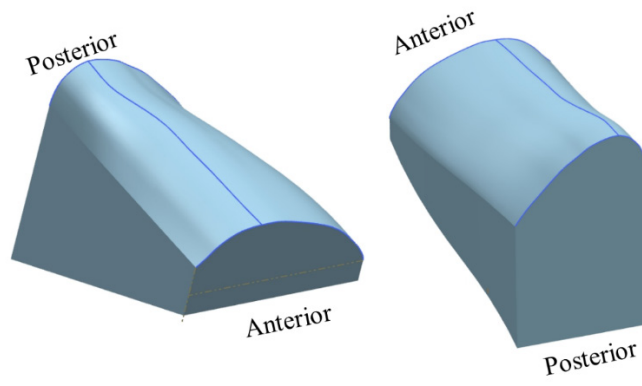


Figure A.7: Finished MRI-based model.

APPENDIX B. MATLAB CODE FOR EDGE TRACKING

This code was written by Preston Murray and altered by Shelby Ward.

```
% File to track position of point in 3D space over time. Uses
% correlation-based tracking algorithm combined with DLT.
% Altered by Preston Murray to incorporate multiple points
% opengl software

clc
close all
clear all

%% User Defined inputs
% Define window size (must be even number) for t and t+dt as well as the
% left to right correlation

MT = 8;
NT = 8;
MLR = 16;
NLR = 16;

% If manual points are desired, please enter how many points.
numpoints = 1;

% Enter the number of frames
frames = 40;% I don't know what is supposed to go here.

%% Image load and Calibration
% Load image. Note that A is in spatial coordinates, with i=1,j=1 at the
% top left of the image. A(y,x) is the appropriate way to reference x,y
% position since A data is stored as A(row,column), where row = x and
% column = y data.

pathR = 'E:\Shelby\ICVPB 2014\ICVPB 2014\Medial surface\t1_1.05
t2_3.15_modell_110_C002H001S0001\';
pathL = 'E:\Shelby\ICVPB 2014\ICVPB 2014\Medial surface\t1_1.05
t2_3.15_modell_110_C001H001S0001\';
fileR = 't1_1.05 t2_3.15_modell_110_C002H001S0001000001.tif';%is this all of
the calibrating frames?
fileL = 't1_1.05 t2_3.15_modell_110_C001H001S0001000001.tif';
```

```

% Load the images
imageR = imadjust(imread([pathR fileR]));
imageL = imadjust(imread([pathL fileL]));

% Use the following if L & R and calibration points have already been
% found & stored
% calframes = 14;
% [L,R,aveerror] = GridFinder(calframes, 'F:\Shelby\ICVPB 2014\ICVPB
2014\Medial surface\_Calibration\');
%
% close all
% save LR2.mat L R -double

load LR2.mat
% Choose point to track. Click on same point (approximately) in both left
% and right views. The FFT method will be used to fine-tune the right view
% point.

thing1 = 'Manual Mode';
thing2 = ['Please choose ', num2str(numpoints), ' sets of points'];
title(thing1);
xlabel(thing2);
imshow(imageL)
set(gcf, 'position', [0 150 560 420])

for i = 1:numpoints
    [uL0(i), vL0(i)] = ginput(1);
    hold on
    plot(uL0(i), vL0(i), 'g.')
end
hold off

% close(fgure(1))
figure
imshow(imageR)
set(gcf, 'position', [460 150 560 420])
for i = 1:numpoints
    [uR0(i), vR0(i)] = ginput(1);
    hold on
    plot(uR0(i), vR0(i), 'g.')
end
hold off

%% Adjust the points from left to right
% Call function to interrogate window using FFT method. This is where the
% right view point will be fine-tuned (that is, the window in the right
% view that matches the window in the left view will be found).

for i=1:numpoints
    [xd, yd] =
LRInterrogate(MLR, NLR, uL0(i), vL0(i), uR0(i), vR0(i), imageL, imageR);
    xdtemp(i) = xd;
    ydtemp(i) = yd;
end

```

```

% Adjust points based on interrogation results
uL = uL0;
vL = vL0;
uR = uR0 + xdtemp;
vR = vR0 + ydtemp;

% Display adjusted point location
figure(1)
imshow(imageL)
set(gcf, 'position', [0 150 560 420])
hold on
plot(uL, vL, '.g')
figure(2)
imshow(imageR)
set(gcf, 'position', [460 150 560 420])
hold on
plot(uR, vR, '.r.')

% hold off
% Start storage of uL, vL, uR, vR point locations
UL = uL;
VL = vL;
UR = uR;
VR = vR;

%% Loop through images to track point(s) over time
% Changing path
pathL1= 'E:\Shelby\ICVPB 2014\ICVPB 2014\Medial surface\t1_1.05
t2_3.15_model1_110_C001H001S0001\';
pathR1= 'E:\Shelby\ICVPB 2014\ICVPB 2014\Medial surface\t1_1.05
t2_3.15_model1_110_C002H001S0001\';
for i = 1:frames-1
    % Load images at time=t and time=t+dt
    imageL1 = [pathL1 't1_1.05 t2_3.15_model1_110_C001H001S0001'
num2str(i, '%0.6i') '.tif'];
    imageL2 = [pathL1 't1_1.05 t2_3.15_model1_110_C001H001S0001'
num2str(i+1, '%0.6i') '.tif'];
    imageR1 = [pathR1 't1_1.05 t2_3.15_model1_110_C002H001S0001'
num2str(i, '%0.6i') '.tif'];
    imageR2 = [pathR1 't1_1.05 t2_3.15_model1_110_C002H001S0001'
num2str(i+1, '%0.6i') '.tif'];
    ALa = imadjust(imread(imageL1), [0;.35], [0;1]);
    ALb = imadjust(imread(imageL2), [0;.35], [0;1]);
    ARa = imadjust(imread(imageR1), [0;.65], [0;1]);
    ARb = imadjust(imread(imageR2), [0;.65], [0;1]);

    % Initialize point locations. Here, instead of comparing left & right
    % views, we're looking at the left view at time=t and comparing it to
    % the same left view at time=t+dt.
    uL0 = UL;
    vL0 = VL;
    uLdt = UL;
    vLdt = VL;

    % Track region in left view from time=t to time=t+dt
    for j = 1:numpoints

```

```

        [xd,yd] =
TInterrogate(MT,NT,uL0(:,j,i),vL0(:,j,i),uLdt(:,j,i),vLdt(:,j,i),ALa,ALb);
        xdltemp(:,j,i) = xd;
        ydltemp(:,j,i) = yd;
    end

    % Adjust points based on interrogation results
    uL(:, :, i) = uL0(:, :, i);
    vL(:, :, i) = vL0(:, :, i);
    uLdt(:, :, i) = uLdt(:, :, i) + xdltemp(:, :, i);
    vLdt(:, :, i) = vLdt(:, :, i) + ydltemp(:, :, i);

    % Compare right view point at time=t to time=t+dt.
    uR0(:, :, i) = UR(:, :, i);
    vR0(:, :, i) = VR(:, :, i);
    uRdt(:, :, i) = UR(:, :, i);
    vRdt(:, :, i) = VR(:, :, i);

    % Track region in right view from time=t to time=t+dt
    for j = 1:numpoints
        [xd,yd] =
TInterrogate(MT,NT,uR0(:,j,i),vR0(:,j,i),uRdt(:,j,i),vRdt(:,j,i),ARa,ARb);
        xdrtemp(:,j,i) = xd;
        ydrtemp(:,j,i) = yd;
    end

    % Adjust points based on interrogation results
    uR(:, :, i) = uR0(:, :, i);
    vR(:, :, i) = vR0(:, :, i);
    uRdt(:, :, i) = uRdt(:, :, i) + xdrtemp(:, :, i);
    vRdt(:, :, i) = vRdt(:, :, i) + ydrtemp(:, :, i);

    % Match point in right view at time=t+dt to point in left view at
    % same time step.
    for j = 1:numpoints
        [xd,yd] =
LRInterrogate(MLR,NLR,uLdt(:,j,i),vLdt(:,j,i),uRdt(:,j,i),vRdt(:,j,i),ALb,ARb
);
        xdtemp(j) = xd;
        ydtemp(j) = yd;
    end

    % Adjust points based on interrogation results
    uLdt(:, :, i) = uLdt(:, :, i);
    vLdt(:, :, i) = vLdt(:, :, i);
    uRdt(:, :, i) = uRdt(:, :, i) + xdtemp;
    vRdt(:, :, i) = vRdt(:, :, i) + ydtemp;

    % Store point locations
    UL(:, :, i+1) = uLdt(:, :, i);
    VL(:, :, i+1) = vLdt(:, :, i);
    UR(:, :, i+1) = uRdt(:, :, i);
    VR(:, :, i+1) = vRdt(:, :, i);

    % Display adjusted point location

```

```

figure(1)
imshow(ALb);
hold on
for j = 1:numpoints
    plot(UL(:,j,i),VL(:,j,i),'g.', UL(:,j,i+1),VL(:,j,i+1),'r.')
end
hold off

figure(2)
imshow(ARb)
hold on
for j = 1:numpoints
    plot(UR(:,j,i),VR(:,j,i),'g.',UR(:,j,i+1),VR(:,j,i+1),'r.')
end
hold off

% Create a movie from the plot frame
% mov1(i) = getframe(1);
% pause
end
%% Use DLT function to evaluate real-world position of selected points
for i = 1:frames
    for j = 1:numpoints
        X(j,:,i) = DLTApply(UL(:,j,i),VL(:,j,i),UR(:,j,i),VR(:,j,i),L,R);
    end
end

% save X.mat -double

% load X.mat
%% Plots of points and surface
% Plot the trajectories of each point
for i = 1:numpoints

plot3(reshape(X(i,3,:),1,[]),reshape(X(i,2,:),1,[]),reshape(X(i,1,:),1,[]))
    hold on
    %     plot([0 0], [-5 10],'--k')
    %     ylim([-5 10])
    axis equal
end
xlabel('x')
ylabel('y')
zlabel('z')
hold off
%%
% Timeline of surface through one period
len = length(uR0(1,1,:));
toverT = [1 round(.1*len) round(.2*len) round(.3*len) round(.4*len)
round(.5*len) round(.6*len) round(.7*len) round(.9*len) round(.9*len) ];
i = 1;
q = 1;

figure('Position',[1 31 1280 920])
% pause
for j = toverT
    % plot the trajectories

```

```

subplot(1,length(toverT),q)
% set(gca,'position',[.01*(q-1)*9.4 0.9 .09 .09])
plot(reshape(X(:,3,j),1,[]),reshape(X(:,2,j),1,[]),'k','LineWidth',2)
i = i+1;
hold on
q = q+1;
% plot the points on a line in time
for p = 1:numpoints
    plot(reshape(X(p,3,:),1,[]),reshape(X(p,2,:),1,[]),'k')
    % ylabel(lab)
    xlim([-8 0])
    hold on
    plot([0 0],[-6 6],'--k','LineWidth',2)
    axis equal
end
if j > 5
    set(gca, 'YTick', []);
    set(get(gca, 'YLabel'), 'String', '')
end
% set(gca, 'XTick', [])
set(gca, 'TickDir', 'in')
end

```

```

function [L,R,aveerror] = GridFinder(frames, path)
    for i = 1:frames+1
        %% Load and display the image
        % folder1 = [num2str(i-1) '_C1\'];
        % folder2 = [num2str(i-1) '_C2\'];
        imageL = [path num2str(i-1) '_C001H001S0001000001.tif'];% I need to
rename the calibration images
        imageR = [path num2str(i-1) '_C002H001S0001000001.tif'];
        imageR = imread(imageR);
        imageL = imread(imageL);
        % adjust the contrast of the images
        imageR = imadjust(imageR);
        imageL = imadjust(imageL);
        subplot(1,2,2)
        imshow(imageR)
        subplot(1,2,1)
        imshow(imageL)
        %% Theshold the image and convert to binary
        i
        % Make parts of the right image go away
        imageR(1:end,1:150) = 0; % Crop from left to right side of grid
        imageR(1:110,1:end) = 0; % Crop from top to bottom
        imageR(1:end,430:end) = 0; % Crop from right side of grid to right
of image
        imageR(390:end,1:end) = 0; % Crop from the bottom of grid to bottom
        subplot(1,2,2)
        imshow(imageR)
        % Make parts of the left image go away
        imageL(1:100,1:end) = 0; % Crop from top to bottom
        imageL(1:end,1:125) = 0; % Crop from left to right side of grid
    end
end

```

```

        imageL(1:end,390:end) = 0; % Crop from right side of grid to right
        imageL(400:end,1:end) = 0; % Crop from the bottom of grid to bottom
of image
        subplot(1,2,1)
        imshow(imageL)
        % Use graythresh to find the image threshold value
%         levelR = graythresh(imageR);
%         levelL = graythresh(imageL);
        levelR = .2;
        levelL = .2;
        % Change the images to black and white
        bwR = im2bw(imageR,levelR);
        bwL = im2bw(imageL,levelL);
        % Filter the image
        bwR = bwareaopen(~bwR, 20);
        bwL = bwareaopen(~bwL, 20);
        % Show the processed image
        figure
        subplot(1,2,2)
        imshow(bwR)
        subplot(1,2,1)
        imshow(bwL)
        %% Call the CentroidFind mfile to find the centroids
        [centroidR, zeropoint1] = CentroidFind(bwR);
        [centroidL, zeropoint2] = CentroidFind(bwL);
        % Sort the centroids
        centroid = sortcentroid(centroidR, centroidL);
        % Load the centroids and origins into their respective matrices
(x,y,z)
        for j = 1: numel(centroid(:,1))
            for k = 1:2
                centroidgrid(j,k,i) = centroid(j,k);
            end
        end
        % origins(:, :, i) = zeropoint1(:);
        % origin2(:, :, i) = zeropoint2(:);
end
%% Calibrate the L and R Matrices

% Extract the pixel locations for the left and right images
[uR vR uL vL] = dotsort(centroidgrid);

% Load the real life coordinates of the points
realmat= [path 'realmat.xls'];
realmat= importdata(realmat);
% Parse out the coordinates from each picture
x = realmat.realmat(1:600,1);
y = realmat.realmat(1:600,2);
z = realmat.realmat(1:600,3);

% Calculate the L and R matrices
[L,R] = DLTCalib(uL, vL, uR, vR, x, y, z);
%% Determine the error in the system at each point
% Use DLT function to evaluate real-world position of selected points
for i = 1:length(x)
    X(i,:) = DLTApply(uL(i),vL(i),uR(i),vR(i),L,R);

```

```

end

% Determine the error in the calibration system
for i = 1:length(x)
    error(i) = sqrt((x(i)-X(i,1))^2 + (y(i)-X(i,2))^2 + (z(i)-X(i,3))^2);
end

aveerror = mean(error);

%% Plot the results
% Plot the centroids
for j = 1:frames

    % Show image
    imageL = [path num2str(j) '_C001H001S0001000001.tif'];
    imageR = [path num2str(j) '_C002H001S0001000001.tif'];
    imageR = imread(imageR);
    imageL = imread(imageL);

    % adjust the contrast of the images
    imageR = imadjust(imageR);
    imageL = imadjust(imageL);
    figure(j)
    subplot(122)
    imshow(imageR);
    hold on

    % Plot the grid
    for k = 1 : 100
        plot(centroidgrid(k,1,j), centroidgrid(k,2,j), 'bo');
        % mov(k) = getframe;
        % pause
    end

    subplot(121)
    imshow(imageL);
    hold on

    % Plot the grid
    for k = 101 : numel(centroidgrid(:,1))
        plot(centroidgrid(k,1,j), centroidgrid(k,2,j), 'bo');
        % mov(k) = getframe;
        % pause
    end
end
end
end

function [xd,yd] = LRInterrogate(M,N,uA,vA,uB,vB,imageL,imageR)

    uA = round(uA);
    vA = round(vA);
    uB = round(uB);
    vB = round(vB);

```

```

% Define left & right windows (subsets of original image)
Aa = imageL(vA-(N/2-1):vA+N/2, uA-(M/2-1):uA+M/2);
Ab = imageR(vB-(N/2-1):vB+N/2, uB-(M/2-1):uB+M/2);

% Calculate FFT2 of left image window, centered about uL0,vL0

% Recall that image indices are in row,column format, which is y,x
FFTa = fft2(Aa);

% Calculate FFT2 of right image window, centered about uR0,vR0
FFTb = fft2(Ab);

% Use FFT method to compare left & right images
phi = fftshift(iff2(FFTa.*conj(FFTb)));

% Find peak of correlation. This tells us how much the right window needs
% to be adjusted (fine-tuned) based on our original pick.
[npeakint,mpeakint] = find(max(max(phi))==phi);
npeakint = npeakint(1);
mpeakint = mpeakint(1);

% This part is not used, not sure why
xdint = -(mpeakint -(M/2 + 1));
ydint = -(npeakint -(N/2 + 1));

% Conditional statements to move the point away from the
% edges of the interrogation window

if npeakint < 2
    npeakint = 2;
elseif npeakint > N-2
    npeakint = N-2;
end

if mpeakint < 2
    mpeakint = 2;
elseif mpeakint > M-2
    mpeakint = M-2;
end

% Calculate sub-pixel displacement
mstar = (log(phi(npeakint,mpeakint+1)) -log(phi(npeakint,mpeakint-
1)))/(4*log(phi(npeakint,mpeakint)) -2*log(phi(npeakint,mpeakint-1)) -
2*log(phi(npeakint,mpeakint+1)));
nstar = (log(phi(npeakint+1,mpeakint)) -log(phi(npeakint-
1,mpeakint)))/(4*log(phi(npeakint,mpeakint)) -2*log(phi(npeakint-1,mpeakint))
-2*log(phi(npeakint+1,mpeakint)));
mpeak = mpeakint + mstar;
npeak = npeakint + nstar;
xd = -(mpeak -(M/2 + 1));
yd = -(npeak -(N/2 + 1));

% % Display correlation surface and peak location

```

```

% % Display windows
% figure(4)
% set(gcf,'position',[700 35 560 420])
% subplot(221)
% imshow(uint8(Aa))
% xlabel('Left')
% subplot(222)
% subplot(2,2,2)
% imshow(uint8(Ab))
% xlabel('Right')
%
% subplot(223)
% subplot(2,2,3)
% mesh(phi)
% xlabel('m')
% ylabel('n')
% shading interp
% hold on
% plot3(mpeakint,npeakint,max(max(phi)), 'g.')
% plot3(mpeak,npeak,max(max(phi)), 'r.')
%
% hold off
% subplot(224)
% subplot(2,2,4)
% axis square
% pcolor(phi)
% xlabel('m')
% ylabel('n')
% shading interp
% hold on
% plot(mpeakint,npeakint, 'g.',mpeak,npeak, 'r.')
% hold off
% % pause
end

```

```

function [xd,yd] = TInterrogate(M,N,uA,vA,uB,vB,A1,A2)
    uA = round(uA);
    vA = round(vA);
    uB = round(uB);
    vB = round(vB);

    % Define left & right windows (subsets of original image)
    Aa = A1(vA-(N/2-1):vA+N/2, uA-(M/2-1):uA+M/2);
    Ab = A2(vB-(N/2-1):vB+N/2, uB-(M/2-1):uB+M/2);

    % % Display windows
    % figure(2)
    % subplot(121)
    % imshow(uint8(Aa))
    % subplot(122)
    % imshow(uint8(Ab))

```

```

% Calculate FFT2 of left image window, centered about uL0,vL0
% Recall that image indices are in row,column format, which is y,x
FFTa = fft2(Aa);

% Calculate FFT2 of right image window, centered about uR0,vR0
FFTb = fft2(Ab);

% Use FFT method to compare left & right images
phi = fftshift(iff2(FFTa.*conj(FFTb)));

% Find peak of correlation. This tells us how much the right window needs
% to be adjusted (fine-tuned) based on our original pick.
[npeakint,mpeakint] = find(max(max(phi))==phi);
mpeakint = mpeakint(1);
npeakint = npeakint(1);

% These two values are not used in the program
xdint = -(mpeakint - (M/2 + 1));
ydint = -(npeakint - (N/2 + 1));

% Calculate sub-pixel displacement
mstar = (log(phi(npeakint,mpeakint+1)) - log(phi(npeakint,mpeakint-
1)))/...
(4*log(phi(npeakint,mpeakint)) - 2*log(phi(npeakint,mpeakint-1)) ...
- 2*log(phi(npeakint,mpeakint+1)));

nstar = (log(phi(npeakint+1,mpeakint)) - log(phi(npeakint-
1,mpeakint)))/...
(4*log(phi(npeakint,mpeakint)) - 2*log(phi(npeakint-1,mpeakint)) ...
- 2*log(phi(npeakint+1,mpeakint)));

mpeak = mpeakint + mstar;
npeak = npeakint + nstar;
xd = -(mpeak - (M/2 + 1));
yd = -(npeak - (N/2 + 1));
% % Display correlation surface and peak location
% figure(3)
% set(gcf,'position',[100 35 560 420])
% subplot(221)
% imshow(Aa)
% xlabel('i')
%
% subplot(222)
% imshow(Ab)
% xlabel('i+1')
%
%
% subplot(223)
% mesh(phi)
% xlabel('m')
% ylabel('n')
% shading interp
% hold on
% plot3(mpeakint,npeakint,max(max(phi)),'g.')

```

```

% plot3(mpeak,npeak,max(max(phi)), 'r.')
% hold off
% subplot(224)
% pcolor(phi)
% xlabel('m')
% ylabel('n')
% shading interp
% hold on
% plot(mpeakint,npeakint, 'g.', mpeak, npeak, 'r.')
% hold off
% pause
end

```

```

function [X] = DLTApply(uL,vL,uR,vR,L,R)

% Calculate A matrix
A = [L(1)-L(9)*uL L(2)-L(10)*uL L(3)-L(11)*uL; ...
L(5)-L(9)*vL L(6)-L(10)*vL L(7)-L(11)*vL; ...
R(1)-R(9)*uR R(2)-R(10)*uR R(3)-R(11)*uR; ...
R(5)-R(9)*vR R(6)-R(10)*vR R(7)-R(11)*vR];

% Calculate B matrix
B = [uL-L(4); vL-L(8); uR-R(4); vR-R(8)];

% Calculate X = [x,y,z] positions
X = inv(A'*A)*A'*B;
end

```

```

function [centroid, zerocoor] = CentroidFind(bw)
% This function finds the centroid of points in a pre processed image
% bw is a pre processed image
% The output 'centroid' is the centroids of the points from the image
% The output 'zerocoor' is the location of the zero point on the image
% Identify the connected components in the binary image
cc = bwconncomp(bw,8);
cc.NumObjects;
% Find the
pointdata = regionprops(cc, 'basic');
% Find the centroid and weighted centroid of the points
% s = regionprops(bw, I, {'Centroid','WeightedCentroid'});
% Find the surrounding area and remove it
point_areas = [pointdata.Area];
[~, idx] = max(point_areas);
pointdata = pointdata(idx+1:end);
% Find the location of the center point (big point)
point_areas = [pointdata.Area];
[idx] = find(point_areas > 200);
coor1 = pointdata(idx(1)).Centroid;

```

```

% coor2 = pointdata(idx(2)).Centroid;
uL = coor1(1);
vL = coor1(2);
% uR = coor2(1);
% vR = coor2(2);
zerocoor = [uL, vL];%, uR, vR];
% Plot the centroid and weighted centroid from the processed and original
% figure(5)
% imshow(bw)
% title('Weighted (red) and Unweighted (blue) Centroid Locations');
% hold on
% % numObj = numel(s);
% % for k = 1 : numObj
% % plot(s(k).WeightedCentroid(1), s(k).WeightedCentroid(2), 'r*');
% % plot(s(k).Centroid(1), s(k).Centroid(2), 'bo');
% % end
% % hold off
% %
% Plot the centroid calculated only from the processed image

figure(6)
imshow(bw)
hold on
numObj2 = numel(pointdata);
for k = 1 : numObj2
    plot(pointdata(k).Centroid(1), pointdata(k).Centroid(2), 'bo');
end

plot(uL, vL, 'gd') %, uR, vR, 'gd')
hold off

for i = 1: numel(pointdata)
    centroid(i,:) = [pointdata(i).Centroid];
end

Lcentroid = centroid(1:100);

% Rcentroid = centroid(101:200);
end

function [ uL vL uR vR ] = dotsort(centroidgrid)
%dotsort
% Extract the left and right coordinates from the centroid matrix
xl = centroidgrid(1:100,1,:);
xr = centroidgrid(101:200,1,:);
yl = centroidgrid(1:100,2,:);
yr = centroidgrid(101:200,2,:);
% Place the above data into 2-D matrices
uL = [xl(:, :, 1); xl(:, :, 2); xl(:, :, 3); xl(:, :, 4); xl(:, :, 5);
xl(:, :, 6)];% xl(:, :, 7); xl(:, :, 8)];
vL = [yl(:, :, 1); yl(:, :, 2); yl(:, :, 3); yl(:, :, 4); yl(:, :, 5);
yl(:, :, 6)];% yl(:, :, 7); yl(:, :, 8)];
uR = [xr(:, :, 1); xr(:, :, 2); xr(:, :, 3); xr(:, :, 4); xr(:, :, 5);
xr(:, :, 6)];% xr(:, :, 7); xr(:, :, 8)];

```

```

    vR = [yr(:, :, 1); yr(:, :, 2); yr(:, :, 3); yr(:, :, 4); yr(:, :, 5);
yr(:, :, 6);]; % yr(:, :, 7); yr(:, :, 8);];
end

```

```

function [L,R] = DLTCalib(uL,vL,uR,vR,x,y,z)
    % Construct A matrix for left and right views, u component

    N=length(x);
    for i=1:2:N*2
        k=(i+1)/2;
        AL(i,:)= [x(k) y(k) z(k) 1 0 0 0 0 -uL(k)*x(k) -uL(k)*y(k) -
uL(k)*z(k)];
        AR(i,:)= [x(k) y(k) z(k) 1 0 0 0 0 -uR(k)*x(k) -uR(k)*y(k) -
uR(k)*z(k)];
        BL(i,1)=[uL(k)];
        BR(i,1)=[uR(k)];
    end

    % Construct A matrix for left and right views, v component

    for i=2:2:N*2
        k=i/2;
        AL(i,:)= [0 0 0 0 x(k) y(k) z(k) 1 -vL(k)*x(k) -vL(k)*y(k) -
vL(k)*z(k)];
        AR(i,:)= [0 0 0 0 x(k) y(k) z(k) 1 -vR(k)*x(k) -vR(k)*y(k) -
vR(k)*z(k)];
        BL(i,1)=[vL(k)];
        BR(i,1)=[vR(k)];
    end

    % Calculate L and R calibration matrices
    L=(inv(AL'*AL))* (AL'*BL);
    R=(inv(AR'*AR))* (AR'*BR);
end

```

```

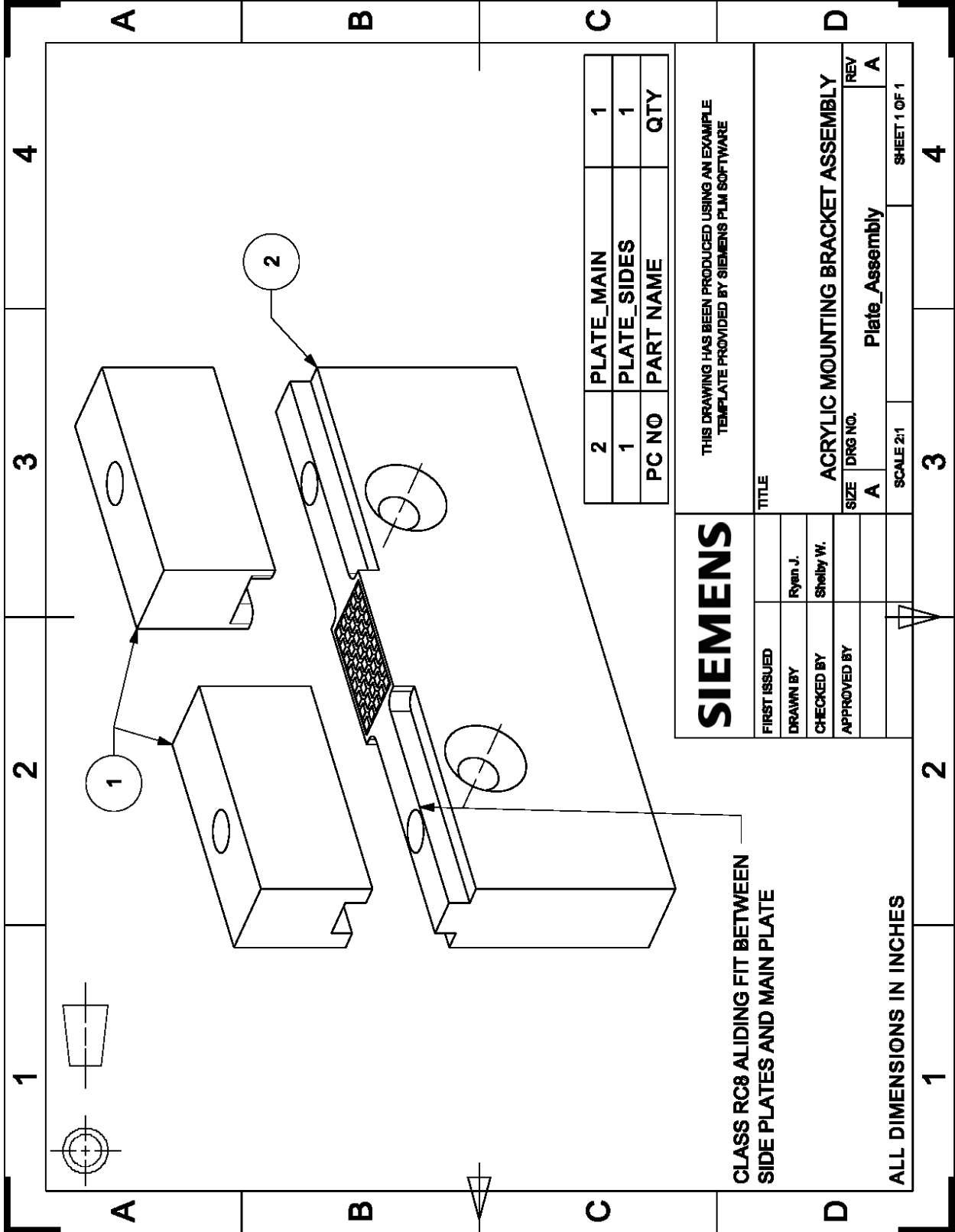
function [centroid] = sortcentroid(centroid1, centroid2)
    %SORTCENTROID receives the matrix centroid, parses the data into a matrix
    %of single columns, sorts them according to the y coordinate (column 2),
    centroid = [sortrows(centroid1(1:10,:),2);
        sortrows(centroid1(11:20, :),2);
        sortrows(centroid1(21:30, :),2);
        sortrows(centroid1(31:40, :),2);
        sortrows(centroid1(41:50, :),2);
        sortrows(centroid1(51:60, :),2);
        sortrows(centroid1(61:70, :),2);
        sortrows(centroid1(71:80, :),2);
        sortrows(centroid1(81:90, :),2);
        sortrows(centroid1(91:100, :),2);
        sortrows(centroid2(1:10, :),2);
        sortrows(centroid2(11:20, :),2);
        sortrows(centroid2(21:30, :),2);
        sortrows(centroid2(31:40, :),2);

```

```
sortrows(centroid2(41:50, :), 2);  
sortrows(centroid2(51:60, :), 2);  
sortrows(centroid2(61:70, :), 2);  
sortrows(centroid2(71:80, :), 2);  
sortrows(centroid2(81:90, :), 2);  
sortrows(centroid2(91:100, :), 2);];  
end
```

APPENDIX C. DRAWINGS AND PROCESS SHEETS FOR THE MOUNTING PLATES

Enclosed are the drawings and process sheets for the mounting plates mentioned in Chapter 3. The plates were designed by Shelby Ward. The drawings and manufacturing process sheets were written by Ryan Jenkins. Manufacturing of the plates was performed by Shelby Ward, Ryan Jenkins and Kevin Moore.



CLASS RC8 ALIDING FIT BETWEEN
SIDE PLATES AND MAIN PLATE

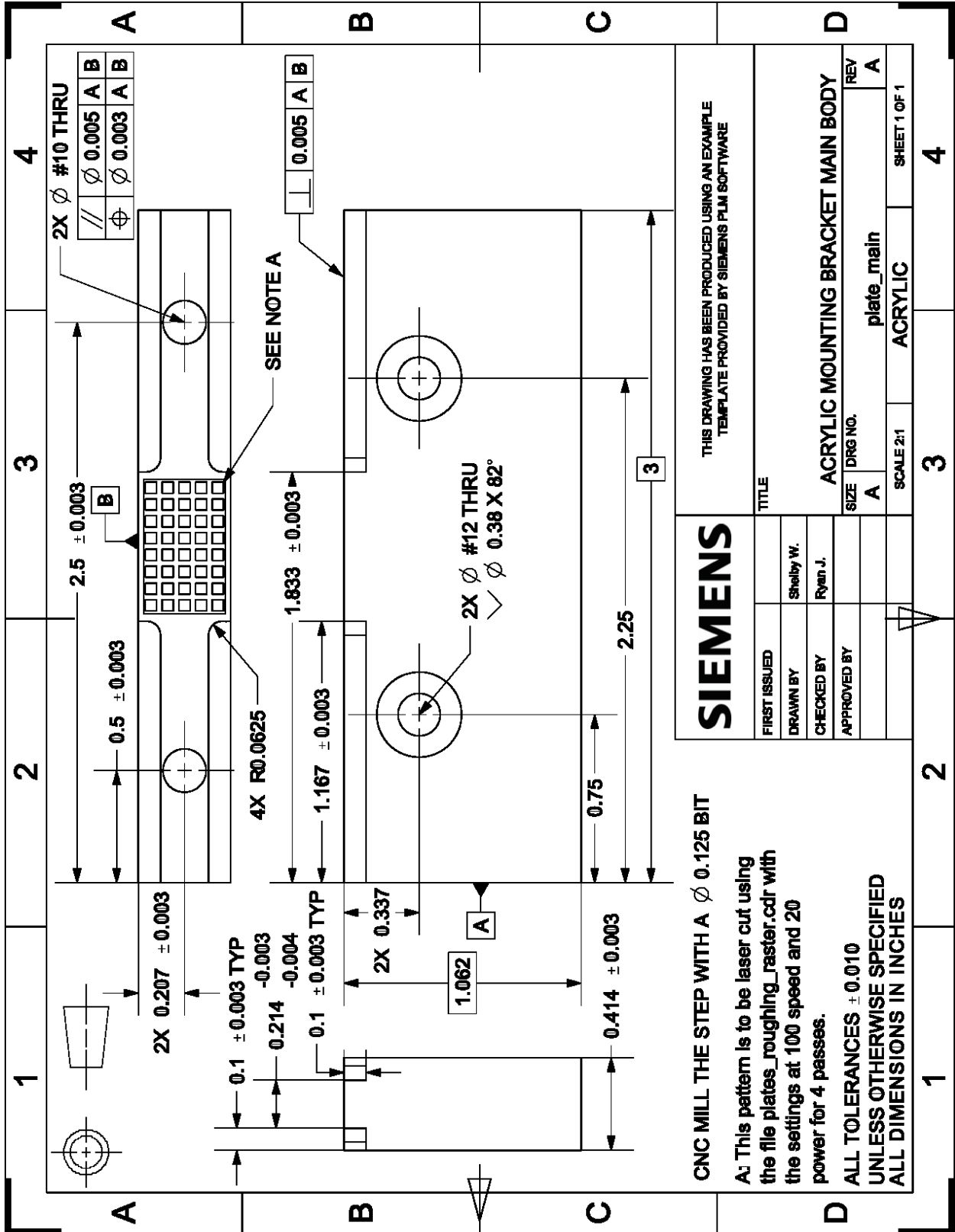
SIEMENS

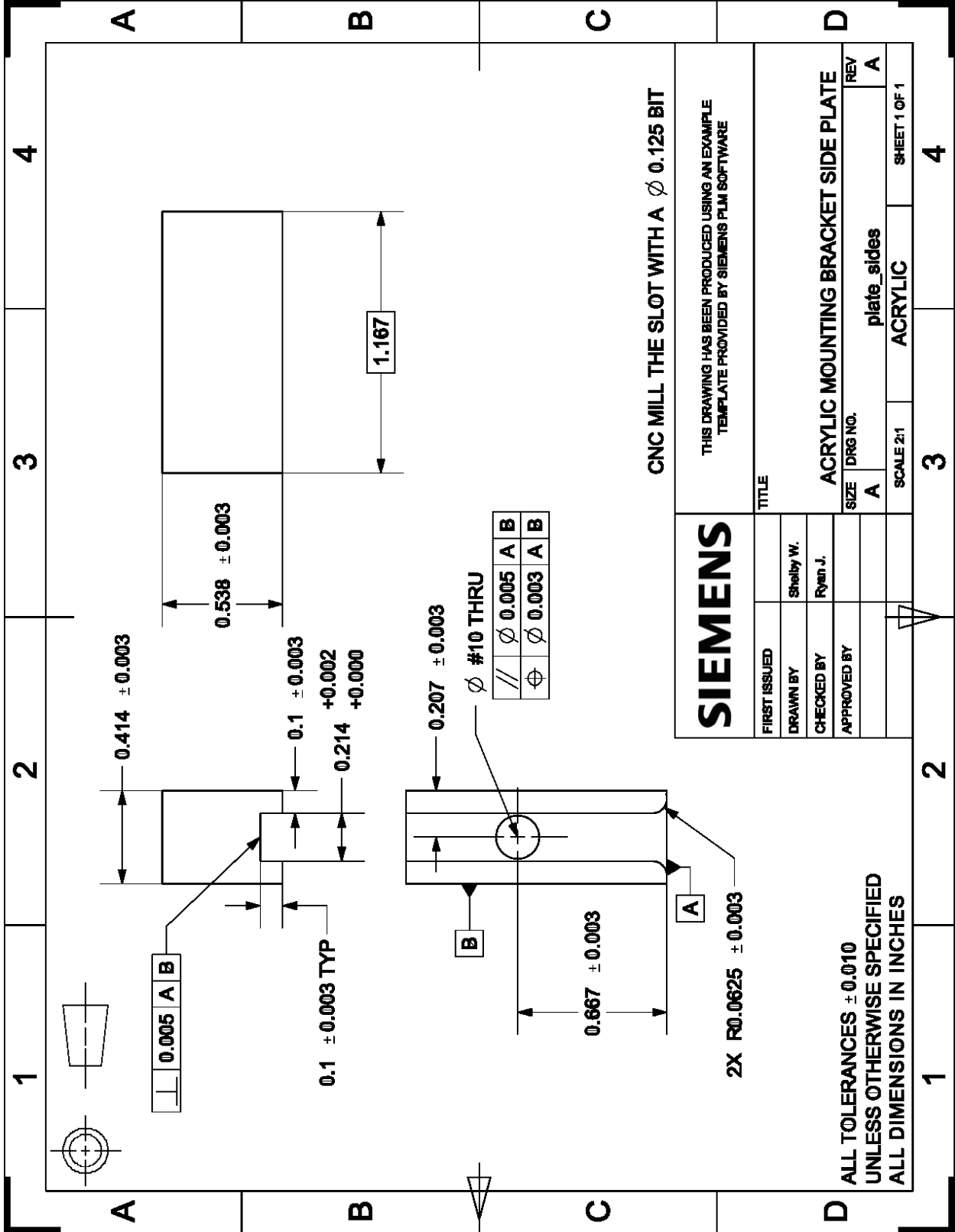
THIS DRAWING HAS BEEN PRODUCED USING AN EXAMPLE
TEMPLATE PROVIDED BY SIEMENS PLM SOFTWARE

FIRST ISSUED		TITLE	
DRAWN BY	Ryan J.	ACRYLIC MOUNTING BRACKET ASSEMBLY	REV
CHECKED BY	Shelby W.	SIZE	A
APPROVED BY		DRG NO.	Plate_Assembly
		SCALE	2:1
			SHEET 1 OF 1

PC NO	PART NAME	QTY
2	PLATE_MAIN	1
1	PLATE_SIDES	1

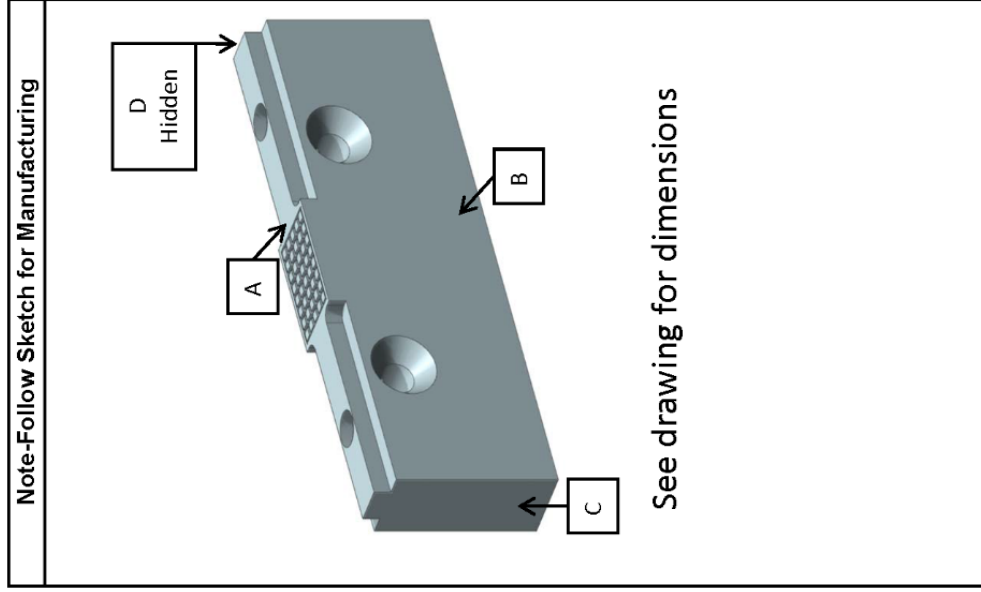
ALL DIMENSIONS IN INCHES





Manufacturing Process Sheet

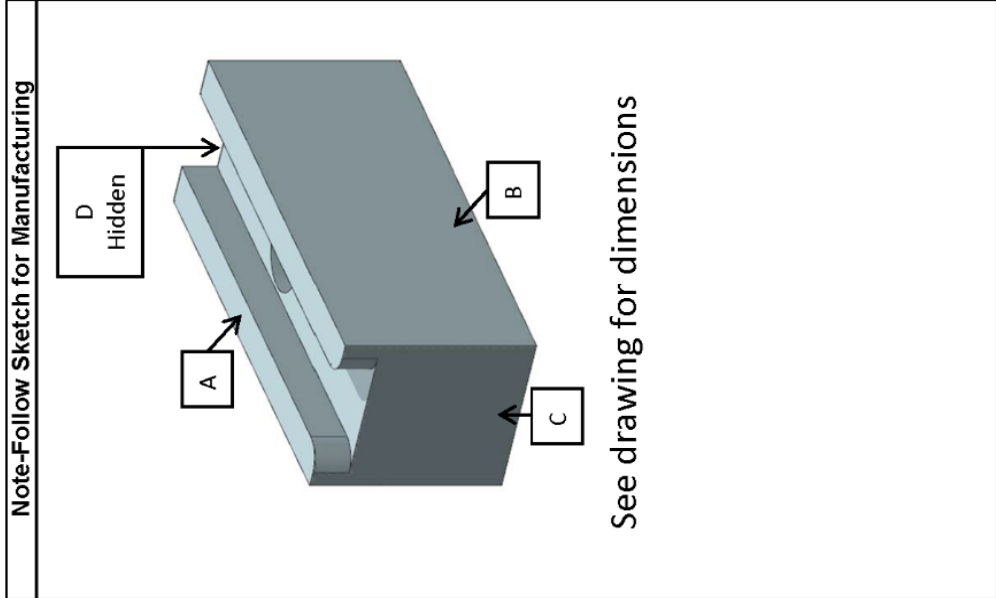
Part No. 2 Part Name MAIN PLATE Model plate_main.prt Oper. No. 1
 Dept No. BYU VFMRG Loc. FB 220C Material ACRYLIC Sheet 1 Of 1
 Prepared By: Ryan Jenkins Date 1/14/2014 Approved By: _____



Oper. Seq.	Description of Operation	RPM	Feed Rate	Name of Tool	Tool No.
1	Obtain 1/2" Acrylic stock	N/A	N/A	N/A	N/A
2	Rough cut to 3.1" X 1.15"	N/A	By Hand	Band Saw	1
3	Place block in manual mill	N/A	N/A	Mill	2
4	Face off surface A till clean	1500	By Hand	Flycutter	3
5	Flip block over	N/A	N/A	Mill	2
6	Face off surface to size (1.062")	1500	By Hand	Flycutter	3
7	Place block so that surface B is face up and the two faced surfaces are clamped in the vice	N/A	N/A	Mill	2
8	Face surface B to size (0.414")	1500	By Hand	Flycutter	3
9	Reposition block so that A is up	N/A	N/A	Mill	2
10	Face off surface C till clean	2000	By Hand	1/2" End Mill	4
11	Flip block around so D is out	N/A	N/A	Mill	2
12	Face off surface D to size (3")	2000	By Hand	1/2" End Mill	4
13	Place block with surface B face up in the CNC mill	N/A	N/A	CNC Mill	5
14	Drill thru holes			#12 Drill Bit	6
15	Countersink holes			82° Countersink	7
16	Reposition block so that A is up	N/A	N/A	CNC Mill	5
17	Drill thru holes			#10 Drill Bit	8
18	Run G-code to cut out the steps			1/8" End Mill	9
19	Clean off part	N/A	N/A	N/A	N/A
20	Place part with A up in Epilog laser engraver	N/A	N/A	Laser Cutter	10
21	Center laser pointer on part	N/A	N/A	Laser Cutter	10
22	Focus laser on surface A	N/A	N/A	Laser Cutter	10
23	Run plates_roughing_raster.cdr at 100 Speed and 20 Power	N/A	N/A	Laser Cutter	10
24	Repeat step 23 three more times	N/A	N/A	Laser Cutter	10
25	Clean off part	N/A	N/A	N/A	N/A

Manufacturing Process Sheet

Part No. 1 Part Name SIDE PLATE Model plate sides.prt Oper. No. 2
 Dept No. BYU VFMRG Loc. FB 220C Material ACRYLIC Sheet 1 Of 1
 Prepared By. Ryan Jenkins Date 1/14/2014 Approved By. _____



See drawing for dimensions

Oper. Seq.	Description of Operation	RPM	Feed Rate	Name of Tool	Tool No.
1	Obtain 1/2" Acrylic stock	N/A	N/A	N/A	N/A
2	Rough cut to 1.25" X 0.6"	N/A	By Hand	Band Saw	1
3	Place block in manual mill	N/A	N/A	Mill	2
4	Face off surface A till clean	1500	By Hand	Flycutter	3
5	Flip block over	N/A	N/A	Mill	2
6	Face off surface to size (0.538")	1500	By Hand	Flycutter	3
7	Place block so that surface B is face up and the two faced surfaces are clamped in the vice	N/A	N/A	Mill	2
8	Face surface B to size (0.414")	1500	By Hand	Flycutter	3
9	Reposition block so that A is up	N/A	N/A	Mill	2
10	Face off surface C till clean	2000	By Hand	1/2" End Mill	4
11	Flip block around so D is out	N/A	N/A	Mill	2
12	Face off surface D to size (3")	2000	By Hand	1/2" End Mill	4
13	Place block in CNC mill with surface A face up	N/A	N/A	CNC Mill	2
14	Drill thru hole			#10 Drill	5
15	Run G-code to cut out the slot			1/8" End Mill	6
16	Clean off part	N/A	N/A	N/A	N/A

APPENDIX D. VECTOR 3D

Below are the Vector 3D settings used for generating the G-code for milling the powdered sugar expendable molds.

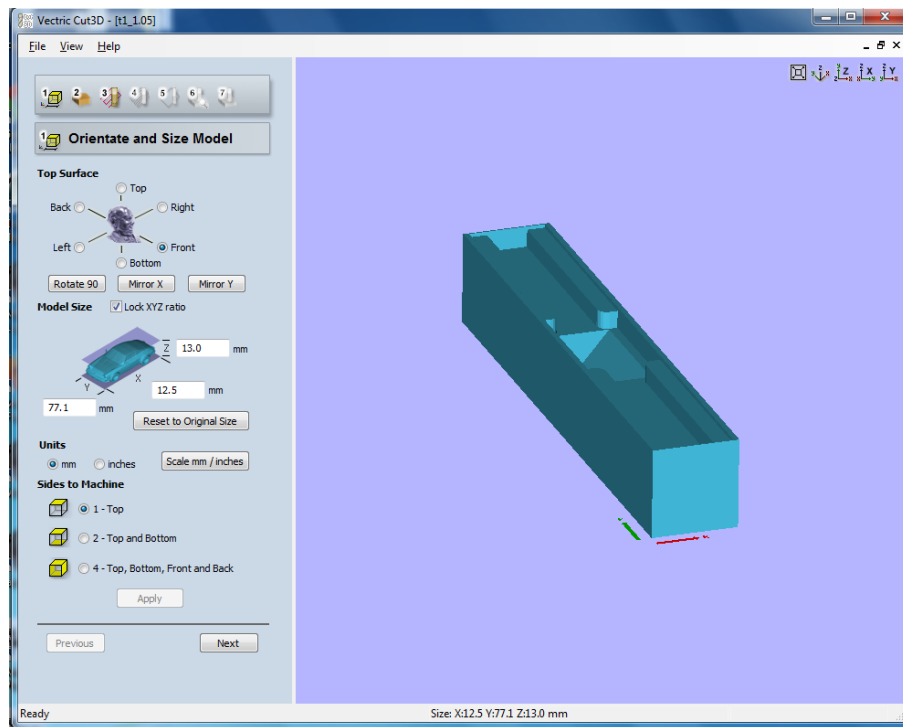


Figure D.1: Model orientation.

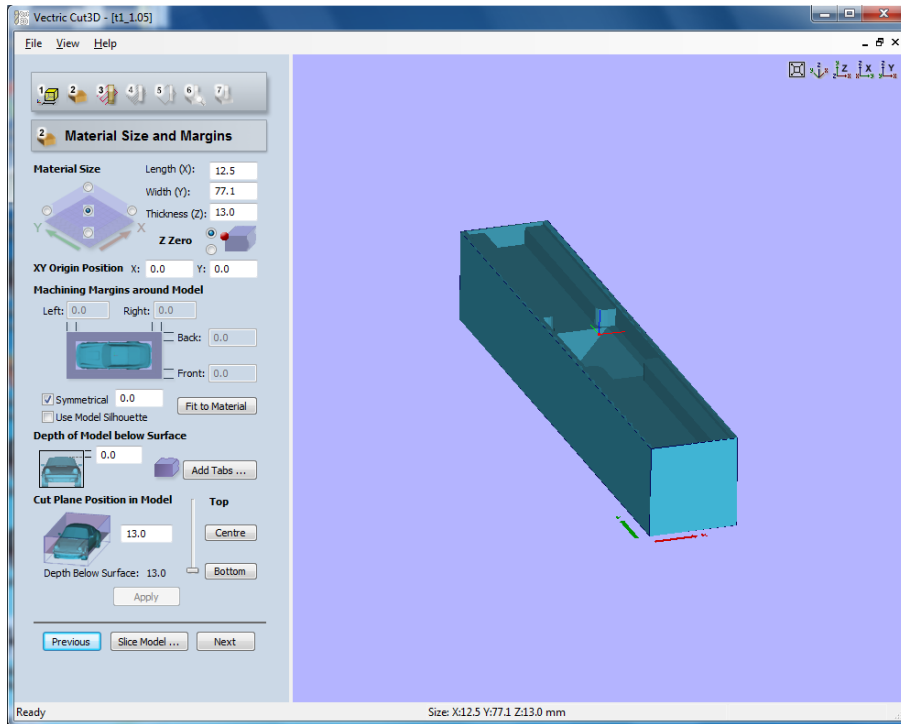


Figure D.2: Model size.

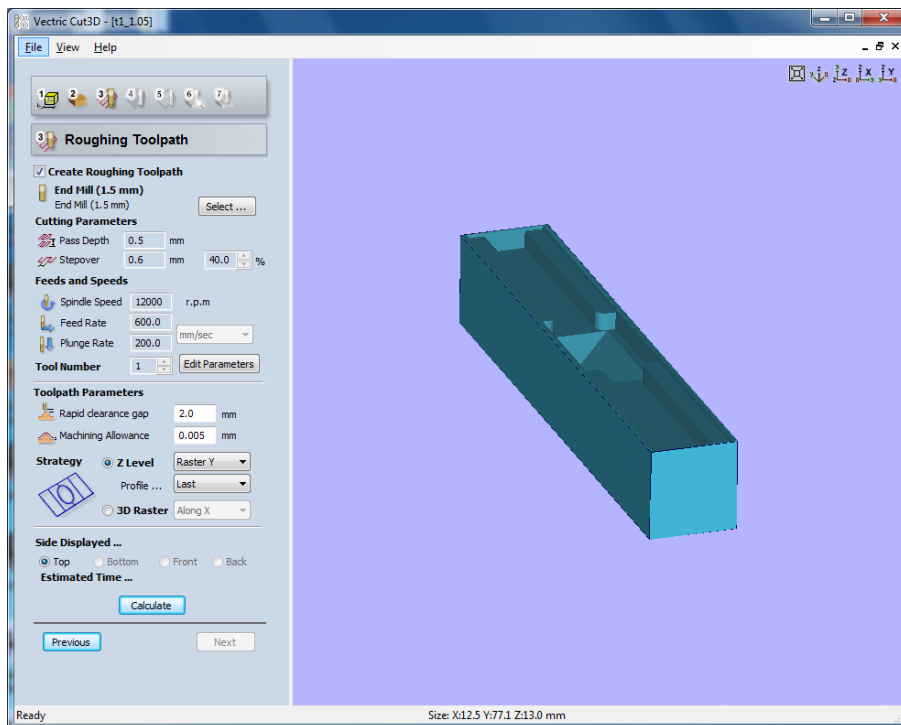


Figure D.3: Rough cut settings.

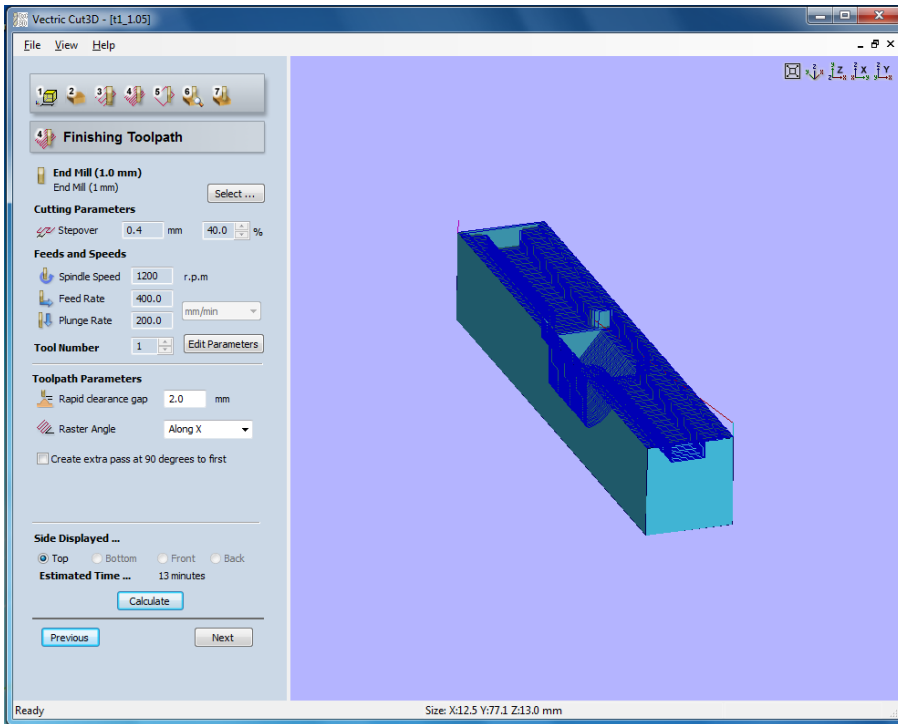


Figure D.4: Finishing cut settings.

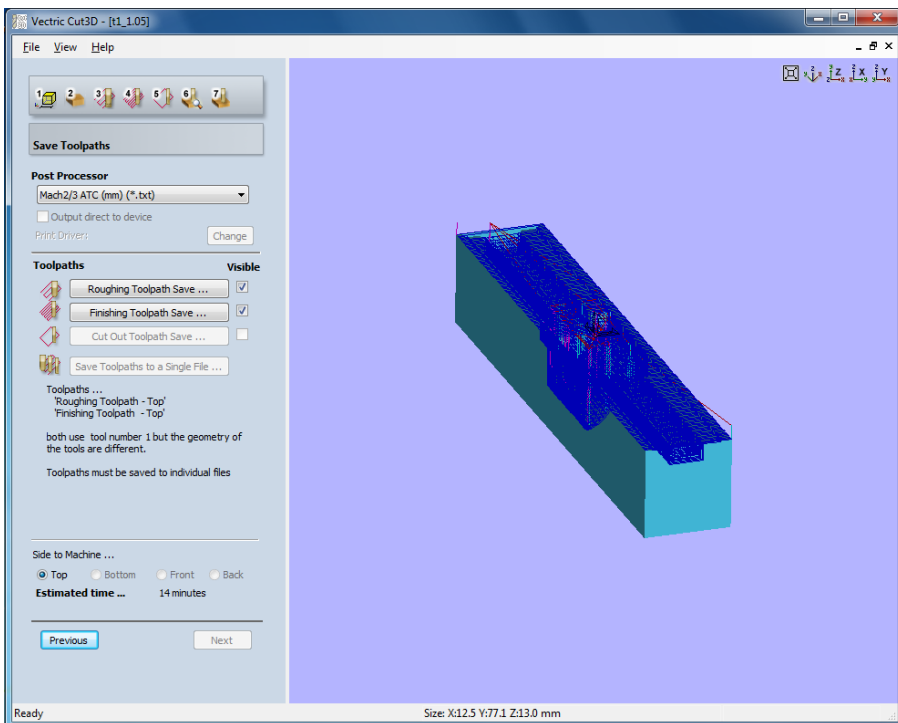


Figure D.5: Toolpath save screen.

APPENDIX E. MACH3 CNC SET UP

Below are the settings used to run Mach3 to control the Zen Toolworks 12 X 12 F8 CNC table top mill.

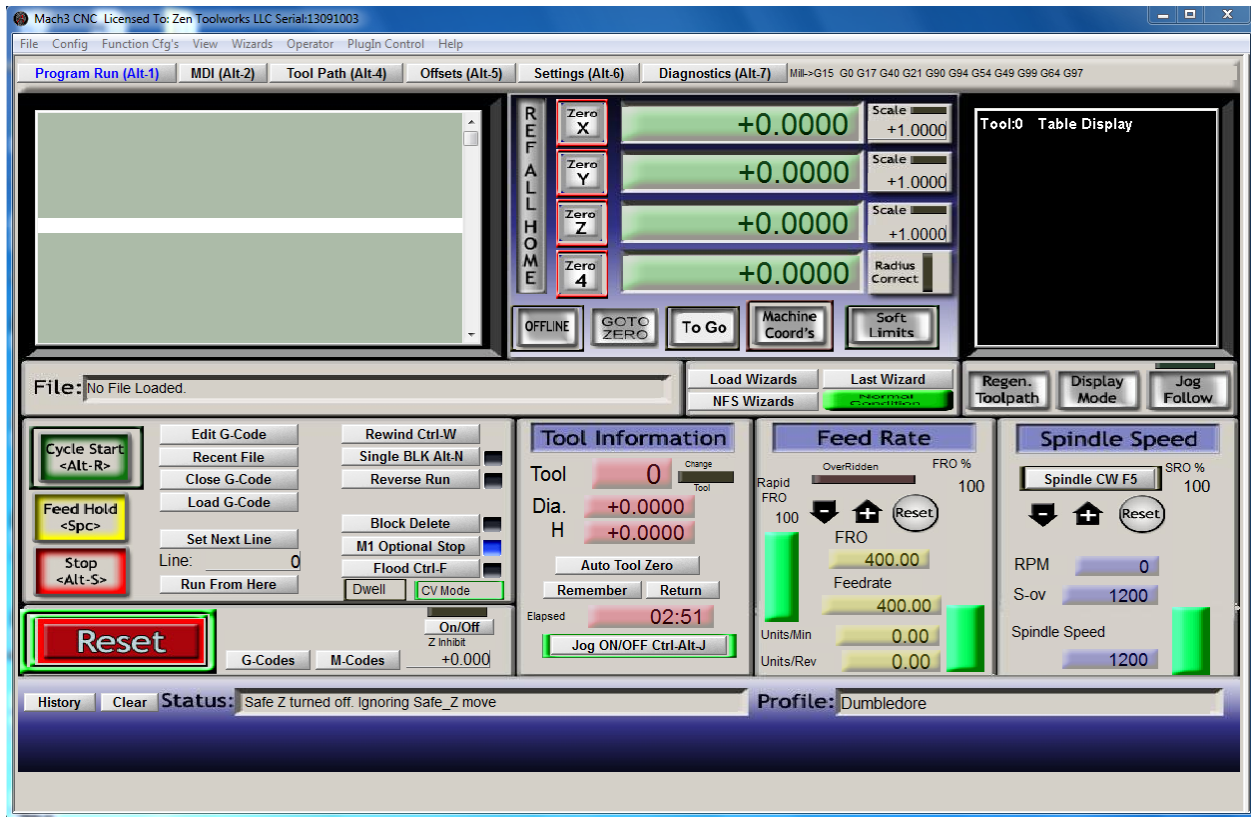


Figure E.1: Mach3 control panel.

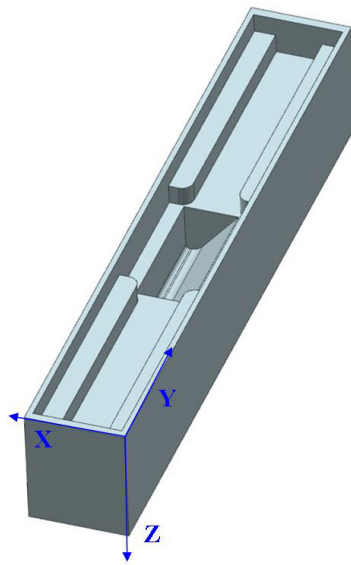


Figure E.2: X, Y, and Z orientation

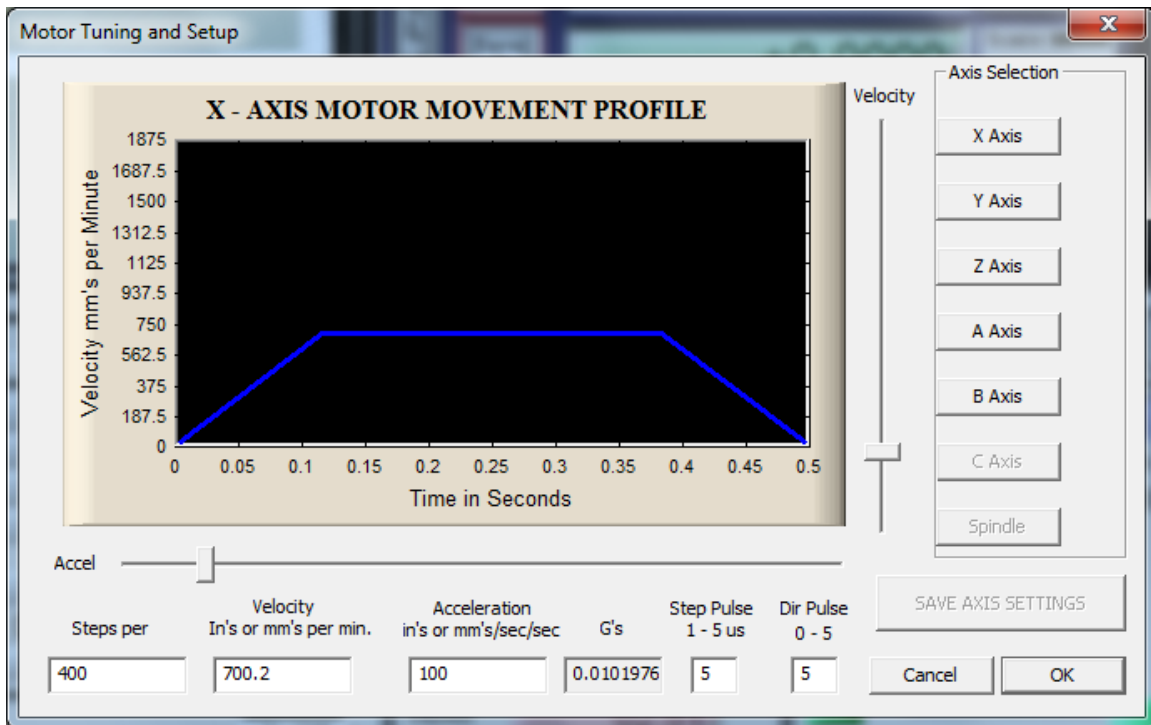


Figure E.3: Mach3 X-axis motor settings.

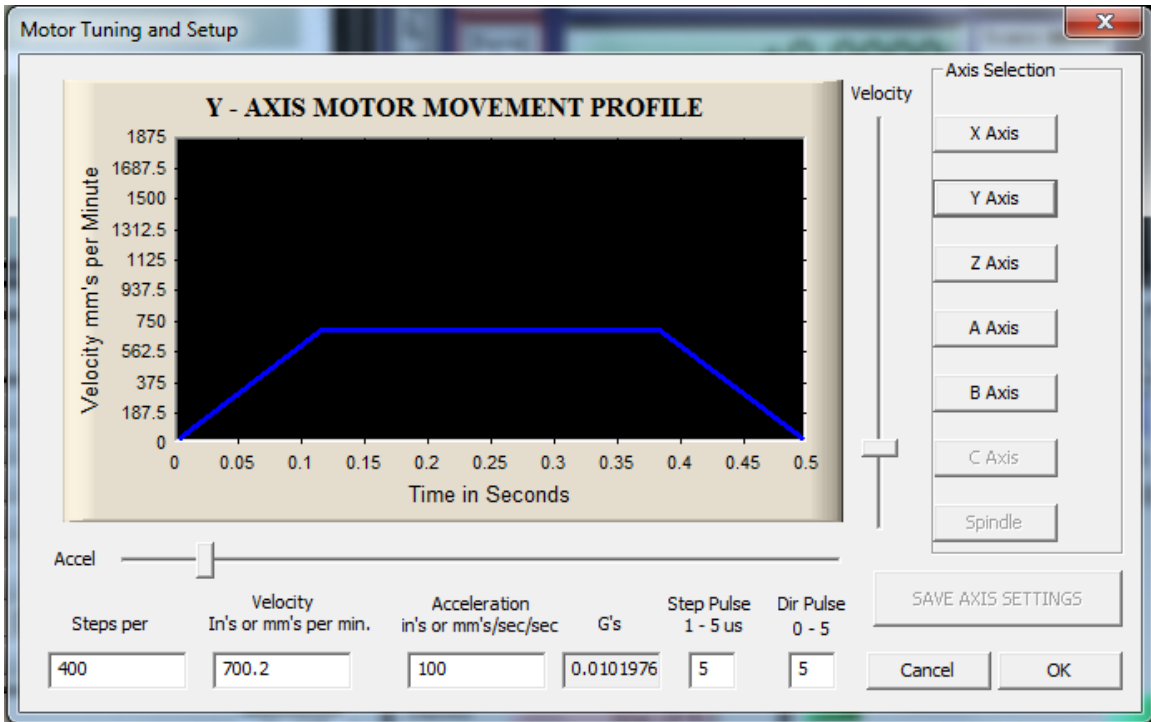


Figure E.4: Mach3 Y-axis motor settings.

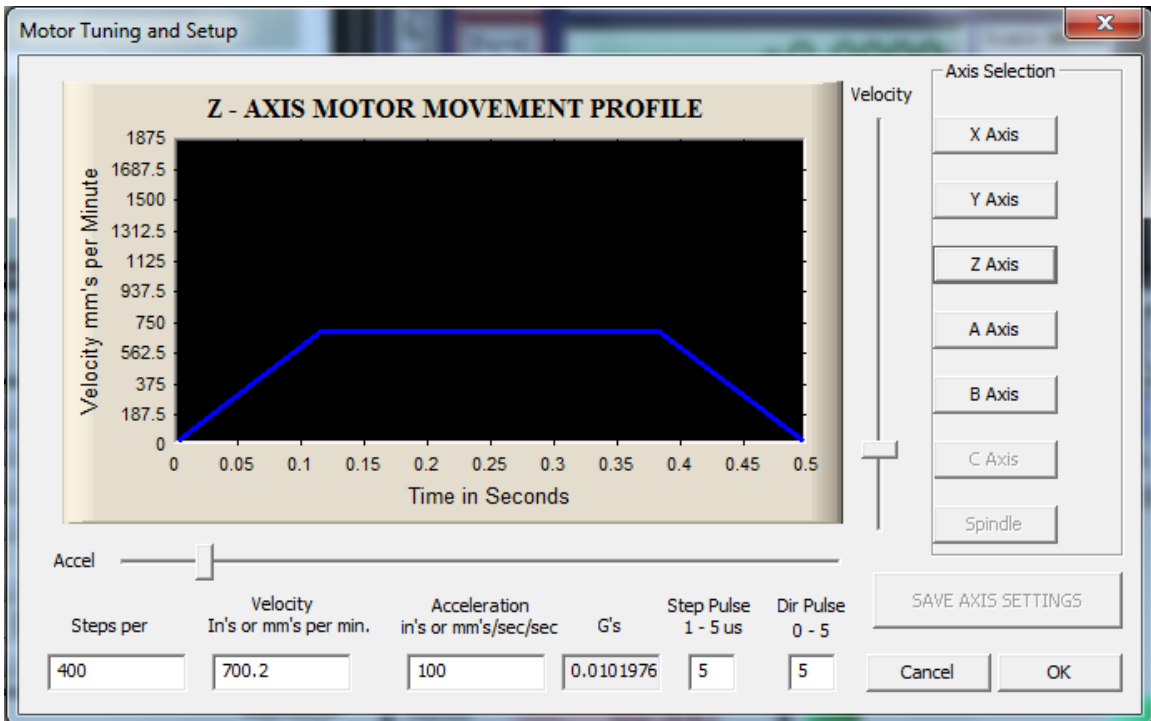


Figure E.5: Mach3 Z-axis motor settings.

APPENDIX F. CURING DETAILS

Table F.1: Silicone curing details.

Silicone Ratio (Part A: Part B: Thinner)	Recommended cure time at 220° F
1:1:1 Ecoflex	30 minutes
1:1:2 Ecoflex	40 minutes
1:1:3 Ecoflex	45 minutes
1:1:4 Ecoflex	1 hour
1:1:5 Ecoflex	1.25 hours
1:1:6 Ecoflex	1.25 hours
1:1:8 Ecoflex	1.5 hours
1:1:1 Dragon Skin 10 Fast	10 minutes (or 2 hours at room temperature)

Table F.2: Curing times used for Chapter 4 models.

Silicone Ratio (Part A: Part B: Thinner)	Recommended cure time at 150° F
1:1:1 Ecoflex	1 hour
1:1:8 Ecoflex	2 hours
1:1:1 Dragon Skin 10 Fast	2 hours at room temperature